

Controlled orientation and periodicity of surface rippling on compliant and brittle amorphous materials induced by scanning probe lithography

DISSERTATION

zur Erlangung des akademischen Grades

Doktoringenieur (Dr.-Ing.)

vorgelegt

der Fakultät Maschinenwesen
der Technischen Universität Dresden

von

M. Sc. Jana Hennig

geboren am 23. März 1990 in Zeitz, Deutschland

Tag der Einreichung: 22. August 2022

Tag der Verteidigung: 09. Januar 2023

Promotionskommission:

Vorsitz: Prof. Dr. Markus Kästner

Gutachter: Prof. Dr. Gianaurelio Cuniberti

Prof. Dr. Enrico Gnecco

Mitglieder: Prof. Dr. Hans-Peter Wiesmann

Prof. Dr. Maik Gude

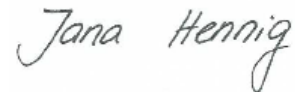
Declaration

I hereby declare that the thesis entitled “Controlled orientation and periodicity of surface rippling on compliant and brittle amorphous materials induced by scanning probe lithography” submitted by me, for the award of the degree of *Doktoringenieur* to Technische Universität Dresden is a record of bonafide work carried out by me under the supervision of Prof. Dr. Gianaurelio Cuniberti and Prof. Dr. Enrico Gnecco, in the Otto Schott Institute of Materials Research at Friedrich Schiller University Jena and the Chair of Materials Science and Nanotechnology at TU Dresden.

I further declare that the work reported in this thesis has not been submitted and will not be submitted, either in part or in full, for the award of any other degree or diploma in this institute or any other institute or university.

Place: Jena

Date: 10. Juli 2022

A handwritten signature in black ink, reading "Jana Hennig". The script is cursive and elegant, with the first letters of the first and last names being capitalized and prominent.

Signature of the Candidate

Contents

Contents	i
Abstract	iii
Zusammenfassung	v
1. Introduction	1
1.1. Periodic surface structures – relevance and formation	1
1.2. Surface rippling created by scanning probe lithography	2
1.3. Wear and nanoparticle release	4
1.4. Aim and outline	4
2. Experimental methods and fundamental concepts	6
2.1. Nanolithography	6
2.2. Atomic force microscopy	7
2.3. Nanoindentation and -scratching	10
2.4. Wear	11
2.5. Stick-slip motion	12
2.6. Spin coating	14
3. Surface rippling on polystyrene	15
3.1. Background and motivation	15
3.2. Methods	20
3.2.1. Sample preparation	20
3.2.2. Scanning probe lithography process	20
3.2.3. Imaging of structures and nanoparticles	21
3.3. Effect of boundaries on the orientation of surface rippling	22
3.4. Particle release as a result of surface rippling	31
4. Periodic structures inside scratches on silica glass	37
4.1. Background and motivation	37
4.2. Methods	38
4.2.1. Sample preparation	39
4.2.2. Scratch tests	39
4.2.3. AFM imaging and analysis	39

4.3. Surface rippling induces by scraping with a sharp indenter.....	40
5. Conclusion and outlook	49
A. Appendix surface rippling on polymers	I
B. Appendix surface rippling on glass	IV
Acknowledgements	VII
References.....	IX

Abstract

This thesis reports on the controlled formation of surface rippling structures induced by tip scanning processes on compliant and brittle materials. Periodic surface structures were generated on polymeric and vitreous materials and with different length scales. Two aspects were focused on: the controlling of orientation and periodicity of the resulting structures via proper tuning the scan conditions and the physical mechanisms ruling the early stages of plowing wear causing the rippling effect.

Specifically the influence of the scanned area geometric shape on the orientation of the rippling structure was investigated on a polystyrene surface. Nanoripples were induced by scanning the surface with a silicon tip using atomic force microscopy and dedicated scripts. Inside a structured area two ripple orientations can be observed: near boundaries the ripple orientation is determined by boundary orientation and regions away from the boundaries the ripples are aligned in a steady orientation. This steady orientation can be tuned by the distance between the scan lines. In the boundary regions the orientation of the ripples is different from steady orientation. The orientation of the boundaries clearly affected the orientation of the ripples and the tendency of the ripples to align in a steady angle defined by the scan parameters could be significantly modified. Geometric shapes like squares, circles, stars, pentagons and hearts allowed to distinguish the influence of curved and straight boundaries. Straight boundaries with different orientations allowed a detailed analysis of the influence of the angle on the rippling process. Straight boundaries inclined in the direction of the steady state angle of ripple orientation previously defined generate a uniform ripple pattern covering the entire scan area.

The aspect of wear originating from the rippled surface was also investigated on similar polystyrene surfaces. As a result of repetitive scan passes spherical particles with diameters up to 250 nm were nucleated and detached from the surface. The particles originate from the crests of the ripples formed in the first scan pass. As proven by the lateral force signal the detachment occurs smoothly without a static friction peak suggesting a crazing mechanism induced by the scanning tip. Once detached from the surface the particles are displaced and piled up along the edges of scanned area.

The formation of periodic surface structures was also investigated on a brittle silica glass. By a combination of scratch tests performed with a diamond microtip mounted in a nanoindenter and imaging with atomic force microscopy the existence of a periodic herringbone pattern inside scratch grooves on silica glass was proven. The rippled pattern was induced in the scratch process when the indenter was pulled laterally along the surface resulting in a microscopic scratch groove. The load was varied up to 30 nN and the scan velocity up to 500 $\mu\text{m/s}$. The resulting periodicity of the structures was found to increase linearly with increasing scratch velocity. The repetition distance was in the range of sub- μm and the corrugation in the range of a few hundred nm, which was well below indentation depth.

In both cases, the surface rippling on a polymeric surfaces and the formation of a periodic pattern inside microscratches on a glass surface, the results were found to be consistent with minimalistic theoretical models for stick-slip.

Zusammenfassung

Die vorliegende Arbeit untersucht die gezielte Beeinflussung von periodischen Oberflächenstrukturen, die durch gleitende Kontakte hervorgerufen werden. Dafür wurden periodische Oberflächenstrukturen auf einem Polymer und einem Glas in jeweils verschiedenen Größenskalen erzeugt. Zwei Aspekte standen dabei im Vordergrund: die Steuerung der Ausrichtung der Strukturen bzw. deren Periodizität durch eine geeignete Abstimmung der experimentellen Parameter und die physikalischen Mechanismen, die in frühen Stadien von Verschleiß für die Entstehung von periodischen Strukturen verantwortlich sind.

Insbesondere wurde der Einfluss der geometrischen Form des gescannten Bereichs auf die Ausrichtung der periodischen Struktur auf einer Polystyroloberfläche untersucht. Die Nanostrukturen wurden durch Abfahren der Oberfläche mit einer Siliziumspitze mittels Rasterkraftmikroskopie und speziellen Skripten erzeugt. Innerhalb eines strukturierten Bereichs lassen sich bei den Strukturen zwei Orientierungen beobachten: Im Randbereich wird die Ausrichtung der Strukturen durch die Orientierung der Grenzen bestimmt und in Regionen abseits der Randbereiche sind die Strukturen in einer gleichmäßigen Orientierung ausgerichtet. Diese gleichmäßige Ausrichtung kann durch den Abstand zwischen den Scanlinien eingestellt werden. In den Randbereichen weicht die Ausrichtung der Rippel von der gleichmäßigen Orientierung ab. Die Ausrichtung der Ränder hat folglich einen deutlichen Einfluss auf die Ausrichtung der Strukturen, und die Tendenz, sich in einem durch die Scan-Parameter definierten gleichmäßigen Winkel auszurichten, konnte erheblich verändert werden. Geometrische Formen wie Quadrate, Kreise, Sterne, Fünfecke und Herzen erlaubten es, den Einfluss von gekrümmten und geraden Grenzen zu unterscheiden. Gerade Ränder mit unterschiedlichen Ausrichtungen ermöglichten eine detaillierte Analyse des Einflusses des Winkels auf den Strukturierungsprozess. Grenzen, deren Ausrichtung ähnlich des zuvor definierten gleichmäßigen Winkels ist, erzeugen ein einheitliches Muster, das den gesamten Scanbereich abdeckt.

Weiterhin wurde auf ähnlichen Polystyroloberflächen Verschleiß ausgehen von den strukturierten Oberflächen untersucht. Bei wiederholten Scandurchläufen wurden kugelförmige Partikel mit Durchmessern von bis zu 250 nm erzeugt und von der Oberfläche abgelöst. Die Partikel bilden sich ausgehen von den Bergen der im ersten Scan-Durchgang gebildeten wellenförmigen Strukturen. Wie die dabei aufgenommene laterale Kraftkurve zeigt, erfolgt die Ablösung fließend und ohne plötzlichen Abfall der Reibungskraft. Daraus kann auf einen Crazing-Mechanismus geschlossen werden, der durch die Spitze induziert ist. Sobald sich die Partikel von der Oberfläche gelöst haben, werden sie verschoben und entlang der Ränder des gescannten Bereichs aufgehäuft.

Die Bildung periodischer Oberflächenstrukturen wurde auch auf einem spröden Quarzglas untersucht. Durch eine Kombination von Kratztests mit einer in einem Nanoindenter montierten Diamantmikrospitze und der Bildgebung mit dem Rasterkraftmikroskop wurde die Existenz eines periodischen Fischgrätenmusters innerhalb von Mikrokratzern auf Quarzglas

nachgewiesen. Das Fischgrätenmuster wurde beim Kratzvorgang erzeugt, bei dem der Indenter seitlich entlang der Oberfläche gezogen wurde, was zu einem mikroskopischen Kratzer führte. Die Kraft wurde bis zu 30 nN und die Scangeschwindigkeit bis zu 500 $\mu\text{m/s}$ variiert. Es wurde festgestellt, dass die resultierende Periodizität der Strukturen mit zunehmender Kratzgeschwindigkeit linear zunimmt. Die Periodizität lag im Bereich von sub- μm und die Höhe der Strukturen im Bereich von einigen hundert nm, was deutlich unter der Eindringtiefe lag.

In beiden Fällen, d. h. bei der Oberflächenstrukturierung auf Polymeroberflächen und bei der Bildung eines periodischen Musters innerhalb von Mikrokratzern auf einer Glasoberfläche, stimmten die Ergebnisse mit den minimalistischen theoretischen Modellen für Stick-Slip überein.

1. Introduction

In the first chapter the motivation for investigation and controlling of surface rippling on different materials is given. In this context the importance of stable periodic surface structures in particular applications was highlighted and the risk of nanoparticle release is introduced. Finally the general aim and outline of this thesis are given.

1.1. Periodic surface structures – relevance and formation

The formation of periodic surface structures like wrinkles or ripples on compliant surfaces is a process that can be observed in natural systems as well as artificial systems. The dimensions cover a wide range of length scales from meters down to nanometers, which offers macroscopic as well as microscopic applications. [1, 2]

The potential of surface wrinkles lies in the wide field of applications based on periodic surface structures. Especially periodic surface structures in the range of micro- and nanometers play an important role in biorelated and technical applications. For biorelated or biomedical applications the interaction between the (nano-)structured surface and cells is the key parameter. The cell activity is significantly influenced by the chemical and physical properties of the substrate. By adjusting the dimensions of the surface structures (e.g. on implants) on one hand cell growth on the material can be improved or reduced. A cell differentiation can be achieved and the orientation of cell growth can be controlled. These effects make the interaction of tissue engineering application and the biological system more efficient. On the other hand cell death or a reduced adhesion of bacteria can be achieved. For both aspects a chemical functionalization of the surface is not necessary and enables a series of applications in tissue engineering and other biorelated applications (e.g. marine antifouling coatings). In consequence the surface structure can enhance the biocompatibility of biomaterial scaffolds or can be used to reduce cell adhesion in order to prevent infections related to surface contaminations. [1-4] Additionally the wettability of surface can be controlled by the nanostructure of the surface enabling the production of superhydrophilic or superhydrophobic surfaces. This effect can be used in biorelated application as well as for technical applications like self-cleaning coatings. [2]

Furthermore periodic surface micro and nano structures offer a series of technical applications in the fields of optics and electronics. As an optical application wrinkled polymer layers are used for smart windows. Since the transmittance of the layer can be varied from translucent in the relaxed wrinkled state to transparent in the stretched and unwrinkled state the transmittance of windows can be switched. It has been demonstrated that wrinkled layered systems improve the efficiency of solar cells. The light absorption of the active layer of organic photovoltaic cells and the light extraction efficiency of organic light-emitting diodes are improved when the surface is wrinkled. Generating diffraction patterns on materials with

appropriate optical properties optical focusing devices can be created in a low cost production. Since the surface wrinkling of polymers can be induced by external stimuli reversible patterns can be used to adjust the optical properties of devices. This effect is used in reversible dual-patterned surfaces showing a dynamic fluorescence and wrinkling. These structures can be the base for smart materials applied to smart displays or mass storage. [1, 2]

In the field of electronics wrinkles or ripples surfaces enable the fabrication of stretchable electronics. An external stress is absorbed by the wrinkles making the system flexible and stretchable. This property enables the application as wearable electronics which require flexibility but also need to be restored to their original shape. Furthermore wrinkles structures are used as physical sensors. Since the change of physical factors like pressure, moisture or strain induces variations in the structure also the electrical properties are changed and can be measured. Concerning the importance of regenerative energy sources triboelectric energy becomes an interesting alternative and also on this field structured surfaces play an important role. It was demonstrated that nano and micro structures on the surface of the materials in contact lead to an increased surface charge density which makes the system more efficient. [1, 2]

The large number of applications demonstrate the importance of periodically micro and nanostructured surfaces and show that it is important to develop low cost production methods as well as control the formation of these structures. To achieve this goal a series of techniques was developed and studies in the last years ranging from indirect methods like swelling or shrinkage to complex multistep processes. An interesting phenomenon resulting in periodic wavy pattern which is less explored in context with surface structuring methods is surface rippling. Although it can be observed at different length scales and results in large area structuring within a single step process. Additionally it can be applied to different types of materials as shown in the following section.

1.2. Surface rippling created by scanning probe lithography

Surface rippling is a phenomenon observed at different length scales and on nearly each material. What is meant by surface rippling? This effect describes a wavy pattern or wrinkles on surfaces created by an air flow or sliding and rolling contacts. It can extend over wide length scales like the pattern in the sand of the desert formed by wind shown in Figure 1.1a [5]. On the other hand the wrinkles can spread at the micro scale as shown in Figure 1.1b. Here a so called laser-induced periodic surface structure (LIPSS) on carbon fibers [6] is shown. Its periodicity is in the range of micrometers and the phenomenon can be observed on almost all types of materials [7]. Please note that the structures are not the result of ablation. Figure 1.1c shows an example for surface rippling at the (sub-) nanometer scale. In this case a polymer surface was scanned by an atomic force microscope tip resulting in a pattern surface. [8] A ripple pattern can also be formed at the nanometer scale as demonstrated in Figure 1.1d,

where a scratch on a KBr crystal is shown. The groove and the pile up with the rippled pattern was induced by scratching the surface with an atomic force microscope tip several times. [9]

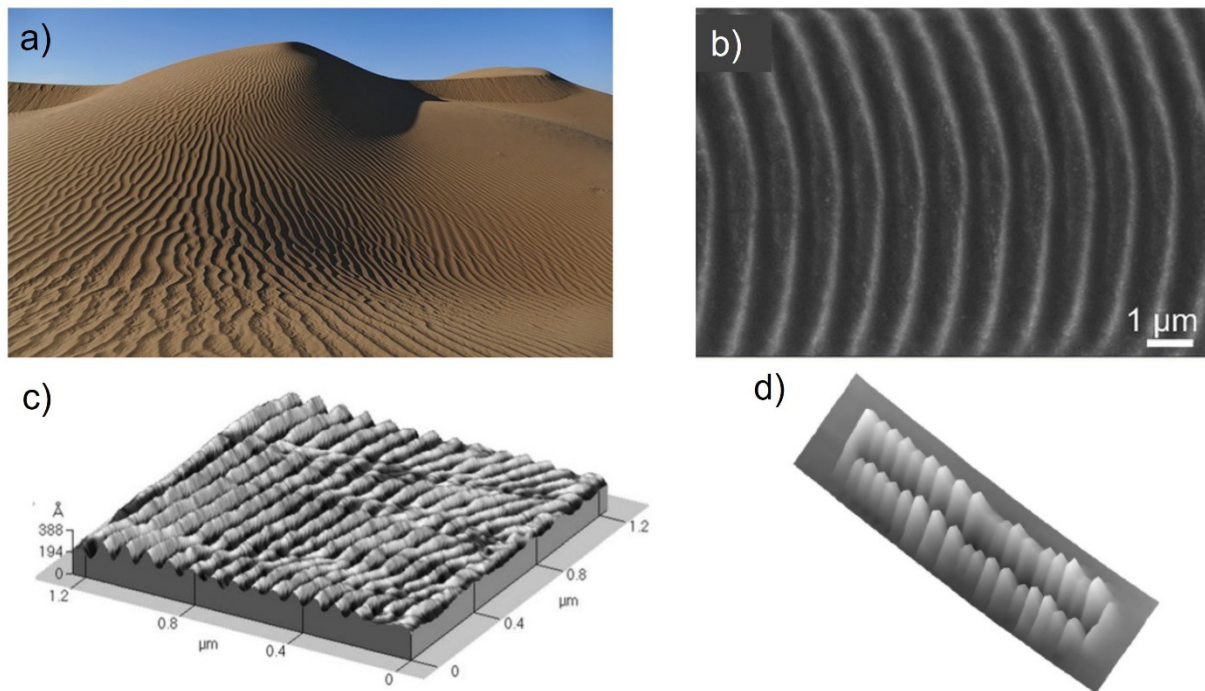


Figure 1.1: Surface rippling at the a) macroscopic scale on sand dunes (desert Dasht-e Kavir (Iran), Image: Xenia Kuhn [5]), b) μm scale on carbon fibers [6] and c) on a polymer surface (PET) [8] d) at the nm scale on a crystal (KBr) [9].

In materials science and nanotechnology the formation of rippled surfaces scanned by a sharp indenter like an atomic force microscope tip in a raster or zig-zag path was frequently described in the past years [8-12]. Especially compliant surfaces of polymer films were used to investigate surface rippling. All of these groups produced and reproduced periodic rippling structures, but controlling the orientation was a less studied aspect. Rippling effects caused by scraping with a sharp indenter were also observed on brittle materials like crystals [9]. But they were not detected on brittle amorphous materials like glass surfaces before [13, 14].

As described above the formation of a rippling surface structure at the (sub-)nanometer scale can be induced by scanning a material with a sharp indenter. This technique is a category of nanolithography called scanning probe lithography. Nanolithography in general covers a series of techniques to structure different materials at the micro- and nanometer scale [15]. Scanning probe lithography comprises techniques using a sharp indenter to modify a material locally. Surface can be changed by a series of physical and chemical interactions between tip and surface including mechanical material removal, thermal treatment, (thermo-)chemical reactions or current induced effects. Material can be added or removed. One of the advantages of scanning probe lithography over other common nanolithography techniques is that it structures a surface in a single step process. In the case of surface rippling induced by scanning with an atomic force microscope the surface can be imaged during manipulation additionally. [16, 17]

1.3. Wear and nanoparticle release

Since a series of applications of rippled or wrinkle surfaces are based on polymeric materials or surfaces the risks of polymers especially the degradation into micro and nanoparticles has to be considered. It has to be mentioned that such sliding, scanning or scraping processes used for structuring by scanning probe lithography cannot occur without friction [8, 18]. Friction leads to wear and can result in abrasion and particle release. Uncontrolled polymer (nano-) particle release to environment is a problem of great concern in our decade. Polymer micro- and nanoparticles were found on terrestrial samples [19, 20], in oceans and freshwater systems [21-25], in the air [26, 27] and snow samples from the Alps [28, 29] and the Antarctic [30]. Due to their small size they are difficult to localize and cleared away and can be easily transported over very large distances. In consequence the particles accumulate in environment and are ingested by organisms. On this way they become part of the food-chain and end up also in human organisms. Inside the organism they create threats caused by their physical size on the one hand and the chemical composition on the other hand. [31-33] For these reasons there is no doubt that plastic pollution has to be reduced and controlled. But the knowledge about the release of micro- and nanoparticles is still very limited. Since a series of research works focus on the degradation caused by a combination of physical and chemical factors like mechanical stress, UV radiation and water [34, 35], the exclusive degradation by physical processes is less pronounced. Especially the observation of individual nucleation and detachment of single polymer particles by abrasive processes is a challenging issue and fundamental studies on this topic are rare.

1.4. Aim and outline

This thesis expands the knowledge of surface rippling induced by scraping amorphous materials with a sharp indenter. Two (compliant and brittle) fundamental materials were investigated: polystyrene and silica glass.

First of all the influence of boundary orientation of the scanned area on the orientation of the ripple pattern was studied. Coming from the known ripple formation on squared areas on compliant surfaces scanned by a sharp nanoindenter the orientation of the boundaries was changed systematically in order to control the ripple orientation. The obtained results may help to produce surface ripples with defined orientation over large distances.

In a second step squared structured areas were scanned repetitively in order to investigate wear processes ending in nucleation and detachment of single particles. Here atomic force microscopy allows to study the underlying processes *in situ* and the observation of the damaged surface afterwards. From the obtained results conclusions on the physical processes leading to particle detachment can be drawn.

The third and last part deals with periodic structures observed inside scratches on glass surfaces. The influence of scratch velocity on the periodicity of the structures was investigated

systematically. Therefore a glass surface was scratched by a diamond tip with increasing velocities and a constant load creating plastic-elastic surface deformation. The rippled structures inside the scratches represent a fundamental result and may help to produce periodic structures on glass surfaces by scanning processes similar to the surface rippling on compliant surfaces.

The results on polymeric surfaces can pave the way for new methods for low volume production of structured surfaces with a well-defined structure orientation. Simultaneously it provides fundamental information about the detachment of polymer particles under mechanical stress. The results on the glass surface can help to develop efficient methods for structuring of brittle materials and may help to replace polymeric materials for applications not requiring the material specific properties of polymers.

This thesis is organized as follows:

Chapter 2 describes the background of the used experimental methods. First scanning probe lithography is introduced in the context of nanolithography. Since atomic force microscopy was the main technique used in this thesis as a scanning probe lithography method as well as an imaging method the atomic force microscope in general and especially the employed working modes are explained. Nanoindentation and nanoscratching is the second method focused in this section. Since the thesis will focus on the connection between wear and stick-slip motion both physical phenomena are described. Additionally a brief description on spin coating as the fabrication method for the investigated polymer surfaces is given.

Chapter 3 deals with rippling effects on polystyrene surfaces induced by scanning process with a sharp tip of an atomic force microscope. After an explanation of the background and motivation the experimental setup is described in order to highlight the progress with respect to state-of-the-art research. Then the results of the study on the boundary effect on the ripple orientation are presented and discussed. The last part includes the results of particle release induced by a repetition of the scanning process and contextualize them with the help of previous results.

Chapter 4 presents the part dealing with glass surfaces. The topic is introduced and motivated. After the experimental setup is explained considering specifics the results are presented and discussed.

Finally Chapter 5 concludes the thesis, mentions some open questions and gives an outlook on potential following studies.

The thesis is finished with the appendix including additional images and graphs, the acknowledgements and references.

2. Experimental methods and fundamental concepts

In Chapter 2 the used experimental methods and techniques are introduced. First of all an overview of nanolithography is given including a brief introduction in scanning probe lithography. Since atomic force microscopy is the mainly used technique as scanning probe lithography technique and simultaneously for surface characterization of nanostructures, atomic force microscopy modes used in this thesis is focused. Nanoindentation and -scratching as the second main technique of the thesis is described. The following section provides an overview of wear and stick-slip motion. Both physical phenomena are related to sliding contacts occurring in atomic force microscopy scanning and nanoscratching. Additionally a brief introduction in spin coating is given since this is the techniques used for preparing the polymer samples used in this thesis.

2.1. Nanolithography

Nanolithography techniques can be divided into four categories:

- **Photolithography** covers techniques using light to micro- and sub nanometer patterns. The geometric design is transferred by an optical mask and the photoresist either hardens or break down when it is shut by light. The softer part is removed by an appropriated solvent and the pattern is formed. [36]
- **Scanning lithography** covers a group of techniques using a beam or a tip scanning a surface and transferring a geometric design directly to the material by mechanical or chemical processes. [16]
- **Soft lithography** uses elastomeric stamps, molds or conformable photomasks to fabricate replicating structures. [15]
- **Further techniques** using miscellaneous physical or chemical effects to create structures. [37]

All of these categories covers a series of techniques, which can be categorized into subgroups shown in Figure 2.1.

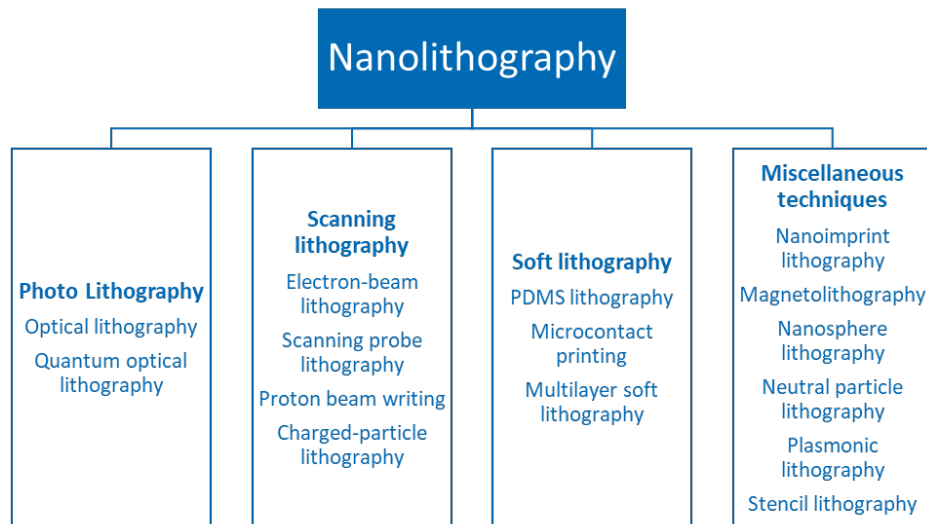


Figure 2.1: Nanolithography categories and techniques.

The common technique used for metal-oxide semiconductor fabrication is optical lithography at a wavelength of 192 nm. This technique combines high throughputs and low production costs, but has reached its physical limits. Mask- and stamp-based techniques need high-volume production to work economically. Low-volume or prototype production require flexible tools without the overhead of mask or stamp fabrication. This requirement can be fulfilled by techniques which transfer the geometric structure directly to the material. A series of beam-based techniques were developed addressing this issue. Electron-beam lithography is the dominant one within this group of techniques. Parallel scanning probe lithography (SPL) which uses a sharp tip to modify the surface locally becomes an interesting alternative. It is suitable to a wide spectrum of materials, enables an inherent inspection, allows an accurate positioning and in contrast to beam-based methods it can be performed under ambient conditions. An essential advantage of SPL is that it is a single step process achieving a high resolution in the range of sub-10-nanometers. The most frequently used technique for SPL is atomic force microscopy. [16, 17] Technical details about scanning probe lithography performed by atomic force microscopes will be included in the following section.

2.2. Atomic force microscopy

The atomic force microscopy (AFM) was invented by *Binnig et al.* in 1986 [38] as a category of scanning probe microscopy techniques. A scheme of the AFM setup is shown in Figure 2.2. In principle a sharp tip mounted on a flexible cantilever physically scans the surface of the sample. The tip is moved by piezoelectric scanners, that allows an extremely accurate movement in x-, y- and z-direction. By the interactions between the tip and the sample surface the cantilever is bend or twist while the tip is scanning the surface. A laser beam focused on the end of the cantilever and reflected onto a quartered photodiode measures the deflection and twist of the cantilever. When the cantilever bends or twists the position of the laser spot on the photodiode changes. In consequence the photodiode voltage regulates the position of

the tip via a feedback loop in order to balance the bending caused by topography and to control the force between tip and sample. With the resulting movement the system can generate topography or other force maps of the surface. The twist of the cantilever provides information about friction between sample and tip. [38-40]

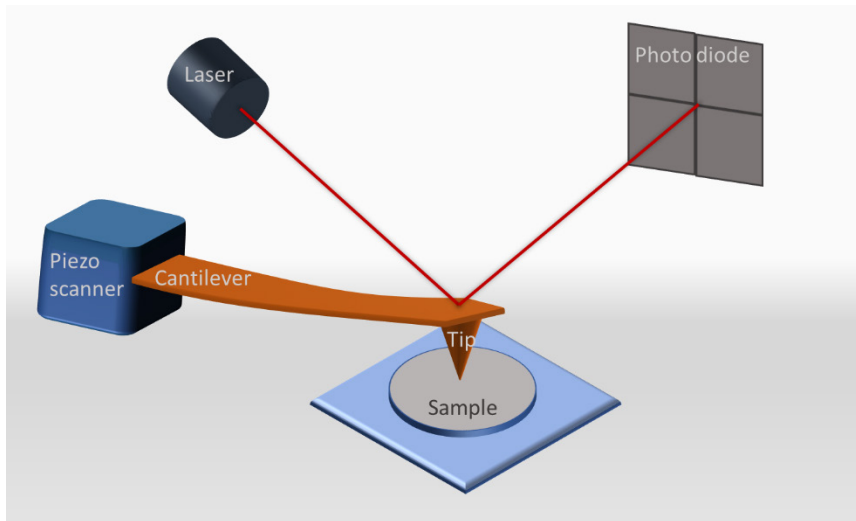


Figure 2.2: Scheme of the principle AFM setup.

AFM technique provides a series of modes for measuring surface properties offering a wide spectrum of applications. To summarize it briefly AFM tip can scan the surface in contact mode, in an intermittent mode (tapping mode) or in non-contact mode. Additionally to scan modes a defined normal load can be applied in order to create (single) nanoindentations. Since contact and tapping mode are used in this thesis the following section will focus on these modes. In contact mode the tip is moved laterally over the sample surface. Caused by height differences on the surface the cantilever is bent leading to a change in the position of the deflected laser beam on the photo diode. In the most common force controlled setup the height of the cantilever or respectively the tip is adjusted via a feedback loop by piezo scanners. In this mode all parts of the sample experience the same normal load. In contrast to this approach the tip can be moved over the surface in constant height leading to different normal load applications depending on the height changes of the surface. Since the tip is in permanent contact with the surface repulsive forces determine the interaction between tip and surface. The surface can be scanned with the tip in contact at trace and retrace or the tip can be retracted by a certain height at retrace (so called “hover mode”). Next to contact mode the AFM can work in non-contact mode in which the interaction is determined by attractive forces between tip and surface. [41, 42]

Since the bending and the resulting force applied by the tip depend on the spring constant the exact value has to be calibrated for each cantilever or tip respectively. Cantilevers provided by manufactures generally contain a data sheet including the specifications, like spring constant. These values are calculated from cantilever geometry and not experimentally determined for each single cantilever. In consequence the spring constant has to be measured before an AFM

measurement is started. Several approaches are provided to determine the spring constant experimentally.

Common approaches are based on thermal noise under consumption of harmonic oscillation of the cantilever and its damping. The thermal noise method measures free fluctuations of the cantilever caused by thermal vibrations from the environment. It is available at ambient conditions as well as in liquids or increased temperatures. The fluctuations are measured in the AFM as vertical deflection against time. To exclude time-dependent influences like thermal drift the measurement is analyzed frequency dependent. A simple harmonic oscillator fit is used in order to calculate the energy of the resonance (area under the curve). Since the energy is given by the spring constant k and the average value of vertical deflection of the cantilever, spring constant can be calculated. The usage of correction factors can make the calculation more accurate. This method was described by *Hutter and Bechhoefer* in 1993. [43]

The contact-based spring constant calibration uses the well-known Hooke's law $F = -k \cdot x$ to calculate the spring constant. Therefore the distance the cantilever deflects at a certain voltage measured by photodiode defined by the sensitivity is needed. The sensitivity is determined by a force distance curve acquired with the cantilever on a hard substrate. Since the repulsive contact region is linear for hard surface and tip the factor for converting volts on nanometers can be easily done. The achieved values can be used for calibration the applied loads to the surface of interest. [44]

A spring constant calibration using the geometrical dimensions of the cantilever and the physical properties of environment along with the thermal noise measurement was described by *Sader et al.* [45]. This method calculates the spring constant and sensitivity simultaneously without requiring a force distance curve on a hard surface. But it is only applicable to rectangular cantilevers with a length much larger than the width. Finally the spring constant is calculated from the density of surrounding medium, cantilever dimensions and a well-defined hydrodynamic factor. By correction factors the method was adapted to be applied also to non-rectangle cantilevers. [45, 46] Commercial AFM systems provide an automated process to calculate spring constant and sensitivity with one or several of these methods.

Since in contact mode the applied load at the tip-sample contact can be controlled quite exactly this method is used not only for imaging but also to modify or manipulate the surface in sub-micrometer down to nanometer scale. So the AFM became a frequently used technique for scanning probe lithography (SPL) at which the tip is used to modify the surface mechanically in a controlled way without a subsequent development step. SPL includes several approaches with the goal to create 3D-patterned surfaces with defined geometric features. Surfaces can be structured directly by mechanical removal of material induced by scratching with the AFM tip. With the help of an integrated feedback loop and scanning a raster complex 3D nanostructures are producible. For compliant and soft surfaces the material can be deformed instead of removed. Both processes are induced by friction between the tip and the surface. Thermal and thermochemical SPL use heat to modify the material mechanically or change chemistry locally. Nowadays the tip is heated by a current flow in the cantilever resulting in an increased temperature in the contact area of tip and surface. In

consequence the heat is highly localized to an area on a few nm². For bias-induced SPL electric bias is used to induce electrochemical processes. By applying moderate voltages to the tip high electric fields can be achieved due to the small contact area between tip and surface. Oxidation SPL is based on an anodic reaction between tip and surface and induces an oxidation of the contact area. [16, 17, 47, 48]

Next to the contact and non-contact mode the AFM offers a third frequently used mode: the so called tapping mode. It is an intermittent mode in which the tip is oscillating with a frequency close to its resonance frequency. When the tip approaches the surface the amplitude changes due to interactions between tip and sample. The change is detected and used in the feedback loop to adjust the position of the tip by piezoelectric scanners in order to keep the oscillation amplitude constant. Since this mode can be applied to a series of materials and the interaction between tip and surface is minimal this mode is frequently used for topography imaging. [41]

2.3. Nanoindentation and -scratching

Nanoindentation is an adaption of conventional indentation hardness tests in order to study mechanical properties developed in the 1970s. It enables the testing of small volumes within a well-defined area on the surface due to a high spatial resolution to place the indenter. [49] While indentation process load and penetration into surface is measured. The resulting load-displacement curves provide information about mechanical properties. Together with the resulting impact especially its area and depth the elastic modulus and hardness can be determined. [50] The used tips indenting the surface with a defined load have a precise tip shape. As known from indentation tests at larger scales a series of tip geometries are available but usually a Vickers or Berkovich tip (shown in Figure 2.3) is used.

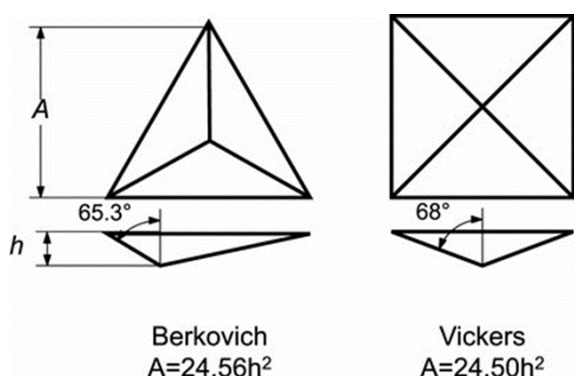


Figure 2.3: Geometry of a Berkovich indenter and a Vickers indenter. [51]

Typical loads applied by nanoindenters are in the range of mNs which is typically used for harder materials like ceramics, glasses and metals. By using AFM technique indentation tests with applied loads of nNs up to μ Ns can be performed. With such low values of normal loads even soft materials like polymers can be indented in a defined way. [52]

Next to nanoindentation tests nanoscratch tests offers a test regime for measurements at the micro- and nanometer scale. They can be performed on commercial nanoindenters and provide a powerful tool for investigations on mechanical and tribological properties down to nanoscale friction. [53, 54] Nanoscratch tests are frequently used to determine adhesive strength and fracture properties of coated systems [55, 56] and they are the standard measurement for scratch resistance of glass surfaces. [57] The applied normal load can be kept constant or variate while scratching. Several parameters like normal load, displacement into surface or lateral force can be measured *in situ* and plotted afterwards. The resulting force – distance curves and displacement – distance curves provide important information about the scratch behavior of the material. Combined with the characteristics of the resulting scratch groove information about the wear mechanism can be obtained.

2.4. Wear

Wear describes the damaging of surfaces by deformation or removal of material resulting from mechanical interaction of surfaces in relative motion. Different criteria can be used to classify it: relative motion, interaction of elements or interaction mechanisms, damage severity or damage mechanisms. In engineering context it is reasonable to classify wear by the underlying mechanism. The main wear mechanisms are described in the following part and schematically shown in Figure 2.4. In real life these mechanisms can occur in parallel or combined. [58-60]

Adhesive wear occurs in frictional contacts, mainly in sliding contacts but also in rolling contacts or impacts. When two surfaces are pressed together, in the contact zone solid-state welding can occur. Caused by a relative motion of the two surfaces a shear stress is induced in these welding zones resulting in breakage. By adhesion between the damaged material and the other surface material is transferred from one surface to the other. This way protrusions above the original surface can be generated. Severity of adhesive wear is determined by and affects surface roughness. Also surface energy is affected. [58, 59]

Abrasive wear occurs in sliding contacts between a harder and a softer material. The material scraped off either by hard particles (three-body abrasion) or by asperities pressed against each other (two-body abrasion) and moved along a surface. Three subcategories of abrasive wear can be distinguished: plowing and cutting wear and fragmentation. Plowing wear is characterized by the displacement of material to the side out of the scratch groove. In consequence a pile up at one or both sides is formed by plastic deformation. Typically the material is not detached from the surface. Cutting wear takes place when material is separated from the surface without or only little displacement to the side. Fragmentation starts with material separation by cutting which initiates localized fracture. Crack propagation around the wear groove occurs leading to additional material loss. The deformations on the surface caused by abrasive wear generates defects which paths the way for active atoms like oxygen to diffuse into the surface. In consequence the mechanical properties of the surface can be changed by chemical reactions. [58, 59]

Surface fatigue, pitting and impact wear are caused by cyclic sliding contacts or impacts and generates microcracks at or below the surface. By crack propagation particles from the surface are detached leading to craters with sharp walls. [58, 59]

Another type of wear is fretting which is caused by repeated rubbing between two surfaces leading to material removal from one or both surfaces. It originates from vibrations or temperature changes and creates large amounts of powder debris. [58, 59]

Next to physical interactions wear can be caused by chemical reactions between the surface material and the surrounding medium leading to corrosion and oxidation wear. This type of wear can occur in dry and lubricated contacts. When corrosion occurs is supported by tribological stress it is called tribocorrosion. [58, 59]

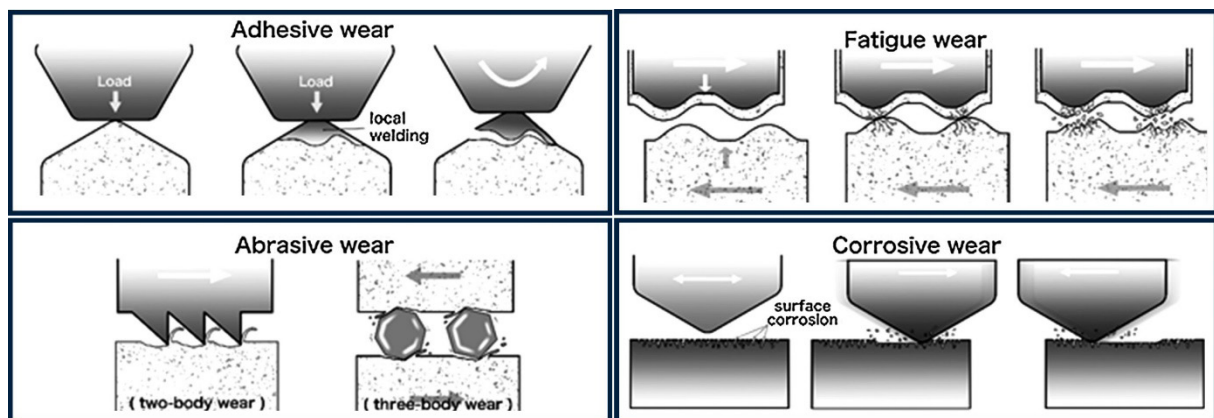


Figure 2.4: Schemes of main wear mechanisms. [58]

2.5. Stick-slip motion

Recording the lateral or friction force during scan or scratch processes provides important information about the behavior and the motion of the tip during sliding and the response of the material. The friction coefficient μ is given by the ratio of lateral force and normal force [61]. But not only the values itself also changes in the lateral force – distance/time curves provide information. Whereas a smooth curve indicates a continuous movement of the tip across the surface variations in lateral force indicates a discontinuous movement [62]. A periodic oscillation in lateral force along the scratch or scan length is the result of a stick-slip motion. The motion is characterized by alternating stick and slip phases known from different length scale. Probably the most popular example for a stick-slip motion is the displacement of crustal plates against each other [63]. At the macroscopic scale the stick-slip motion can be explained by a simple model. A scheme of the model is shown in Figure 2.5a. When a rigid block with a certain mass is lying on a flat surface connected to a spring and pulled by a constant velocity it sticks a certain time. In this stick phase the spring is stretched resulting in an increasing spring force. When the spring force overcomes the static friction force between the block and the surface the block suddenly slips. Simultaneously the movement is slowed down by the kinetic friction force till it stops again. Thereby the movement of the block is damped following the principles of a harmonic oscillator. In consequence the recorded lateral

force alternates in the typical saw tooth shape. [64, 65] To describe the stick-slip motion at the atomic scale the Prandtl-Tomlinson model is used. The model is shown schematically in Figure 2.5b. It has been developed in the 1920s by Prandtl [66] and Tomlinson [67] in parallel and reproduces the stick-slip motion of a sphere driven elastically on a crystal surface. The sphere is attached to a spring pulled by a certain velocity. The crystalline surface represents an energy landscape. Since the valleys of this landscape represents positions with a minimum energy and the atoms represents energy barriers the sphere sticks in the valleys. Simultaneously it is driven resulting in an extension of the spring. In consequence elastic energy is stored in the spring. The sphere – surface interaction can be described by a sinusoidal potential depending on position x and time t . The sphere sticks in the valley till the position becomes instable caused by the velocity and the resulting movement. At this point the sphere slips into the next energy minimum. [68] Since the AFM technique enables the recording of the lateral force with high accuracy this effect is used for friction force microscopy in order to achieve atomic resolution [69, 70]. In this case the apex of the AFM tip represents the sphere and the cantilever the spring. Cantilever holder creates the movement or velocity respectively.

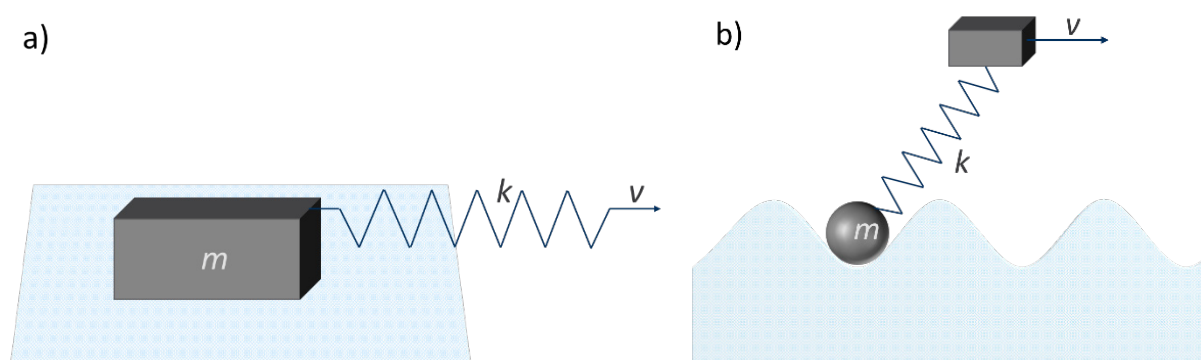


Figure 2.5: Schemes a) of the sliding block model for stick slip motion at the macroscopic scale and b) of the Prandtl-Tomlinson model for stick slip motion at the atomic scale. (both reproduced from [64])

2.6. Spin coating

Spin coating is a technique to produce smooth thin films with a uniform thickness onto flat substrates. A scheme of the process is shown in Figure 2.6a. It is frequently used to deposit solvated polymers, e. g. for the production of photoresists. In principle a drop of the coating material is placed at the center of the substrate. Then the substrate is rotated with speeds of 1000s of rounds per minute (rpm). By centrifugal forces the material is spined off to the edges and forms a film on the substrate. Usually the used solvents are volatile and in consequence they evaporate during spin process or within a short time range after spinning. The resulting film thickness is determined by several parameters like viscosity, concentration of the solvent, spin speed and time and speeding up at the beginning of the process. The influence of the viscosity of solution and the angular velocity on thickness of polymer films was studied systematically by *Hall et al.* [71] in 1990s. The results for polystyrene solved in toluol are shown in Figure 2.6b. With the help of these results the film thickness can be adjusted accurate by the choose of the concentration and spin speed. [71, 72]

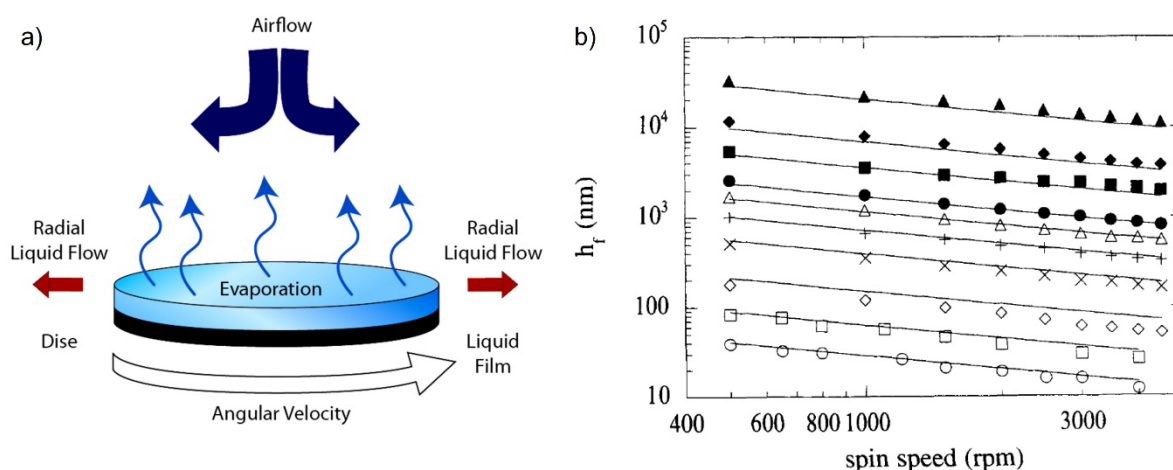


Figure 2.6: a) Scheme of spin coating process[72]. b) Resulting film thickness of polystyrene solutions with different concentrations of polystyrene in toluol depending on the spin speed, concentrations top down: 30 wt%, 20 wt%, 15 wt%, 10 wt%, 8 wt%, 6 wt%, 4 wt%, 2 wt%, 1 wt%, 0,5 wt% [71].

3. Surface rippling on polystyrene

Surface rippling means the formation of periodic wavy pattern on surfaces. As described in Chapter 1.2 it occurs at different length scales. In this chapter the formation of such wavy patterns on a polymer surface induced by sliding or scraping with a sharp indenter is described. Thereby controlling the orientation of the created pattern is focused. In the second part resulting (nano-)particle formation and detachment caused by scraping is studied. After an overview of the state of the art in Chapter 3.1 the experimental setup is described in Chapter 3.2 followed by the presentation and discussion of the results in Chapter 3.3 and 3.4. The presented results have been published in references [73] and [74].

3.1. Background and motivation

When a compliant surface is scanned in a defined pathway (zig-zag or consecutive parallel lines) applying a normal load causing an indentation a typical rippling pattern is formed. This effect was observed on several polymer surfaces like polystyrene (PS) [10, 18, 75], poly(ϵ -caprolactone) (PCL) [8], poly(ethylene terephthalate) (PET) [8, 76], poly(methylmethacrylate) (PMMA), polycarbonate (PC) [10] and more [12, 77]. Since PS is one of the most frequently used polymer for technical applications [31], a large number of present investigations rely on this material providing a series of conditions needed for surface rippling. Temperature influences periodicity of the obtained ripples [10]. As indicated by the results of *Sun et al.* a high molecular weight seems to be a key factor for the formation of ripples [78]. *Gnecco et al.* [18] provided a theoretical model based on the famous Prandtl-Tomlinson model (see Chapter 2.5) to describe the formation of dips and hillocks along a single scan line. In contrast to the original Prandtl-Tomlinson model, the model for surface rippling of polymers starts with an initial flat surface. Since it is assumed that the interaction energy corresponds to the surface profile in the model the interaction energy is also initially flat. The interaction potential between tip and surface is variable and the energy landscape evolves under the influence of the tip. The model includes the indentation rate N , scan velocity v and the lateral stiffness k . A sketch of the model is shown in Figure 3.1a and described phenomenologically below. The mathematical description is given by Equation 3.1 and Equation 3.2 below Figure 3.1.

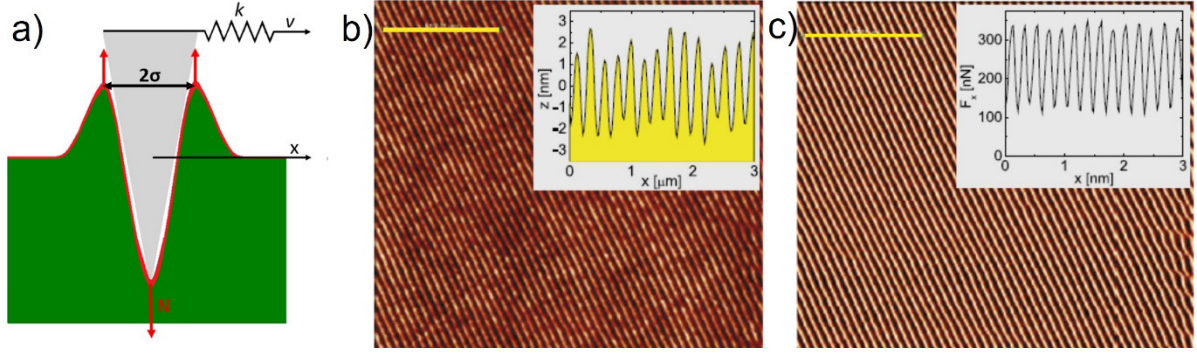


Figure 3.1: a) Sketch of the Prandtl model applied to the formation of surface ripples and the critical parameters. At a given time t a rigid tip apex (in grey) with the width 2σ is indenting the surface. The tip is laterally pulled by a spring of stiffness k and with a velocity v . b) AFM topography image and c) corresponding lateral force pattern accompanying the formation of ripples on a solvent-enriched PS surface. Cross-sections corresponding to the yellow lines are shown in the insets. [18]

The time evolution of the surface profile $h(x,t)$ can be described mathematically assuming that the surface is indented by a Gaussian of half-width σ centered at the tip location $x_0(t)$. The pile up ahead and behind the tip grows in the same way at the distances $\pm 2\sigma$ from x_0 leading to the overall evolution of $h(x,t)$ given by

$$\frac{\partial h}{\partial t} = N \left(e^{-(x-x_0(t))^2/2\sigma^2} + \frac{1}{2} e^{-(x-x_0(t)-2\sigma)^2/2\sigma^2} + \frac{1}{2} e^{-(x-x_0(t)+2\sigma)^2/2\sigma^2} \right).$$

Equation 3.1

The total surface potential changes with time t and tip position x and can be described mathematically by the following equation

$$U(x,t) = U_{int}(x,t) + \frac{1}{2} k(x - vt)^2$$

Equation 3.2

where the potential $U_{int}(x,t)$ represents the tip-surface interaction.

As shown in Figure 3.1a the tip with a width of 2σ is pulled elastically parallel to surface while it locally indents the surface plastically. The tip creates an indentation with a surrounding pile up. The shape of the indentation dip is defined by the geometry of the tip and the height of the pile up increases proportionally with indentation rate N . The spring force pulling the tip laterally increases at a rate depending on the applied velocity v . Depending on the ratio between these two rates the tip follows the spring in a steady way or suddenly overcomes the pile up rim and repeats the process again along the scan line. The result of the second case is a stick-slip motion causing a line of dips and rims. The lateral force increases in stick phase till it overcomes a threshold and suddenly decreases in slip phase resulting in a typical saw tooth pattern in the lateral force – distance/ time curve shown Figure 3.1c. By a repetition of the process in consecutive scan lines with a defined distance b a ripple topography pattern is formed shown in Figure 3.1b. [18]

The influence of the scan line distance was systematically investigated by *Mazo et al.* [79] and described theoretically. Surface patterns induced by scanning with a sharp indenter were simulated using the theoretical model introduced by *Gnecco et al.* [18]. The resulting images are shown in Figure 3.2. It was found that at a given scan line distance a steady region exist in which the ripples tend to orientate in a preferred angle. This locking angle increases with increasing scan line distances. At the edge of scan area ripple follow the orientation given by the boundary, which can be seen in Figure 3.2e) and f). The vertical ripples at the left side of the structured area follow the orientation of the left boundary. The simulated patterns were confirmed by experimental results on PS scanned with an AFM tip.

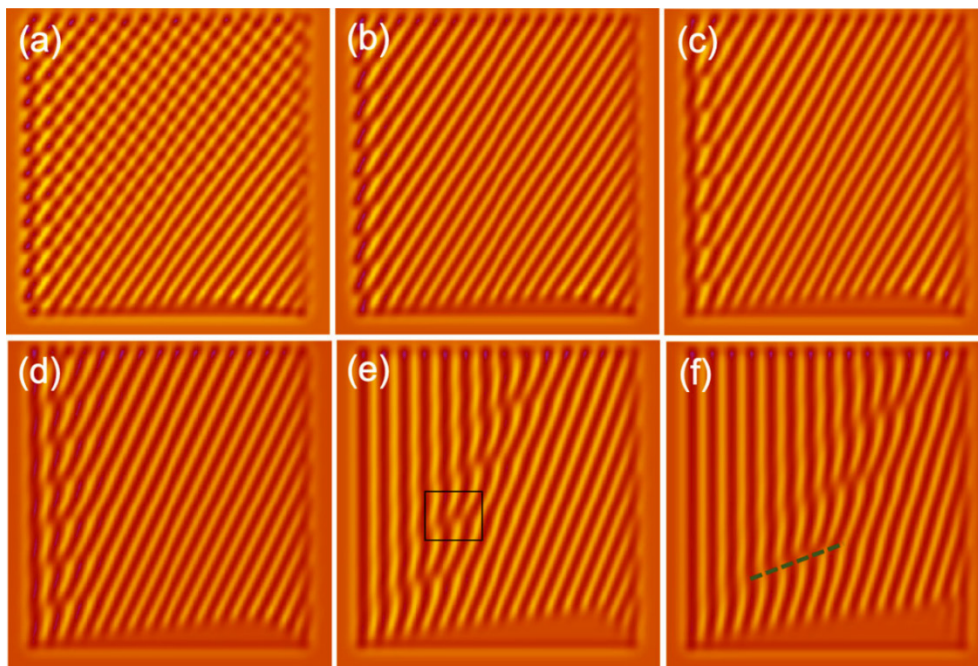


Figure 3.2: a) to f) Surface patterns obtained from the Prandtl model for stick-slip friction. The ratio between scan line distance and tip width has been varied from 0.2 to 1.2 by steps of 0.2. Each frame has a linear size of 4 μm . The rectangle in e) marks a discontinuity in ripple orientation. The dashed line in f) shows the branching also seen experimentally. [79]

That the ripple orientation can be influenced by boundaries was observed by *Napolitano et al.* previously [76]. A ripples pattern inside a circular area, a triangle and a L-shapes area are shown in Figure 3.3. In this case different geometric shapes on a PET surface were structured resulting in different patterns. The applied load variate inside and outside these structures. In order to this load variance the orientation of the pattern changes. In the case of the triangle the ripples are completely parallel to the right side indicating that certain boundary orientations can define the orientation of resulting structures over large distances.

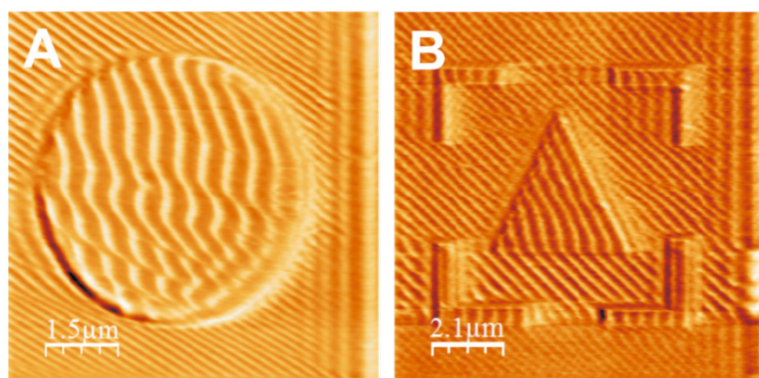


Figure 3.3: Ripple patterns on a) a circular area and b) on an area consisting in a triangle surrounded by four L-shaped regions. [76]

Further parameters influencing the structure were found in experiments with other polymers. The tip trace [77, 80] and cantilever orientation [81] was found to influence resulting rippled pattern on PC. Experiments with PMMA have shown that the solvent can influence surface rippling [82].

These findings will be the basis for processes resulting in rippled patterns with a controlled period, corrugation and orientation. Especially with the help of boundaries changes in directions of ripples can be achieved. When it is possible to control the ripple orientation the application as a scanning probe lithography process is nearly endless. Several geometries could be structured within a single step process and orientation of each geometry could be adjusted. This will provide a time and cost saving process for prototype manufacturing and low-volume-production. For this reasons this thesis introduces an approach for controlling the orientation of periodic structures formed by scanning processes inside a defined area.

Since the scanning and scratching of a polymer surface with a sharp tip cannot occur without friction the resulting wear has to be considered. A well-known problem accompanying with the use of polymer devices is degradation and particle release to environment. Macroscopic plastic fragments degrade into micro- and nanoparticle by a combination of different factors like mechanical stress, UV radiation and water [25]. The small particles are difficult to localize and clear away. Due to their small size and weight they are transported by air or water over large distances and in consequence they sediment all over the world. The microplastics are ingested by organism and enrich along the food-chain. At the end they are ingested also by human beings and can be extremely harmful. Inside organisms they can be transported by blood and, due to their small size, penetrate cell membranes. Inside the cells particles can create serious health problems caused by their size and/or chemical composition. [29, 83-85] As mentioned above PS is one of the most used polymer, even in the context of microplastic pollution a large number of investigations focus on this polymer. PS nanoparticles were found in cells of different organisms and their negative effect on the biochemical processes was demonstrated. [86-89] Even in the brain of the investigated organisms the particles were found, meaning that they can cross the blood-brain barrier. So they have the potential to create threats affecting the neuronal functions. [90]

On the one hand a diminution of polymer applications would reduce the particle release to environment sustainable. On the other hand polymers are unavoidable for certain applications, because their mechanical or chemical properties are required. Here a particle release can be reduced by the reduction of degradation and particle detachment during life circle and correct recycling afterwards. To achieve this goal the first step is to understand the mechanism of particle release. Till now it is known that certain factors, like mechanical stress, UV radiation, water and biodegradation by microorganisms contribute to the degradation of macroscopic plastic fragments into micro- and nanoparticles [25, 34]. Polymer devices are exposed a combination of these factors in life cycle as well as in environment after disposal. But not all of these factors are well understood and can be controlled. Since the influence of UV radiation, water and microorganisms is detailed studied and described [91, 92], the effect of mechanical stress on the degradation at the (sub-) nanometer scale is less pronounced. From the macroscopic scale the behavior of (amorphous) polymers under mechanical stress is well known. The material is ductile and deforms plastic-elastically. With increasing mechanical stress crazes are formed. Inside these crazes a very localized plastic deformation occurs leading to microvoids interrupted by fibrillar bridges. Inside these bridges molecular chains become orientated along the bridges and perpendicular to the voids. When the microvoids coalesce a crack is formed and propagates perpendicular to the mechanical stress (e.g. tensile stress). [93] Since atactic PS has a glass transition temperature T_g of 100°C, it can be considered that these mechanism occurs in PS samples exposed to mechanical stress [94].

The isolated influence of mechanical stress on particle detachment at the (sub-) nanometer scale is a challenging experimental issue. In macroscopic experimental setups the small particles can only be detected indirectly by the decreasing weight of macroscopic fragments. To image detached nanoparticles measuring instruments with resolutions about a few hundred nm or lower are necessary. These resolutions can be achieved by the high tech optical microscopes, fluorescence microscopes, electron microscopes or AFM [95, 96]. In contrast to the light microscopy and electron microscopy the AFM offers a crucial advantage. With the help of the AFM mechanical stress can be applied to the surface by scanning processes [17, 18]. The theoretical technical background is described in Chapter 2.2. The surface can be imaged *in situ* and afterwards without moving the sample [16]. An experimental approach to detach particles and inspect it simultaneously combined with an imaging step afterwards is presented in this thesis.

3.2. Methods

Polymer samples used in this thesis were prepared with a high molecular weight (M_w) polystyrene (PS) solved in toluene and spin coated on silicon wafer as substrates. This process was already used for previous studies on surface rippling of PS. [18, 79, 97] Surface rippling on the PS surface was induced by a scanning probe lithography process using the AFM technique, which is also a known process from literature. [8, 12, 79, 80] Both aspects of experimental setup are described in the following sub chapters.

3.2.1. Sample preparation

For inducing surface ripples by scanning probe processes a polymer with long chains and in consequence a high M_w is needed [78, 98]. In this thesis polymer powders of PS with M_w of $320 \cdot 10^3$ g/mol (Sigma Aldrich) and $320 \cdot 10^3$ g/mol (Polymer Source) were used. The polydispersity index (PDI) of both polymer powders is below 1,02. The polymer powder was solved in toluene with (Merck, 99,9 % HCPL) adjusting a concentration of 6 wt% PS in solution.

The polymer solution was spin coated with 3000 rpm for 1 min onto cleaned silicon wafers followed by drying at ambient conditions for about 24 hours.

Resulting thickness can be estimated by the given conditions (PS concentration in solution and spin coating parameters) around 400 nm. [71]

3.2.2. Scanning probe lithography process

For scanning probe lithography a commercial AFM (JPK NanoWizard4, Bruker) and silicon probes (NSG-01, NT-MDT) with a tip radius below 10 nm were used. Since the used cantilevers have a rectangular shape the spring constant k and sensitivity of the used cantilevers was determined by the method introduced by *Sader et al.* [45] and described in Chapter 2.2. Surface ripples were created by scanning the surface in contact mode within the area to be structured applying a normal load F_N between 100 and 150 nN. In this load range tip penetrates the surface and creates a typical profile. By pulling the tip laterally and scanning in consecutive scan lines a typical ripple pattern is induced. This mechanism was already described with a theoretical model by *Gnecco et al.* [18] By applying this high load to an usual AFM scan area a rectangular or respectably a square area can be structured, which is the basic setup for AFM scanning and was used in Chapter 3.4. A schematical scheme of this experimental setup is shown in Figure 3.4a. In this case boundaries of structured area are perpendicular to fast and slow scan axis which corresponds to x- and y-axis in a Cartesian coordinate system.

To study the influence of boundary effects on ripple orientation (Chapter 3.3) systematically PS surface was structured within defined contours. This was realized by applying multi setpoints while scanning a square area. The corresponding scheme is shown in Figure 3.4b. Geometric shapes of the areas to be structured a binary image was used with a size of

250×250 px. The number of scan lines was determined by the number of pixels in a row. Setpoint and in consequence applied normal load during scanning was alternated between two values during scanning and could be changed within scan lines by a dedicated script. Within the areas to be structured a normal load F_N between 100 and 150 nN (inside the star in Figure 3.4b) and outside these areas a normal load of $F_N = 30$ nN (outside the star in Figure 3.4b) was applied. Scan line distance can be adjusted by the choose of the scan size and was set to $b = 20$ nm by scanning an area of $5 \times 5 \mu\text{m}^2$. Tip was moved with a velocity of $v = 11,3 \mu\text{m/s}$ from left to right during single scan lines and bottom up between single scan lines. Backwards tip was not in contact with surface (so called “hover mode”, described in Chapter 2.2). For similar parameters a steady ripple orientation about 50° is reported by *Mazo et al.* [79]. All angles of boundaries and ripples are referred to fast scan direction (x-axis) and measured counter clockwise (shown in the scheme in Figure 3.8).

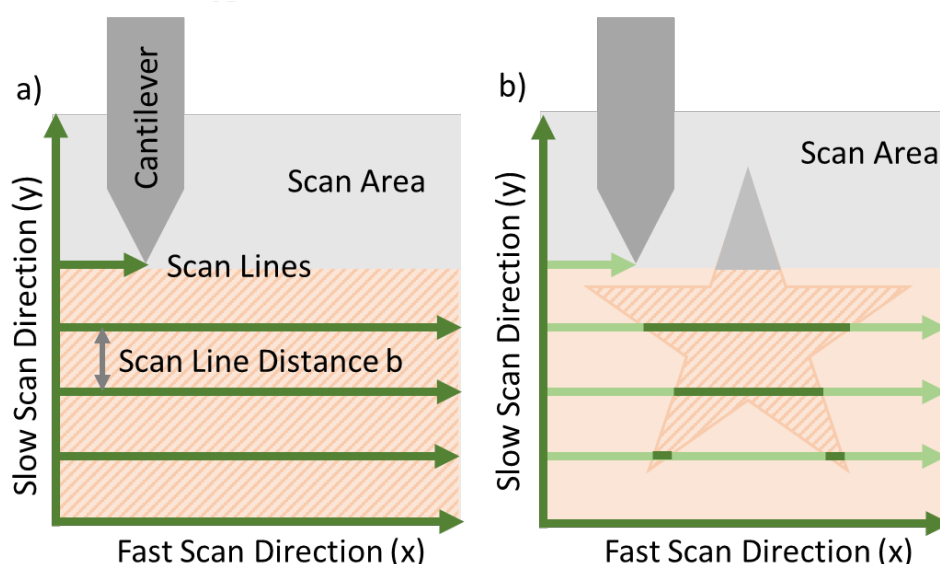


Figure 3.4: Scheme of experimental setup for surface rippling induced by scaping a compliant PS surface with an AFM probe. Scan lines in dark green correspond to a normal load of 100 to 150 nN and scan lines in light green correspond to a normal load of 30 nN. a) structuring a square area with constant normal load and b) structuring a defined geometric shape (star) while scanning a square area with setpoint variation.

3.2.3. Imaging of structures and nanoparticles

To image the so created structured surfaces the AFM itself was used. Structured geometric shapes and squares observed in Chapter 3.3 were images in contact mode with the same tips used for structuring (NSG-01, NT-MDT). To visualize the orientation of the ripples and to quantify the amount of structures with a certain orientation the software package OrientationJ [99, 100] was used. With the help of this software based on the image editing software Fiji (ImageJ) rippled structures were colored depending on their orientation angle. Additionally the amount of ripples with each angle was determined and plotted in diagrams.

Structured squares observed in Chapter 3.4 were imaged in tapping mode using PPP-ZEIHR probes (Nanosensors). In this case a series of areas were structured with different numbers of

scan repetitions per area. Tapping mode images of these areas were acquired afterwards. Due to that experimental procedure the tapping mode images after different scan repetitions shown in Chapter 3.4 were not taken at the same position. They show different structured areas.

3.3. Effect of boundaries on the orientation of surface rippling

The use of the multi setpoint scanning describes in Chapter 3.2.2 allowed the structuring inside user-defined boundaries and open the door to study the influence of straight as well as curved boundaries on the ripple orientation. In a first step defined geometric shapes were structured. The resulting ripple pattern inside a circle, a five-pointed-star, a square rotated by 45° , a heart, a ellipse and a pentagon are shown in Figure 3.5. Depending on boundary shape and orientation different ripple angles can be observed. Due to cantilever motion during structuring from left to right (backwards cantilever is not in contact with sample surface) only the boundary on the left side of structured area can influence the ripple formation.

Figure 3.5 shows shapes with curved boundaries: circle, heart and ellipse; and shapes with straight boundaries: star, square and pentagon. In all shapes with curved boundaries left boundary is continuous and in consequence boundary angle changes smoothly. The first ripples at the left side follow the boundary orientation very well in the circle, the heart and the ellipse. In the lower part of these shapes the boundary angle starts at 180° (circle and ellipse) respectively about 150° for the heart and changes to 90° bottom-up. In this region only one to two ripples can follow the boundary orientation. Then ripples start to reorientate in their preferred orientation under the applied scanning conditions of about 50° to 70° including some discontinuities. Especially for the heart and the ellipse this effect is well pronounced. In the upper part of the shapes, where the boundary angle changes between 90° and 0° , more than three ripples can follow the boundary orientation. But with increasing distance to left boundary ripples tend to orientate in straight lines instead of curves ones. The orientation seems to be determined by boundary orientation in this region.

The shapes with straight boundaries include also different angles in their left boundary. But the angles change suddenly at corners of the shapes and are constant between the corners. In consequence the left boundaries are precisely orientated at 72° and 144° in the case of the five-pointed-star, 135° and 45° in the case of the square and 106° and 35° in the case of the pentagon. Starting with the five-pointed-star behind the boundaries orientated at 72° a series of ripples following the boundary orientation up to the end of the scan line can be observed. In contrast behind the boundaries orientated at 144° only one ripple can follow the boundary orientation. With the second ripple the pattern starts to reorientated to an angle of about 45° . In consequence inside the star different domains with ripple orientations of 72° or 45° depending on the left boundary orientation are formed and well separated. In the square also different ripple orientations between the two left boundaries can be observed. In the upper part with the boundary orientation of 45° this orientation can be kept by the ripples very well. In the lower part with the boundary orientation of 135° the first ripples can follow this

orientation and the reorientation starts. But here the steady angle of about 70° cannot be reached completely. A series of small domains with ripple orientations between 45° and 90° can be observed. Similar effects can be observed in the pentagon. Whereas the ripples following the boundary orientation of 35° covers the whole upper part, in the lower part different domains with ripple orientations between 45° and 106° can be observed. Additionally in both square and pentagon discontinuities inside and between domains can be recognized. Such discontinuities breaking rippled regions have been already reported when scanning a square area without rotation [79]. Since these discontinuities can be observed in numeric simulations of rippling caused by scrapping a compliant surface [79], it can be assumed that they are originated from mathematical instabilities in patterning process instead of material defects in the polymer surface.

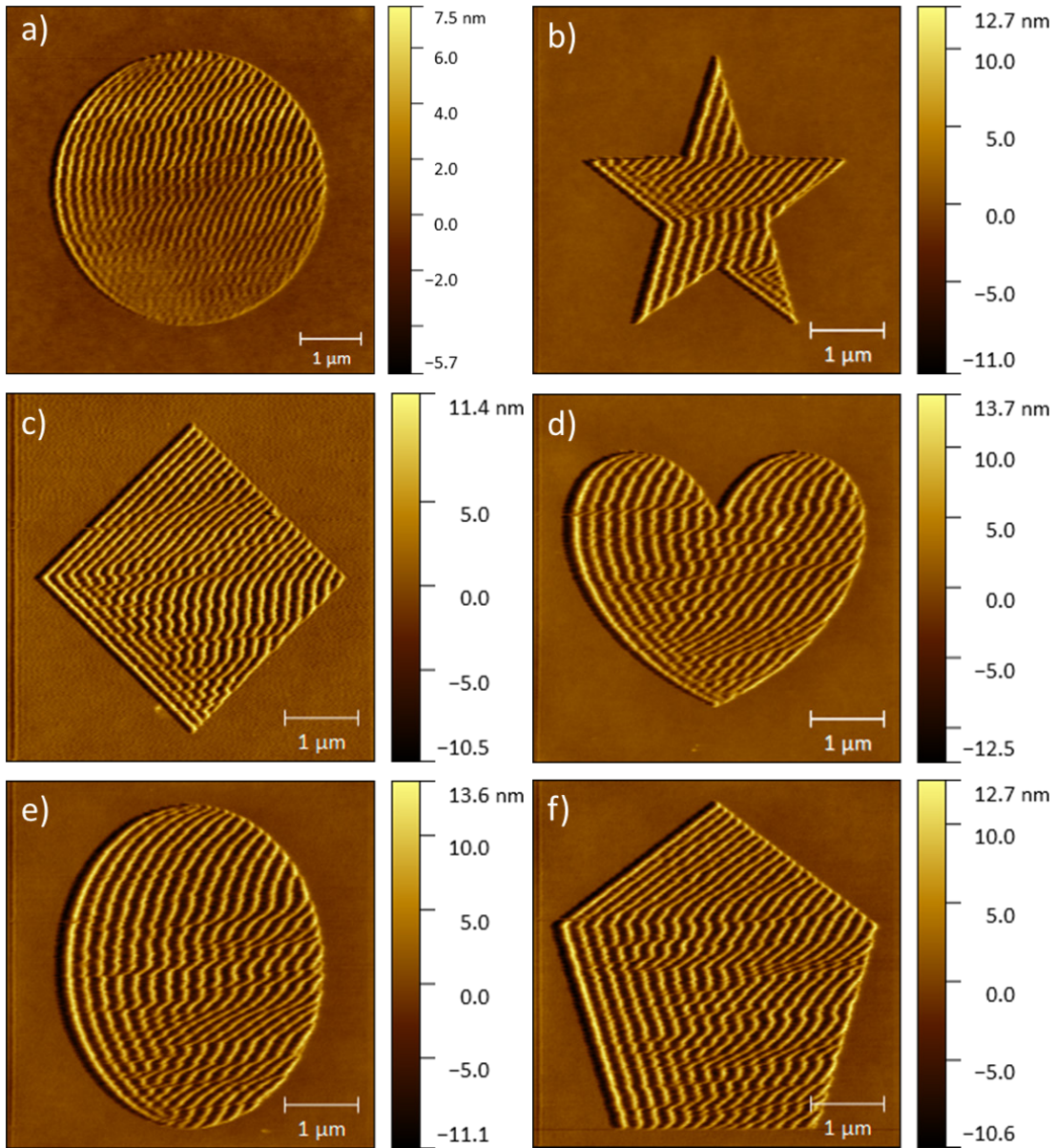


Figure 3.5: AFM topography images of circle, five-pointed-star, square rotated by 45° , heart, ellipse and pentagon structured with the following parameters: a) $F_N = 150$ nN, $v = 10$ $\mu\text{m/s}$, b), d), e) and f) $F_N = 130$ nN, $v = 11,3$ $\mu\text{m/s}$ and c) $F_N = 120$ nN, $v = 11,3$ $\mu\text{m/s}$ and $b = 20$ nm in all cases. [73]

To visualize the ripple orientation AFM topography images of circle, five-pointed-star, square and heart were coloured depending on the pattern orientation using the software package OrientationJ [99]. The resulting images are shown in Figure 3.6. Corresponding colour scale is shown in Figure 3.9. Especially the domains with constant ripple orientation like in the five-pointed-star (Figure 3.6b) and upper part of the square (Figure 3.6c) are well pronounced by the colouring, because these ripples are same-coloured. But also the change in the orientation in regions where boundary orientation cannot be kept by the ripples becomes very clear by the change of colour.

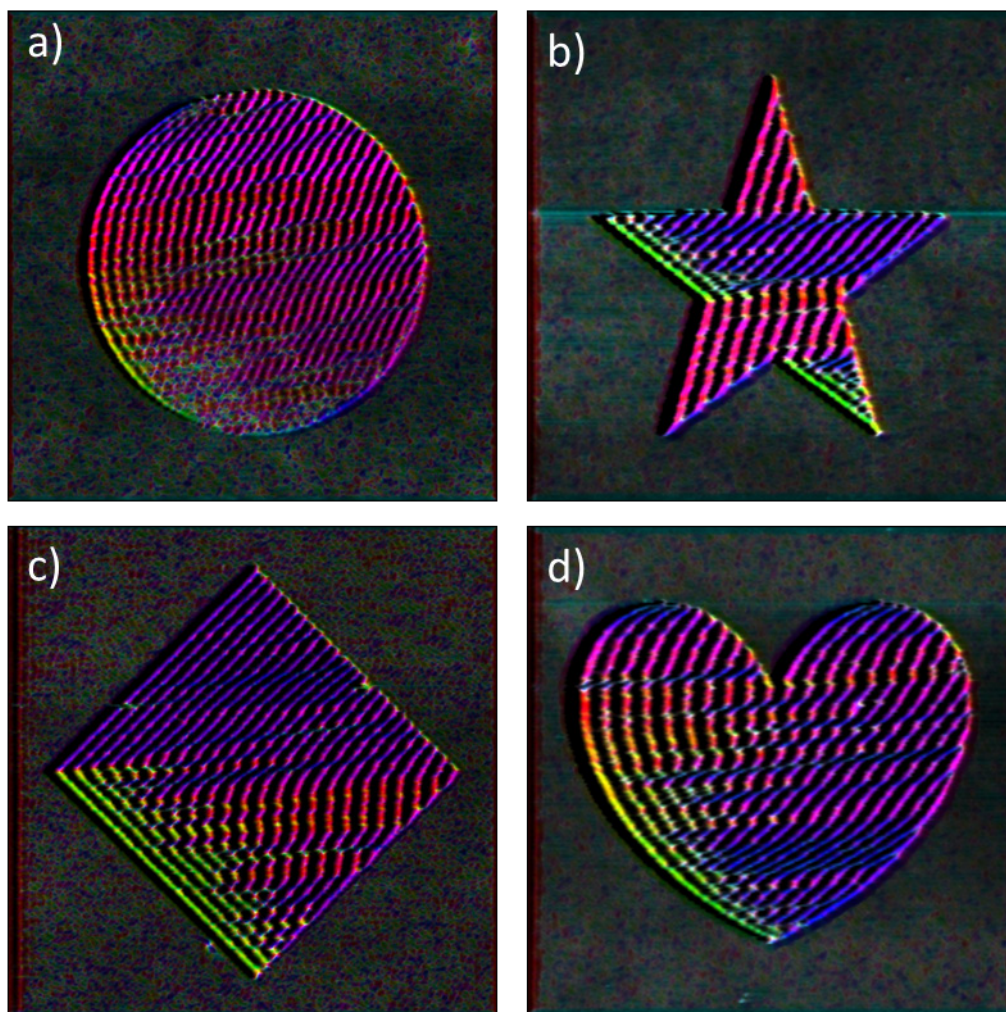


Figure 3.6: AFM topography images coloured depending on their angle according to the scheme in Figure 3.9 corresponding to shapes shown in Figure 3.5 a) – d). [73]

Summarizing the orientation of ripples inside the shown geometric shapes, two ranges of boundary orientation can be distinguished roughly: 1) boundary orientations between 45° and 90° , which can be kept by and 2) boundary orientations between 90° up to 145° , which the ripples cannot follow and try to reorientate in their preferred angle. The preferred angle in the steady region of scanned areas under the applied conditions can be estimated about 70° , which is in the range 1). This leads to the assumption, that the ripple orientation can be

defined by boundary orientation, if the boundary orientation is closed to the preferred orientation defined by scanning conditions.

To study the influence of boundary orientation on ripple orientation systematically a square with the size of $3 \times 3 \mu\text{m}^2$ was rotated counter-clockwise in 10° steps starting with 5° with respect to fast scan axis. The resulting nine structured squares are shown in Figure 3.8. Additionally an unrotated $5 \times 5 \mu\text{m}^2$ square (shown in Figure 3.7) was scanned under the same conditions (polymer sample, AFM probe, normal load, scan velocity and scan line distance) as a reference. The shown height image was taken while scanning the surface in contact mode with the applied load of 120 nN. As described in Chapter 3.2.2 the scan process starts in the lower left corner and the tip moves bottom-up in consecutive scan lines with a distance b of 20 nm. Within the single scan line the tip is moved from left to right in contact with surface. Inside the square three domains with different ripple orientations can be observed. In the lower right corner ripples are orientated in 50° (marked with the blue triangle). Above these domain a second ripple orientation of about 75° can be identified (marked with the green parallelogram). Remaining surface is covered by ripples orientated in 90° and parallel to slow scan axis (y-axis). Compared to the results of *Mazo et al.* who studied the influence of scan line distance on ripple orientation [79] an angle of about 50° to 60° in the steady region should be expected under the given conditions. This angle is reached inside the blue triangle. The small size of this domain can be caused by the small scan area of $5 \times 5 \mu\text{m}^2$. *Mazo et al.* used a scan size of $10 \times 10 \mu\text{m}^2$. In this case ripples affected by the boundary cover a small part at the left side of scan area. In contrast ripples influenced by boundary orientation cover the main part of scan area in Figure 3.7, which is conform with the results for structured shapes with a width of a few periods of ripples in literature. [79] The corresponding cross profile also shown in Figure 3.7 demonstrates the regularity and periodicity of the ripples. The corrugation is in the range of a few nm (8 – 15 nm). Please note that this height image was taken *in situ* during structuring. The measured height combines plastic and elastic deformation of surface. In consequence the resulting corrugation afterwards will be lower. The periodicity of ripple pattern is in the range of 180 nm in this case. Similar values were observed in previous studies on ripples PS surfaces produced under comparable conditions [79, 97]

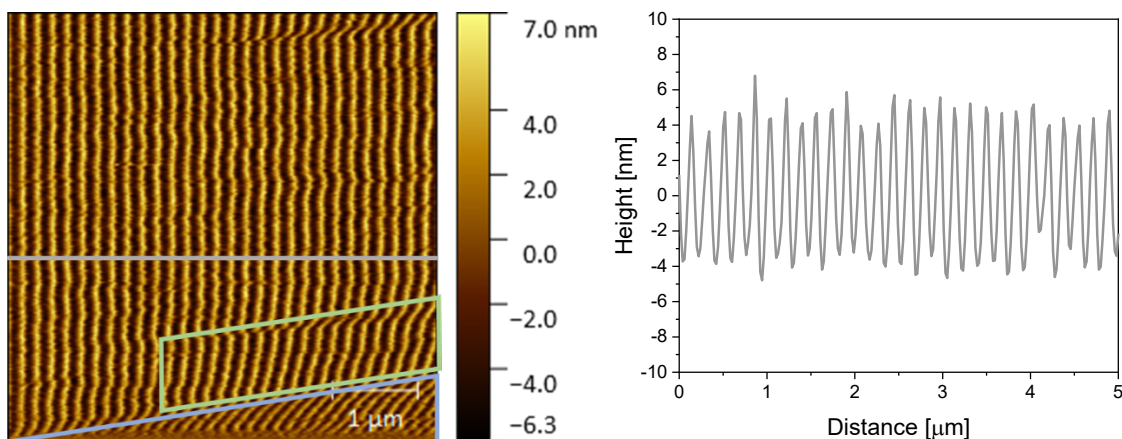


Figure 3.7: AFM height image of an unrotated square obtained while scanning process and cross profile corresponding to scan line marked in grey. $F_N = 120 \text{ nN}$, $v = 11,3 \mu\text{m/s}$ and $b = 20 \text{ nm}$.

The ripple patterns observed in the rotated squares changes with rotation angle and the resulting edge inclination. Starting with the squares rotated by 5° and 15° in the left column of Figure 3.8 nearly the whole area is covered with ripples following the left boundary with an orientation of 95° or 105° . This orientation can be kept by the ripples over the full width of the square except a few discontinuities. Furthermore a small domain in the upper part of the square rotated by 15° is formed with a ripple orientation of about 75° . In the next three squares rotated by 25° , 35° and 45° a transition in ripple orientation can be observed. The domain in the upper part with a ripple orientation below 90° is growing with increasing rotation angle. Ripples in this domain are tilted till the angle of the upper front boundary is reached in the square rotated by 35° and by 45° . This orientation can be kept till the end of the scan line in the square rotated by 45° . In the lower part of the squares an inverse evolution can be observed. The number of ripples following the orientation of the lower front boundary (115° , 125° and 135°) is increased. These regions of the squares are divided into a series of domains with ripple orientations between 45° and the orientation of the front boundary. Starting with the square rotated by 55° the upper left front boundary becomes the dominant one for ripple orientation. Behind this boundary the orientation can be kept by the ripples. The orientation of the lower left front boundary can be reproduced by one ripple in the squares rotated by 55° and 65° , but not any more in the squares rotated by 75° and 85° . Instead of following boundary orientation ripples try to orientate in a steady angle about 50° which is hindered by discontinuities, the influence of boundaries and decreasing size of this area due to rotation. In assumption the ripple orientation is determined by front boundary orientation, if the boundary orientation variates between 45° and 105° , which is supported by topography images coloured by orientation angle in Figure 3.9.

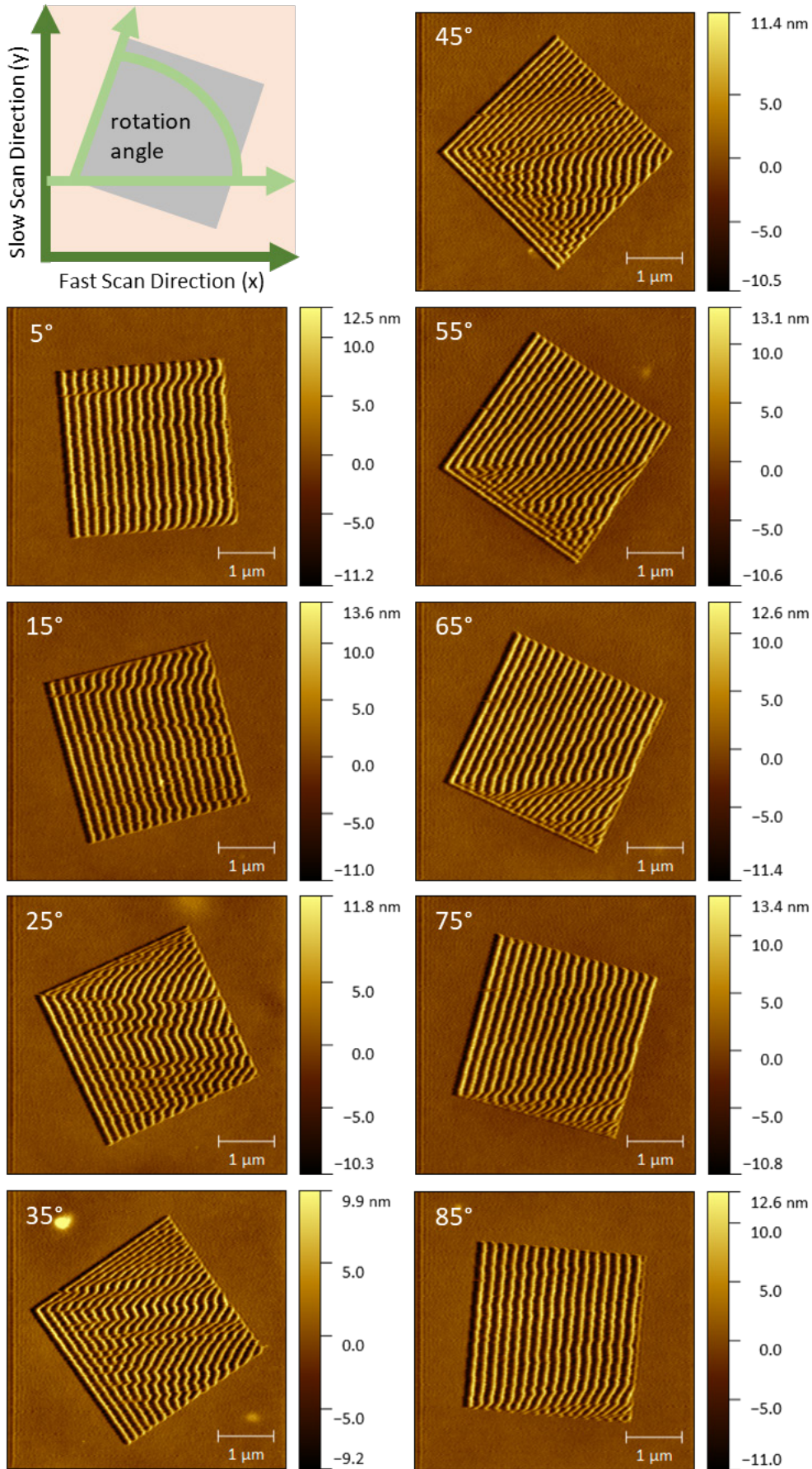


Figure 3.8: Ripple patterns observed after scanning square areas rotated by angles between 5° and 85° corresponding to the scheme at the left side. $F_N = 120$ nN, $v = 11,3$ μm/s and $b = 20$ nm. [73]

By colouring the resulting ripple pattern inside the squares depending on their orientation the change in the ripple orientation becomes visible. Representative for all squares coloured images are shown for the squares rotated by 25° in Figure 3.9b, 55° in Figure 3.9c and 85° in Figure 3.9d. At the left side of the squares straight lines are added in the orientation of the boundaries. Thus the colour of this line corresponds exactly to the angle of the boundary and permits the identification of ripples orientated in the same direction. Figure 3.9a shows the corresponding colour scale. In the squares the different domains can be distinguished by their different colours. Starting with the square rotated by 25° (Figure 3.9b) ripples coloured in yellow, which corresponds to the boundary angle of 115° , can be observed in the lower part. The yellow parts are broken by domains with ripples coloured in pink, which corresponds to an orientation of about 70° . The dominant colour in the upper part of Figure 3.9c is violet, which corresponds to boundary orientation of 55° . In the lower part the transition in ripple orientation is clearly visible by the change of the colour from green (corresponding to boundary orientation of 145°) into blue (45° and pink (70°) domains. In Figure 3.9d the square is covered largely by red ripples, which corresponds to the boundary orientation of 85° and demonstrates, that ripples can follow this orientation over the whole width of the square of about $3\text{ }\mu\text{m}$.

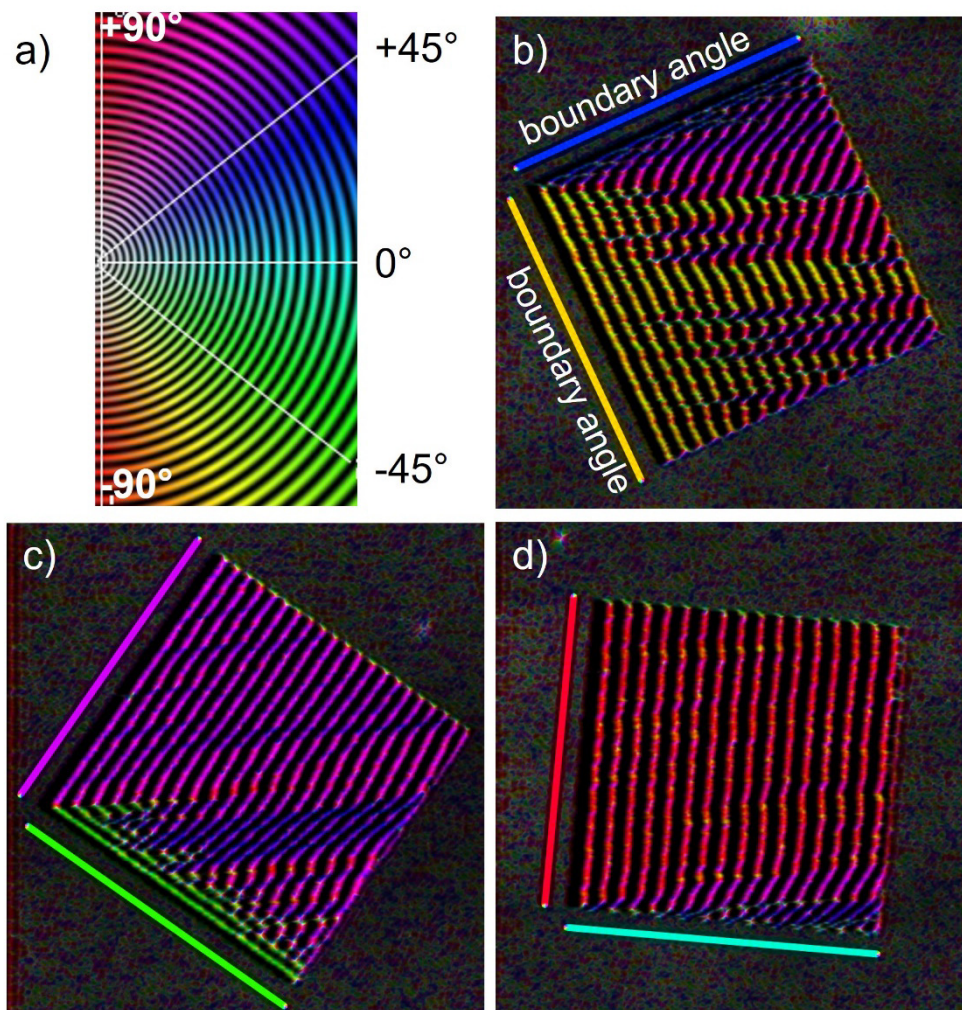


Figure 3.9: a) Colour map used for defining the ripple orientation [99] b) – d) Coloured patterns corresponding to squares oriented at b) 25° , c) 55° and d) 85° in Figure 3.8. [73]

To quantify the qualitative results from Figure 3.8 and Figure 3.9 distribution of ripple orientation for all squares was plotted in Figure 3.10. The main peaks in the graph represents the boundary orientation in corresponding squares, that is followed by ripples. The height of the peaks at the left side of the diagram (-90° to 0° , representing the lower left front boundary) is decreased with increasing rotation angle till it disappears completely at a rotation of 65° . This effect clearly shows, that the influence of this lower left front boundary on ripple orientation decreases. The opposite effect can be observed for the peaks at the right side of the diagram (0° to 90°) representing the upper front boundary. This peak appears at a rotation of 25° and increases up to an rotation angel of 90° . Most of the plotted curves show an additional peak around 50° . This orientation corresponds to ripple orientation in the steady angle observed in some squares. Since the steady angle is less pronounced and not obviously in this graph a second diagram was plotted shown in Figure 3.11. In this diagram the main peaks from Figure 3.10 are shown as dots centred at the edge inclination of the corresponding squares and the ripple orientation inside these squares. The radii of the dots corresponds to the height of the peaks. Once again it becomes clear, that for all edge inclinations ripple can follow the left boundary orientation. But a second information has to be highlighted: the circle at a ripple orientation of 65° is the largest one. This angle is resulting in the most stable patterns. Considering the results of *Mazo et al.* [79] the expected steady angle, that is arose, when scanning a large area under the applied conditions, is in the range of 50° to 70° . In consequence these results suggest, that the orientation of ripple pattern induced by scanning processes can be controlled by a front boundary orientation close to steady angle. The experimental results were confirmed by numerical simulations published in reference [73].

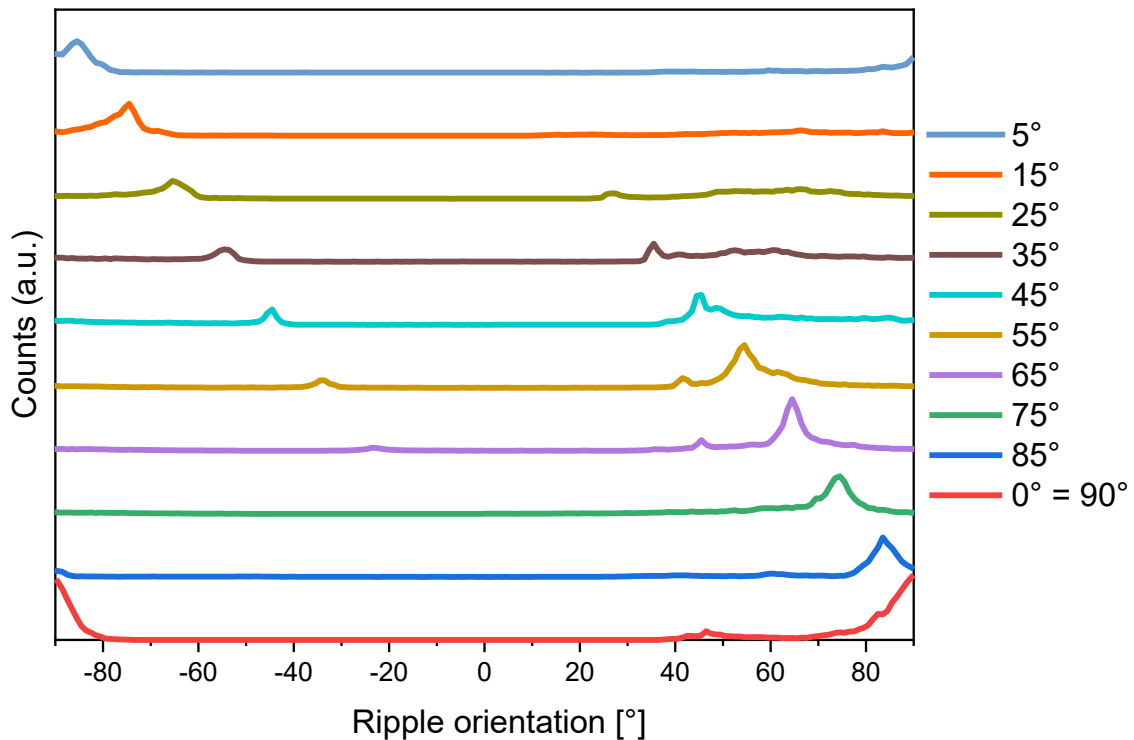


Figure 3.10: Angle distribution of ripple patterns inside the rotated squares shown in Figure 3.8 (5° - 85°) and the unrotated square shown in Figure 3.7 (0° = 90°). [73]

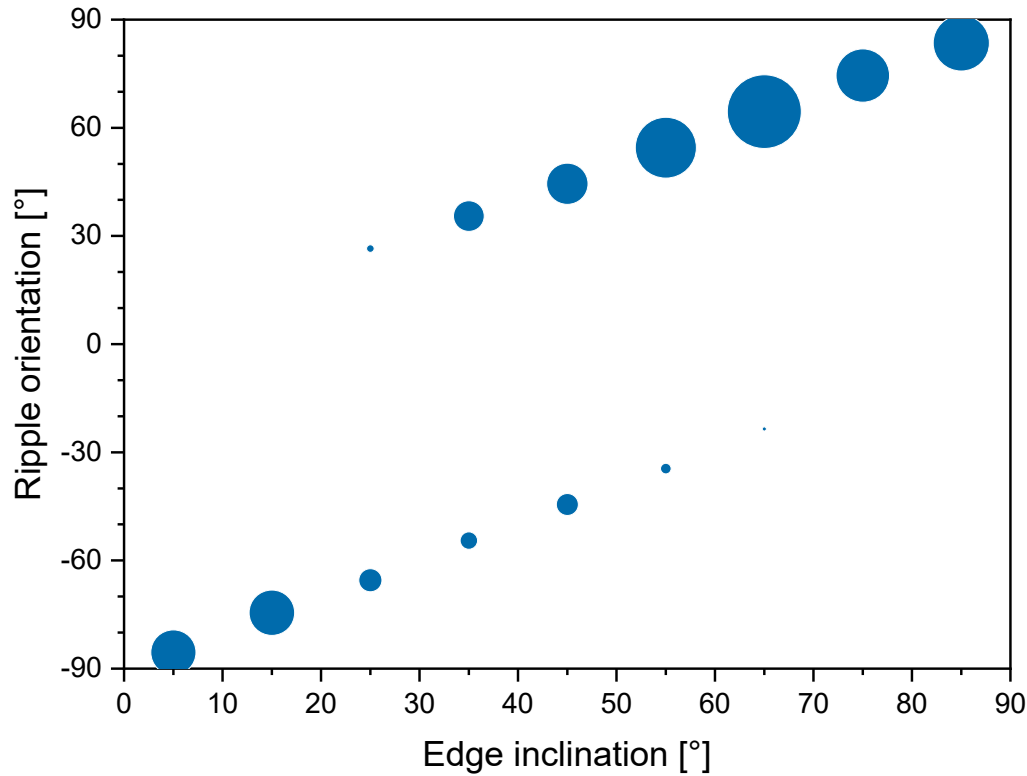


Figure 3.11: Intensity map of the main peaks observed in Figure 3.10. Dots are centred at the edge inclination and ripple orientation and their radius corresponds to the height of the peak. [73]

These results provide important information about the controlled patterning of compliant surfaces using the scanning probe lithography technique. Considering the steady angle of ripple orientation on PS surfaces under the applied conditions (scan line distance, tip width and normal load) regular wavy patterns with a defined orientation can be formed, if the boundary orientation is close to steady angle. The resulting periodicity is well below $1\ \mu\text{m}$. For PMMA surface patterns with repetition distances in this range an antibacterial effect was demonstrated [101, 102]. Results on PS surfaces with micro patterns also indicate reduced adhesion when the period of the pattern is reduced. [103] In both cases the height of the structures was well above the here obtained values for the height of the surface ripples. The dimensions of the rippling structure covers a length scale reached with other fabrication methods used for polymeric nano electrical and optical devices [104, 105].

From the theoretical point of view the experimental results are supported by the model introduced by *Gnecco et al.* [18] and described in Chapter 3.1. The model was extended to three dimensions and used to simulate the scan induced surface structuring inside the same geometrical shapes as in AFM experiments. The resulting patterns show very similar orientations and the trend was identically. [73]

3.4. Particle release as a result of surface rippling

When a polymer surface is scanned or scratched with a sharp tip it is deformed viscoplastically and as demonstrated in experimental investigations and simulations [18, 79] indentations or grooves with a surrounding pile up are formed. Considering these observations the process causes plowing wear (see Chapter 2.4) induced by the friction during the sliding contact.

Scratching a compliant PS surface with a sharp AFM tip several times allows to observe damaging of surface by abrasive processes at the nm scale *in situ*. During the surfaces was scratched and damaged in contact mode in consecutive scan lines it was simultaneously imaged. Additionally damaged surfaces were imaged in tapping mode with a supersharp tip, which allows detailed images of damaged surfaces. Resulting contact mode images of scan areas while scraping first, third and fifth time are shown in Figure 3.12 a) to c). Corresponding tapping mode images acquired afterwards are shown in Figure 3.12 d) to f). In the first pass of scraping (Figure 3.12a) the typical rippling pattern is formed and can be observed also in tapping mode image (Figure 3.12d). At the left side a few ripples can be observed following the boundary orientation. Then the ripples start to reorientate to an angle of 55° in the steady region and a period about 200 nm which perfectly matches the results of *Mazo et al.* [79]. With increasing scan passes the rippling pattern becomes more and more damaged (Figure 3.12 b and c). After three scan passes (Figure 3.12b) first fine horizontal lines in the rippling pattern can be observed and become more pronounced in the fifth scan pass (Figure 3.12c). These lines indicate the movement of particles along the scan line by tip movement [106, 107]. Looking at the corresponding tapping mode images acquired afterwards (Figure 3.12e and f) spherical asperities with diameters up to 250 nm can be observed. Several spheres are detached and moved from their original position to the right side of the scan area which leads to the pile up observed at the right edge of Figure 3.12f. Similar images were obtained in another series of experiments on another sample shown in appendix A, Figure A.1.

Figure 3.13 shows cross sections extracted from tapping mode images shown in Figure 3.12d – f and marked by dashed lines. After one scan pass a regular wavy pattern with a corrugation of about 50 nm and a periodicity of about 250 nm is formed. After three scan passes the pattern becomes unregular. The corrugation is already in the range of 50 nm but periodicity disappeared. At the right side of the scan line a pile up starts to appear. After five scan repetitions only six peaks can be observed over the scan line, whereas the first and the last peak are caused by the pile up formed at the left and right edge of the scan area. Due to tip movement from left to right the pile up at the right boundary is created by particles pushed by the tip. With each scan pass particles are detached from their original location and pushed by the tip along the scan direction. This particle motion can reach distances of a few μm s up to the end of the scan line. In consequence particles are piled up at the right boundary indicated by the tall asperities at the right corner in Figure 3.12f and the tall peak in cross section after five scan passes shown in Figure 3.13. The pile up at the left boundary of scan area, which can be observed in the AFM images of the fifth scan pass (Figure 3.12c and f) and in the corresponding cross section (Figure 3.13), is caused by another effect. The scanning

process is started at the left side. In each scan line tip indents the surface at the left boundary of scan area and creates the initial indentation with a surrounding pile up. By pulling the tip laterally to the right the right part of the pile up is flattened while the corrugation of the left part is kept constant. This process is repeated in consecutive scan lines leading to a groove at left boundary of scan area. Since scanning is repeated at the same scan area up to five times the groove and the initial pile up at the left boundary is growing with each scan repetition leading to a deep groove and tall pile up after five scan repetitions. Considering the AFM tapping mode image after the fifth scan pass (Figure 3.12f) it can be assumed that the ripples in the middle of the scan area are flattened by the scan repetitions and the high peaks in cross section (red profile Figure 3.13) are caused by particles on the surface.

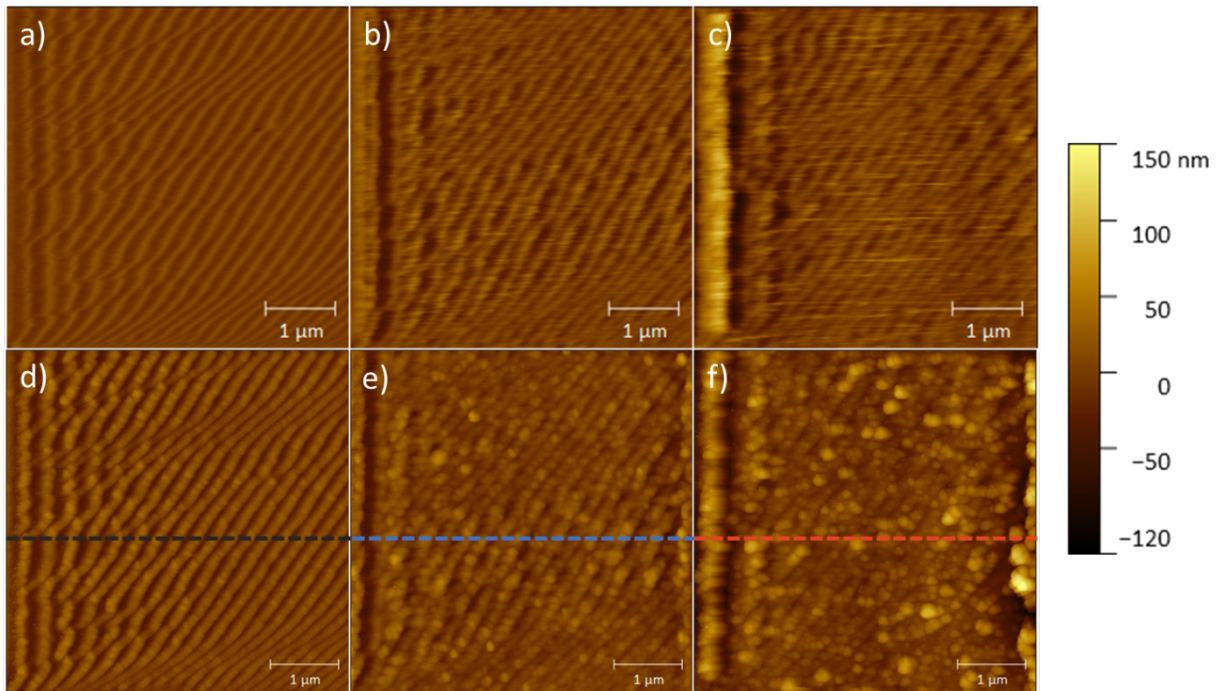


Figure 3.12: Topography images acquired while scanning an initially flat PS surface with $F_N = 100$ nN, $v = 15$ $\mu\text{m/s}$ and $b = 20$ nm a) once, b) three times and c) five times and corresponding tapping mode images afterwards d) – f). [74]

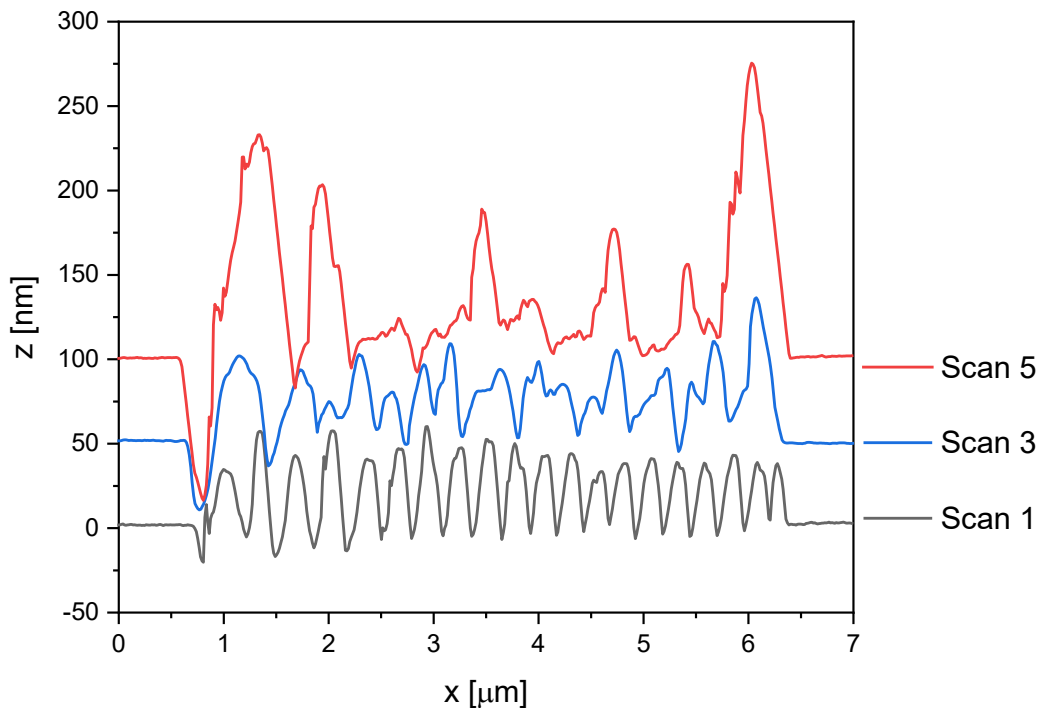


Figure 3.13: Cross sections extracted from Figure 3.12 d), e) and f) corresponding to dashed lines. [74]

The RMS surface roughness was measured in the steady regions in Figure 3.12d – f and during scrapping in contact mode. The results are shown in the diagram in Figure 3.14, open circles corresponds to contact mode data and filled circles corresponds to tapping mode data with the colour coding used in Figure 3.12 and Figure 3.13. In general the RMS values measured on contact mode images are lower than the ones measured on tapping mode images. This effect can be explained by the elastic and plastic deformation of the material. Due to high applied normal load during scrapping in contact mode surface is deformed plastically and instantaneously compressed elastically. Rippling pattern observed in the resulting topography image (see Figure 3.12a and cross section in Figure A.3 in appendix A) show a corrugation of 15 to 20 nm. Retracting the high normal load elastically compressing is removed resulting in a rippling pattern with a corrugation up to 50 nm (see Figure 3.12d and cross section in Figure A.3 in appendix A). The larger corrugation in tapping mode images leads to higher RMS values.

The RMS values measured in contact mode increases up to the third scan pass and stays more or less constant after reaching the maximum. RMS values measured in tapping mode are about 17 nm after one scan, 13 nm after three scan repetitions and 19 nm after five scan repetitions. In the first scan the regular rippling pattern on the initial flat PS surface is formed, which leads to large roughness values. By the following scan repetitions ripples are flattened, which causes a flattening and a decrease in roughness. As seen in Figure 3.12 the nucleation and detachment of particles starts in the third scan repetition. In consequence surface roughness increases again due to spherical asperities and detached particles all over the surface. These trends are confirmed by other series of scratch tests performed on other samples and with scan repetitions up to ten. The results are shown in Figure A.2 in appendix A and a similar evolution of RMS surface values can be observed.

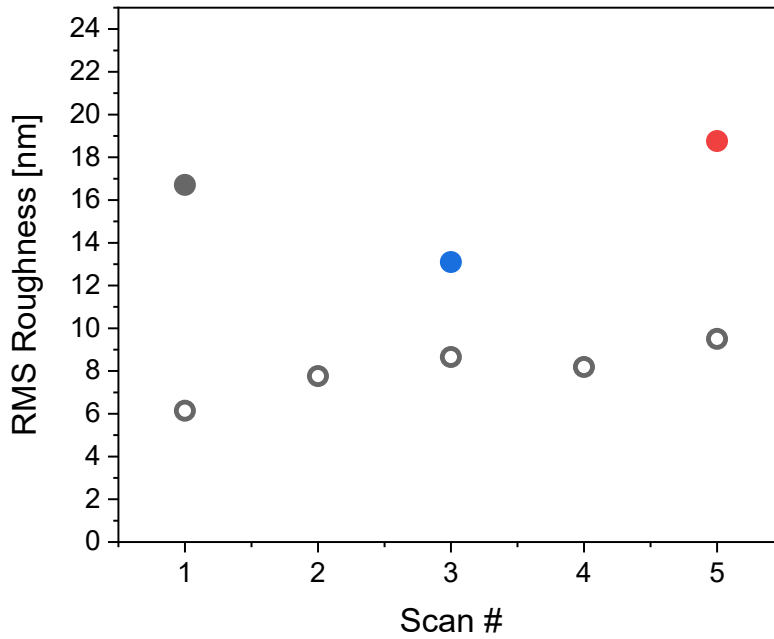


Figure 3.14: RMS roughness on $4 \times 4 \mu\text{m}^2$ areas in steady regions imaged while scraping the PS surface in contact mode (open circles) and in tapping mode afterwards (filled circles, same colour assignment as in Figure 3.13). [74]

The results obtained after the first scan (see Figure 3.12a and d) can be interpreted considering the theoretical model for ripple formation given in reference [18] and the theoretical background for ripple orientation given in reference [79]. The AFM tip indents the surface viscoplastically and extrudes the polymer material surrounding the tip as sketched in Figure 3.15a. As the tip is pulled laterally to the right more material is pushed up until the mechanical equilibrium of the system becomes unstable and the tip slips across the piled up material on its right. This process is repeated along parallel scan lines resulting in ripples orientated by an angle below 90° with respect to fast scan axis. Note that *Mazo et al.* assume constant volume under the surface profile during scratch process. [79] This is not the case in the results presented in this thesis. Cross sections after one scan repetition shown in Figure 3.13 and Figure A.3 in Appendix A clearly show that the apparent volume above the initial flat surface is larger than the volume extruded by the tip. The nominal radius of the used in tapping mode ($< 7 \text{ nm}$) is well below the radius of curvature of the valley (about 100 nm). It can be assumed that the tip can image the valleys up to the ground and in consequence the difference in volume cannot be explained by the convolution between tip and surface profile. [108] As discussed above the increased volume after retracting the normal stress exerted in contact mode can be partially explained by recovery of surface. Considering particle nucleation and detachment a second effect can be responsible for the increased volume. The ripple profile pushed by the tip undergo crazing [109, 110] schematically shown in Figure 3.15b. Inside the ripples polymer chains are stretched in the extruded regions and voids are formed leading to an increase of volume. Due to moving direction of the tip the ripples at the right side are loaded by a time-increasing shear stress additionally to the normal stress. In consequence crazing is expected to appear inside the ripples right to the tip. When the stress applied to the ripples exceed the tensile strength of polystyrene ($35 - 55 \text{ MPa}$ [94]) asperities are detached

from the crest forming nanospheres (shown in Figure 3.15c). The diameter of the spheres is limited by the curvature of the ripples in the order of 100 nm. The role of crazing mechanism in rippling process was already hypothesized by *Schmidt et al.* [111]. The supposed mechanism of particle nucleation and detachment results in a smooth process of particle with several stages which needs several scan repetitions. The radius of the final neck being cut is well below the curvature of the ripples. In consequence no visible variation in lateral force signal is expected.

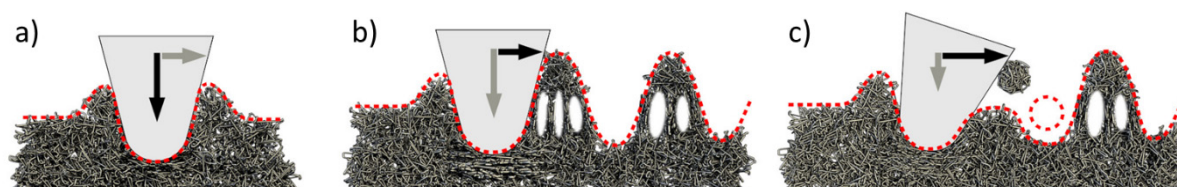


Figure 3.15: Three phases of proposed crazing mechanism for particle formation and detachment: a) Extrusion of material around the AFM tip indenting surface initially, b) crazing process and particle nucleation caused by increasing lateral force on a (previously formed) ripple pattern and c) sphere detachment. [74]

Once a nanosphere is detached it can be moved by AFM tip along the scan direction. This manipulation leads to typical horizontal lines in height image and can be observed in the images obtained during scrapping shown in Figure 3.12a – c. The AFM nanomanipulation of particles across a rippled surface was studied by *Gnecco et al.* [112]. They manipulated gold spheres on a ripples glass surface and observed that sphere tend to be trapped in the bottlenecks of the surface. A considerable static friction force must be overcome to detach them from these locations. In consequence the particle movement can be observed by peaks in lateral force signal. In the case of PS nanospheres manipulated on the rippled PS surface the motion can be recognized in the increased height in sections of several horizontal lines shown in Figure 3.16a. The corresponding cross sections of scan line in which the particle is moved and previous scan line (Figure 3.16b) clearly show the increase in height when the particle is moved and simultaneously imaged. When the particle remains in the new position height decreases to values similar to previous scan line. In contrast to the results presented in [112] lateral force does not give any evidence of particle motion (Figure 3.16c and d). This result indicates that the detachment and motion of PS particles occurs smoothly as expected from the crazing proposed for detachment process.

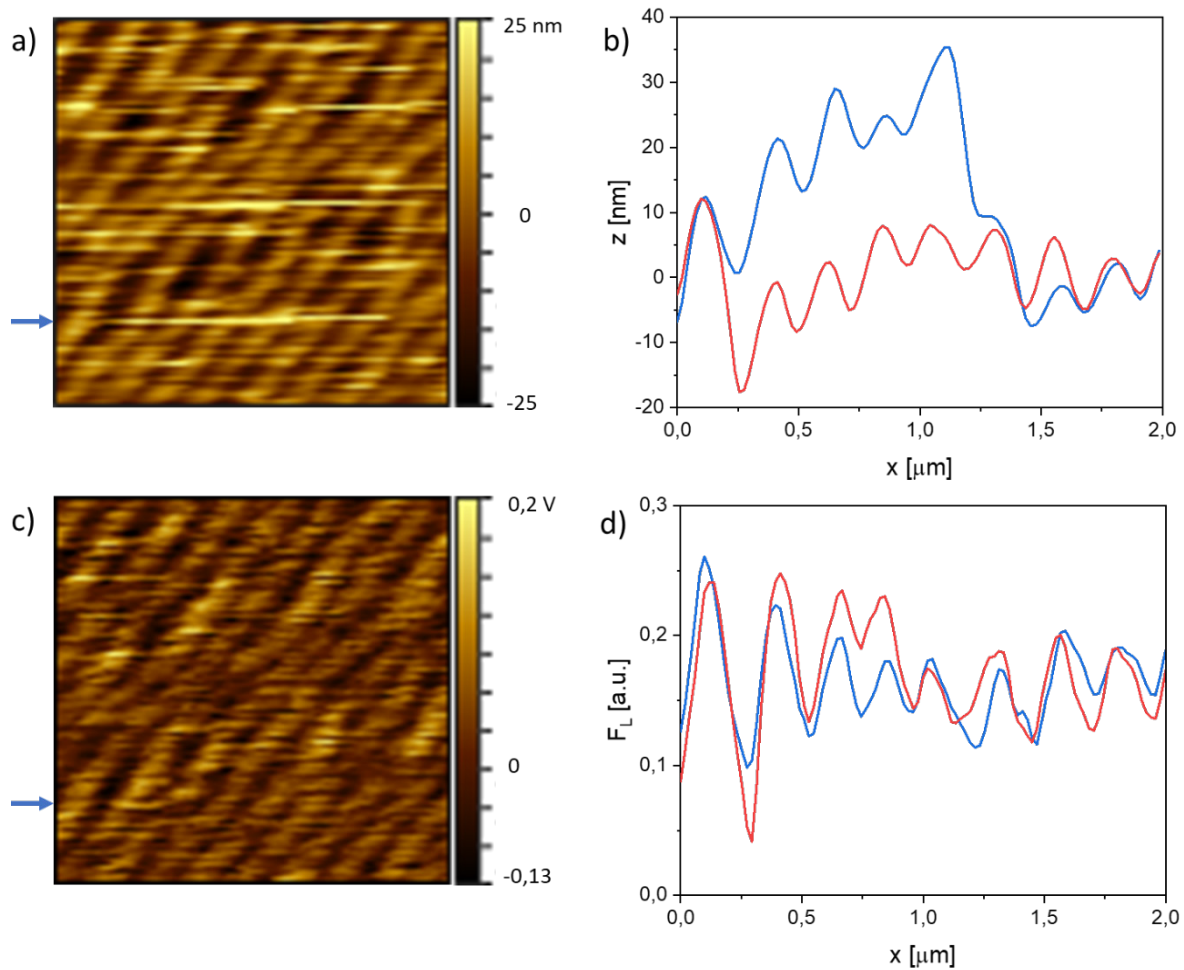


Figure 3.16: a) Topography image extracted from Figure 3.12c (size $2 \times 2 \mu\text{m}^2$), b) cross section of the scan line marked by blue arrow in a) (blue profile), and previous scan line (red profile) and c) corresponding lateral deflection signal with d) lateral deflection cross sections corresponding to b). [74]

These results demonstrate that polymer nanoparticles can be detached by sliding contacts exclusively. The release of particles is initiated within a few repetitions of sliding contact and generates large numbers of particles. Since the single particles can be moved easily along the surface they can also be released to environment which is impossible to prevent. This magnitude of degeneration and its consequence should be considered using scanning probe lithography for nano structuring of polymer surfaces. On the other hand these results provides fundamental information on the mechanism of stress induced degradation of polymers especially at the nanometer scale. The provided underlying process may can help to reduce unintended particle release to environment.

4. Periodic structures inside scratches on silica glass

As demonstrated in the previous chapters the formation of periodic surface structures induced by scanning or scraping processes is a well-known effect on compliant and ductile amorphous surfaces. Since it was already observed on brittle crystals it may can be also induced on brittle amorphous materials like glass surfaces. The following chapter will address this issue. After an overview of the state of the art in Chapter 4.1 the experimental setup is described in Chapter 4.2. The results are presented and discussed in Chapter 4.3. The here presented results are part of reference [113].

4.1. Background and motivation

Scratch tests on glass surfaces are routinely performed using nanoindenters in order to receive qualitative and empirical information on scratch regimes. Most of these studies address scratch regimes where significantly cracking or abrasion occurs. The main goals are the determination of an average load value for the onset of crack formation, study crack propagation and resulting stress fields inside the glass network. Especially for the determination of crack initiation a scratch test regime with continuous increasing normal load was established. [114-117] A scheme of the resulting scratch with the different regimes of surface deformation and a corresponding optical microscope image are shown in Figure 4.1 [115]. The scratch is divided into four regimes: plastic regime, radial cracking, median/lateral cracking and chipping and microabrasion. [115, 116]

The first stage is the plastic regime in which plastic-elastic deformation occurs during scratching. After scratching the elastic deformation is recovered and the plastic deformation remains. [13] Surface defects in the plastic regime can be generated by polishing and cleaning processes or sliding contacts during life cycle. It is well known that the applicable strength of glass devices is determined by critical defects or flaws that act as stress amplifiers and reduce it by several orders of magnitude. [118] For this reason in this stage surface deformation is at the origin of material strength and mechanical failure. Nevertheless it has been only recently addressed, from the perspective of grinding and polishing processes [14, 119] or scratching hardness [13, 120, 121]

The following two stages include different stages of crack formation. Whereas in these regions periodic patterns with a repetition distance in the range of μm s are typical and well known [122] such structures have never been observed in the plastic regime. *Li et al.* [123] observed a saw tooth shape in the curve of lateral force when scratching in a liquid environment which clearly indicates a stick-slip motion [70]. The resulting scratch pattern was not studied.

In the last stage of microabrasion a crushed scratch groove can be observed. The glass surface is destroyed and small glass particle are detached. [115, 116]

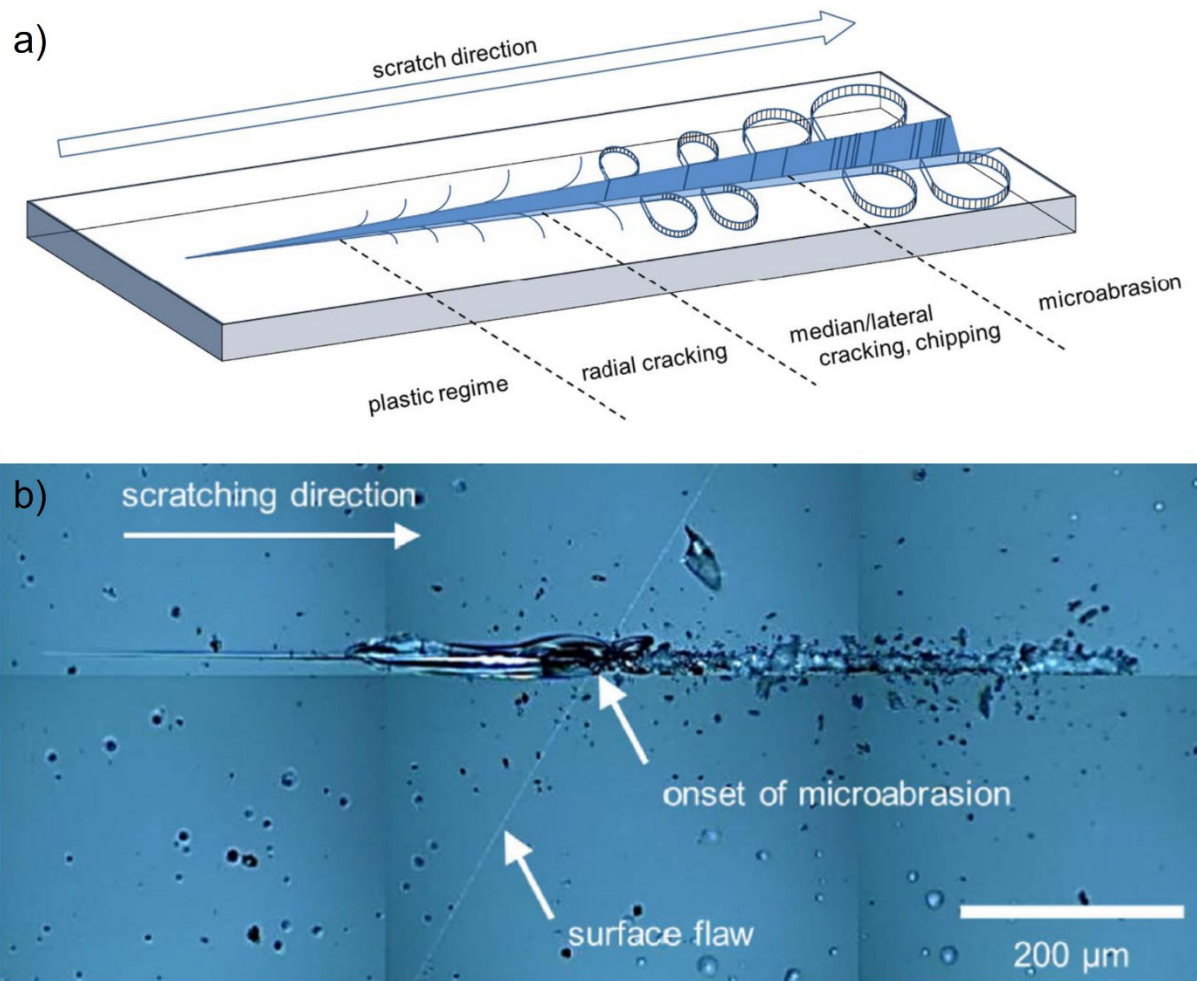


Figure 4.1: a) Scheme of a surface scratch on glass and b) a post mortem optical microscope image of a scratch generated with increasing load. [115]

Considering the known aspects about the periodic structures observed in regimes with crack formation and about the force evolution during scratching it can be hypnotized that also in plastic regime a stick-slip motion could occur leading to a periodic structure. The following part introduces a systematic investigation on the microstructure inside scratch grooves in plastic regime. A combination of nanoindentation and AFM technique is used to study the mechanical contact and early stage of wear on inorganic glass surfaces. AFM technique enables detailed and high resolution imaging of topography inside the scratches generated previously by a nanoindenter and thus the detection of nanostructures.

4.2. Methods

In this part a polished silica glass sample was scratched with a defined normal load and different velocities by a Berkovich tip. Normal load was chosen in the range of elastic-plastic deformation of the glass. After scratching the resulting wear scars were imaged using atomic force microscopy. The obtained structures inside the scratches were analyzed using data analysis in order to describe structures qualitatively and quantitatively.

4.2.1. Sample preparation

A commercial-grade vitreous silica (Heraeus Suprasil 1) was chosen for scratch tests. The glass sample was polished stepwise using dry silicon carbide powder with grain sizes of 70 μm , 40 μm and 9 μm . The final polishing step was performed with a suspension of diamond powder (grain size: 1 μm). Between polishing and scratching the sample was stored in vacuum. Directly before scratching the sample was rinsed with acetone and dried in flowing nitrogen.

4.2.2. Scratch tests

A scheme of scratch process is shown in Figure 4.2a. To generate surface scratches a load-controlled nanoindenter (G200, Agilent) was used. As indentation tool a diamond tip with a Berkovich shape was used (see Figure 4.2a). Scratch process started with a prescanning phase applying a normal load of 50 μN . After this prescan tip was halted and load was increased to the chosen setpoint between 10 and 30 mN. The normal load was chosen to avoid chipping or microabrasion. For these setpoints an elastic-plastic deformation is expected [13]. When the target setpoint was applied the scratching was started and performed until the desired scratch length was reached. At this point tip was halted again. Normal load brought back to prescan value followed by a short scanning. Penetration depth and lateral force were recorded during the whole process.

4.2.3. AFM imaging and analysis

The resulting wear scars were imaged using AFM (JPK NanoWizard4, Bruker). Scratches were scanned in both tapping and contact mode. In tapping mode fast scan direction was orientated vertical to scratch direction and silicon probes with a nominal tip radius of 7 nm (PPP-NCHAuD, Nanosensors) were used. In contact mode fast scan direction was orientated along scratch direction and silicon nitride probes with a nominal tip radius of 2 nm (Tip B, SNL-10, Bruker) were used. A scheme of AFM imaging in contact mode is shown in Figure 4.2b. The obtained images were analyzed using JPK proprietary software, Gwyddion and WSxM [124].

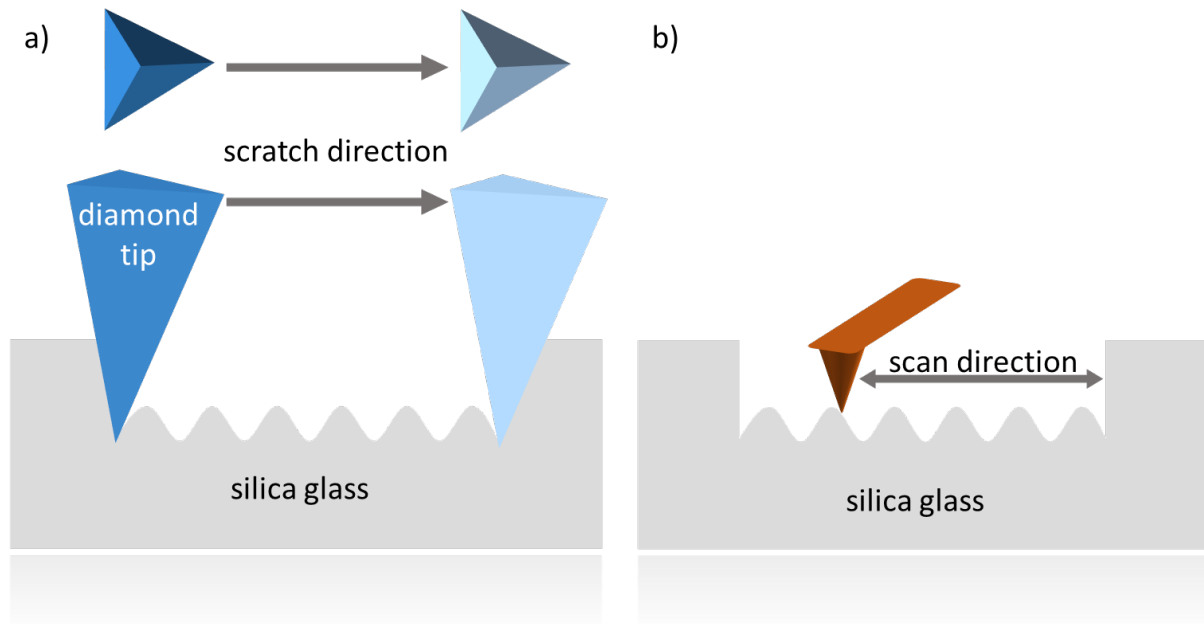


Figure 4.2: Experimental procedure for a) scratching silica glass with a Berkovich diamond tip of a nanoindenter and b) imaging the resulting scratch using atomic force microscopy.

4.3. Surface rippling induces by scraping with a sharp indenter

When the silica glass surface is scratched by the diamond tip a wear scar as shown in Figure 4.3a is generated. Figure 4.3 shows a topography image of the wear scar obtained by AFM scanning in tapping mode (Figure 4.3a), a detailed image of the starting region (Figure 4.3b) and the cross section extracted at the blue line (Figure 4.3c). The scratch was generated by moving the tip downwards with a normal load of $F_N = 30$ mN and a velocity of $v = 10$ $\mu\text{m/s}$. The resulting wear scar has a width of about 3,5 μm and a depth of about 250 nm. A pile up is formed on both sides of the scratch with unsymmetric shape. At the left side of the scratch the pile up reaches width and height of 300 nm and 20 nm. At the right side the width is approximately the same whereas the height is only about 10 nm. Width and depth of the wear scar increases with increasing normal load, which can be observed in AFM images in Figure B.3 and corresponding cross sections in Figure B.4 in appendix B. Both quantities do not change significantly with scratch velocity as shown by cross section in Figure B.6.

Additionally chips can be observed at the left side like known from wood or metals. Considering this fact and the pile up at both sides of the scratch groove it can be assumed that two subcategories of abrasive wear are combined: plowing and cutting wear. Inside the scratch a wavy pattern on the slope is visible. Due to the small corrugation in relation to scratch depth this pattern is less pronounced in the topography image. The cross section across the scratch groove shown on Figure 4.3c shows the profile of the scratch. Please note that x-axis is scaled in μm and z-axis in nm to highlight the details of the profile. A profile with z:x-ratio of one and corresponding indenter geometry is shown in Figure B.1 in appendix B. The profile is not perfectly V-shaped. The slope increases continuously from 7° with respect to horizontal plane near the surface to 14° at the ground. From the geometry of the Berkovich

indenter an orientation of 15° is expected. So only the orientation near the ground of the scratch groove is consistent with this value. In the central region an unsymmetric W-profile can be observed. Since this shape can be observed in all cross sections extracted from different scratches (see Figure B.4 and Figure B.6 in appendix B) it can be assumed that it is caused by the diamond tip itself.

As described in Chapter 4.2.2 a prescan was performed before the normal load for scratching was applied. The line of this prescan can be observed in the AFM topography image as a light line above the scratch with the same orientation as the scratch itself. It is more pronounced in a detailed image of this (Figure 4.3b). Considering this result it has to be assumed that even the small normal loads used in this prescan damage the glass surface.

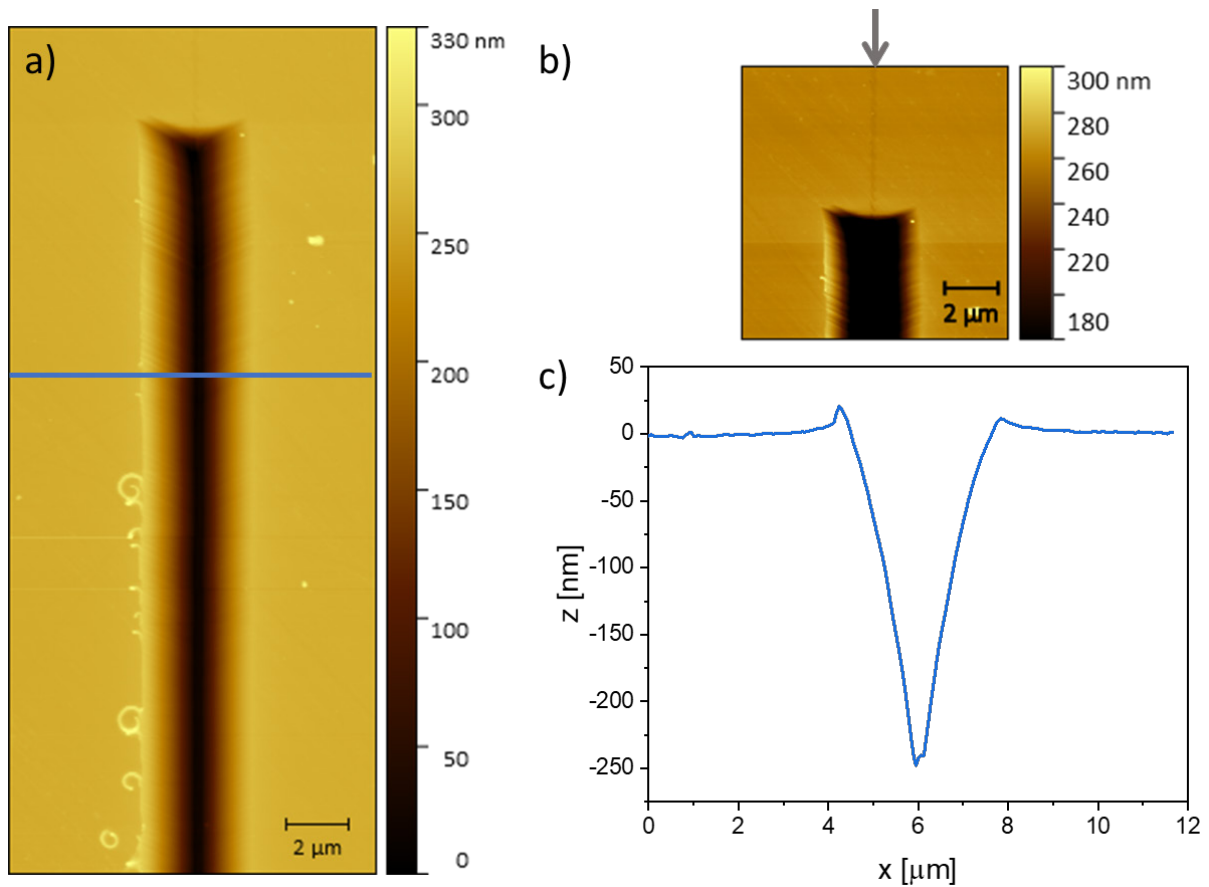


Figure 4.3: a) AFM topography of a silica glass surface previously scratched (downwards) with a normal force of $F_N = 30$ mN and a scratch velocity of $v = 10$ μm/s. b) Detailed image of starting point. The grey arrow is highlighting the prescan line and scratch direction. c) Cross section extracted along the blue line in a) stretched in z-direction. [113]

As already seen in the wear scar in Figure 4.3a a wavy pattern is formed inside the scratch and was found in all the scratches generated with the nanoindenter as described in Chapter 4.2.2 and all over the whole length of each scratch. Figure 4.4 shows 7 μm sections of scratches generated with scratch velocities of a) 10 μm/s, b) 50 μm/s, c) 100 μm/s, d) 150 μm/s, e) 300 μm/s and f) 500 μm/s. The normal load was kept constant at 30 mN. To pronounce the wavy pattern with a corrugation of only a few nm the AFM error signal was chosen. Since the

error signal is the difference between actual and setpoint force lateral dimension are correct but height information cannot be extracted from this images. The pattern can be also recognized in topography images shown in Figure B.5 in appendix B.

A regular herringbone pattern on the slopes of the scratches can be observed for all velocities. With increasing scratch velocity repetition distance (period) changes clearly. The orientation of the ripples is about 62° with respect to axis of travel, which is consistent with the triangular geometry of Berkovich indenter shown in Figure 4.2 and in detail in Figure B.2. On the unscratched surface some polishing lines are visible. Some of these polishing lines can be observed even in the scratch groove as an imprint.

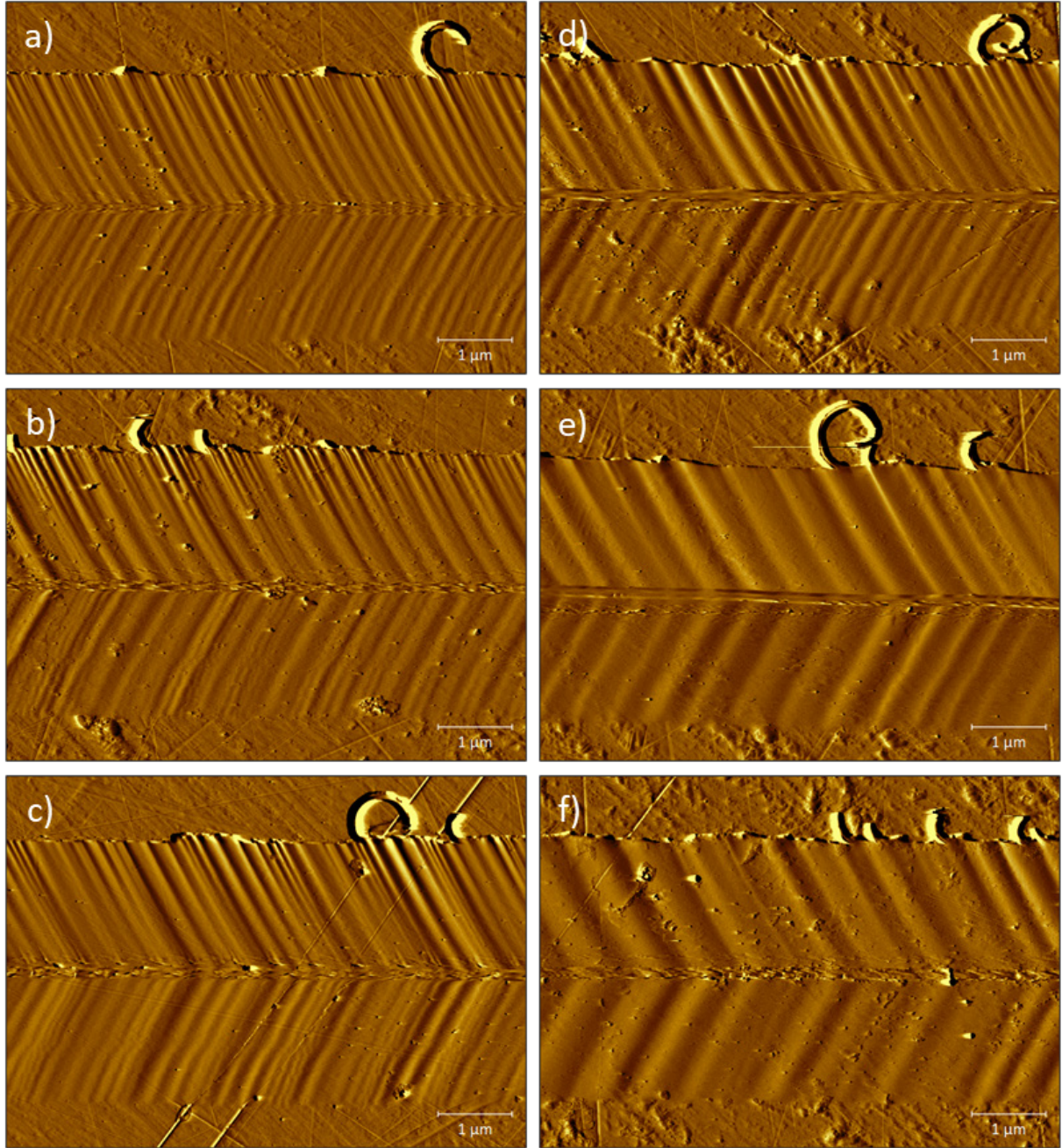


Figure 4.4: AFM error signals along wear scars scratched previously with a diamond tip from left to right applying a normal load of $F_N = 30 \text{ mN}$ and scratch velocities of a) $v = 10 \mu\text{m/s}$, b) $v = 50 \mu\text{m/s}$, c) $v = 100 \mu\text{m/s}$, d) $v = 150 \mu\text{m/s}$, e) $v = 300 \mu\text{m/s}$ and f) $v = 500 \mu\text{m/s}$. [113]

To quantify the periodicity ripple repetition distance or period λ was measured in two different scratches per velocity over a length of min. 30 μm per scratch. Figure 4.5 shows the procedure for a section of a scratch generated with a velocity of 10 $\mu\text{m/s}$ exemplarily. Again the error signal was used due to the clear contrast of the ripples on the slope of the scratch groove (Figure 4.5a). The average value of λ can be estimated from 2D self-correlation as shown in Figure 4.5b and d or from 1D fast Fourier transform (FFT) along horizontal lines as shown in Figure 4.5c and e. In the case of Figure 4.5a an average ripple period λ of $220 \pm 6 \text{ nm}$ was calculated. The results of FFT confirmed the values obtained by self-correlation and prove that the period is constant along vertical direction. The central region was excluded to avoid an influence of impurities observed in this region. As demonstrated in Figure B.5 the wavy pattern can be observed also in topography imaged and their period is consistent with the values obtained from the error signals.

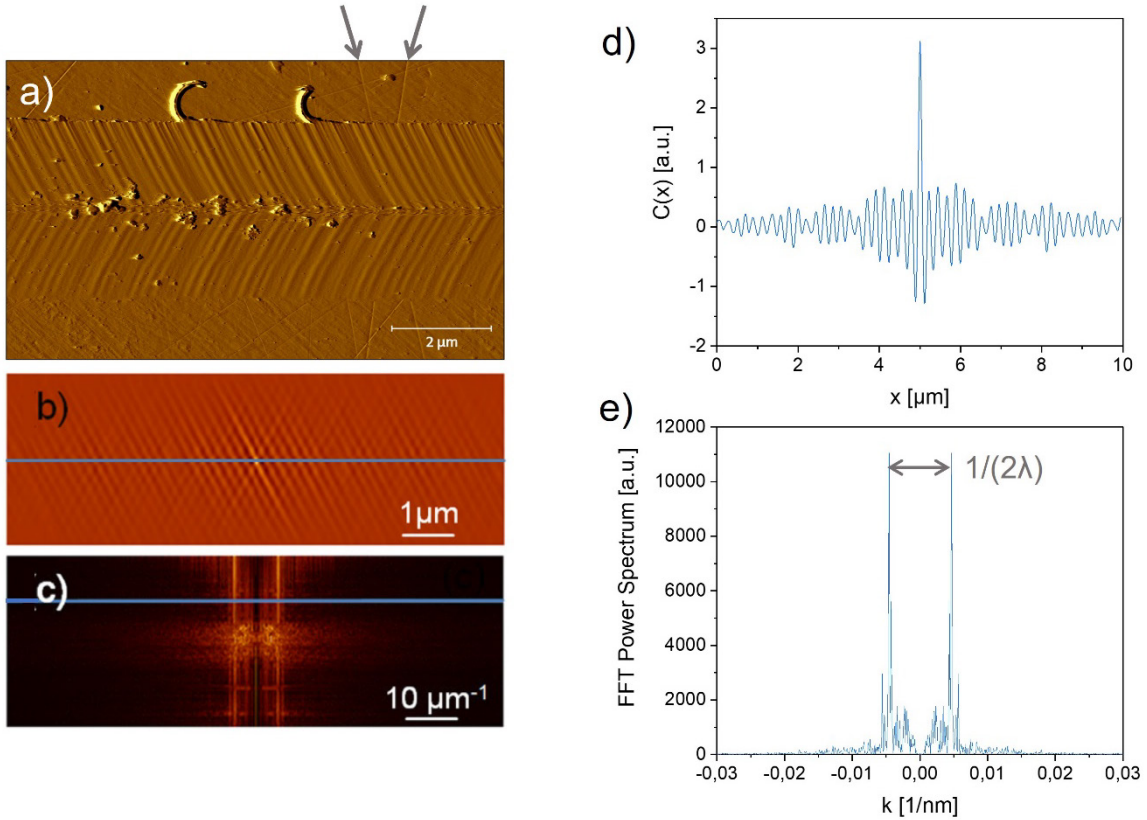


Figure 4.5: a) AFM error signal ($10 \times 6 \mu\text{m}^2$) across the wear scar in Figure 4.3a) and Figure 4.4a). Scratch direction from left to right. The grey arrows highlight two polishing lines. b) 2D self-correlation and c) 1D-FFT along longitudinal direction extracted from the region corresponding to the herringbone pattern in a); d), e) cross sections along the blue lines in b) and c), respectively. [113]

The average ripple period corresponding to every velocity was determined from the single values obtained for the different AFM images of scratches generated with the same velocity. The resulting values are plotted in a diagram shown in Figure 4.6. Additionally standard deviation was calculated and plotted as error bars. The standard deviation at the slowest velocity of 10 $\mu\text{m/s}$ was very low so that the resulting error bar is covered by the dot in the diagram. Ripple period λ depends on scratch velocity and increases with increasing scratch

velocity in general. To quantify the correlation between ripple period and scratch velocity a linear fit was applied to the datapoints, which can be described by Equation 4.1. From linear regression the offset and the slope of the graph can be estimated and the corresponding function can be calculated as

$$\lambda = \lambda_0 + t_0 v$$

Equation 4.1

with $\lambda_0 = (207 \pm 8)$ nm and $t_0 = (1,07 \pm 0,15)$ ms.

Whereas the linear regression crosses the values or respectively the error bars of five velocities the value of 50 $\mu\text{m/s}$ is not covered. This could be caused by a statistical error or the periodicity does not follow the linear trend as assumed at these small velocities.

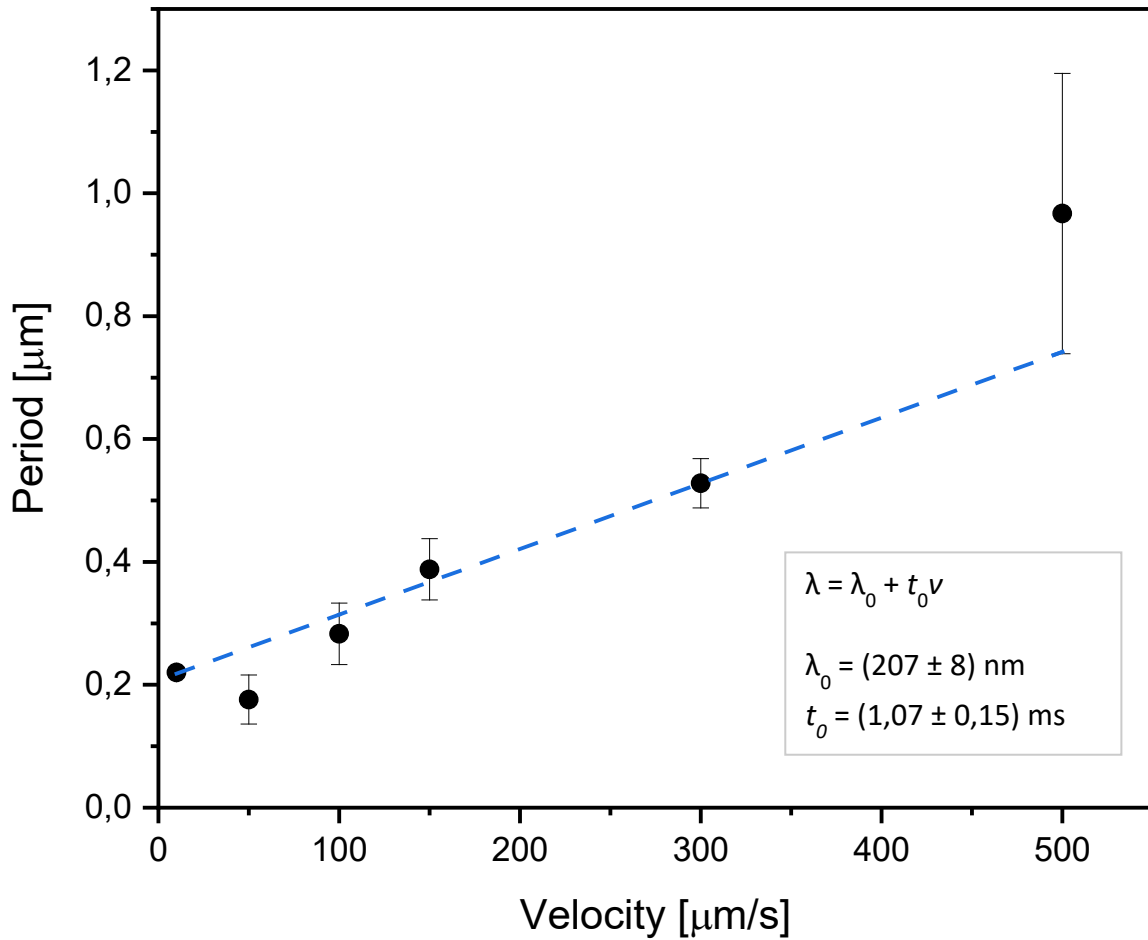


Figure 4.6: Velocity dependence of the ripple period as measured by AFM *ex situ* after scratching with a normal load $F_N = 30\text{mN}$ (black dots) and linear fit of the experimental data points (blue curve) to evaluate the correlation. [113]

The time dependent indentation depth and the lateral force F_L recorded *in situ* during scratching provide additional information. Corresponding graphs obtained while scratching with $v = 10 \mu\text{m/s}$ are shown in Figure 4.7. As shown in Figure 4.7a the average indentation depth while scratching was about 460 nm, which is well above the scratch depth measured by AFM of about 250 nm (see Figure 4.3c and Figure B.6 in appendix A). Considering the shape of the cross section it can be assumed that the glass significantly recovered during unloading. This effect was already observed in previous indentation tests on silica glass with a Vickers indenter [125] and it is not known from other common glasses like soda-lime silicates [126, 127].

From the average value of lateral force during scratching of $F_L = (4,40 \pm 0,05) \text{ mN}$ (extracted from Figure 4.7b) a coefficient of friction of $\mu \approx 0,15$ can be estimated. This value changes only slightly with increasing scratch velocity. A regular variation corresponding to the ripple period cannot be observed in both, indentation depth and lateral force, with the resolution of 100 nm in the available setup.

When the normal load is applied the indentation depth increases asymptotically (see Figure 4.7a). In consequence the indentation rate dz/dt changes from 175 nm/s at the beginning of the indentation (grey arrow) to 50 nm/s at the end of the transition from indentation to scratching (blue arrow) within a time of 4,3 s. In this time lateral movement of the indenter is stopped. When scanning is resumed (marked with the green arrow) the penetration rate increases to 250 nm/s for a short time of 0,2 s. This means that the pressure exerted by the indenter is not balanced by the modified surface profile. The glass network is still reordering under the applies pressure when lateral movement of the indenter is restarted and the scratching process begins. Additionally the lateral force is found to increase continuously at the beginning of the scratch process as shown by the curve in Figure 4.7b. The saturation value of $F_L = 4,40 \text{ mN}$ is reached within 0,2 s. From the slope of the initial part of the lateral force curve an effective lateral stiffness of $k = 2,8 \text{ kN/m}$ can be estimated.

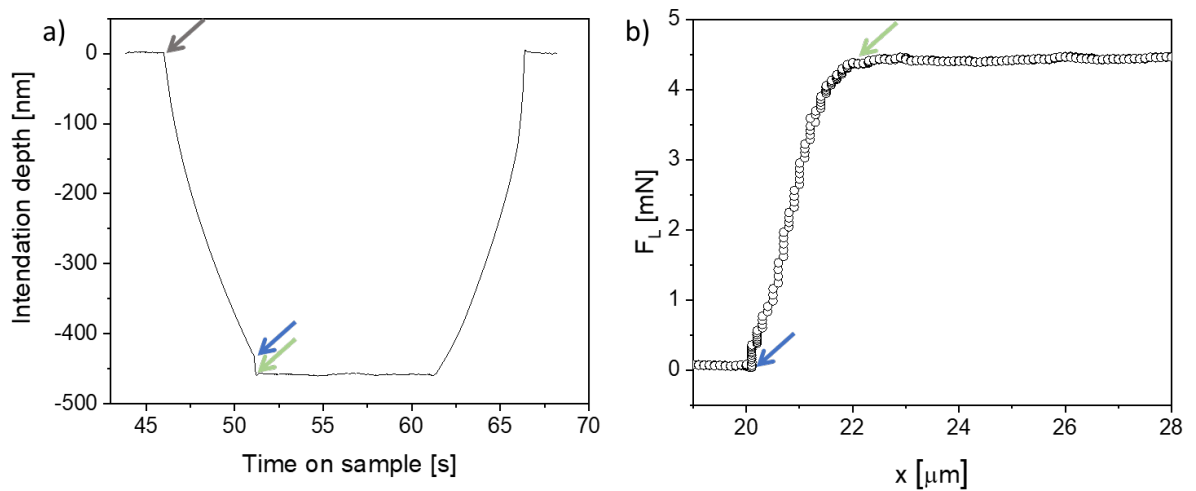


Figure 4.7: a) Time dependent indentation depth while scratching with $v = 10 \mu\text{m/s}$. Scanning was stopped at $t = 46 \text{ s}$, when the normal load of 30 mN was applied and resumed at $t = 51 \text{ s}$. Slightly after this point a steady state was reached. At $t = 62 \text{ s}$ the normal load was retracted. b) Lateral force F_L vs. indenter position x when the scratching process initiates (at $x = 20 \mu\text{m}$). The blue and green arrows correspond to times in a). [113]

Combining the results obtained by nanoindenter and AFM measurements the time spent by the Berkovich tip in each dip of the herringbone pattern can be estimated as $\lambda/v = 22,0$ ms. During this stick time the indenter penetrates the surface by an additional depth $\Delta z = (dz/dt)(\lambda/v) = 5,5$ nm. This value is larger than the ripple corrugation observed in AFM measurements which indicates the elastic recovery. Together with the reduced scratch depth and the shape of the wear scar differing from the expected perfect V-shape observed after scratching a significant elastic recovery of the glass is proven.

Whereas the model for the formation of surface ripples on polymer surfaces is based on the Prandtl-Tomlinson model the interpretation of the surface rippling inside a glass scratch is based on the model for stick-slip motion assuming a block sliding on a flat surface, explained in Chapter 2.5 [65]. It can be assumed that the tip apex sticks to an indentation side while the tip is pulled laterally along the x-direction. In consequence the lateral force F_L increases till it reaches a point at which the glass cannot resist this force anymore. Then the tip suddenly slips into the next position. In contrast to the model of the sliding block [65] the indenter is not sliding on the surface but indenting the glass. At increasing velocities the tip is expected to indent the surface less deeply, which leads to reduced lateral forces required to induce the slip. In this case lower values of ripple period λ would be expected with increasing scratch velocity. This was observed for polymer surfaces scraped by AFM [18], but it is in contrast to the results presented in Figure 4.6. This difference can be explained by the differences in the experimental setups. In the case of scratching a glass surface with the nanoindenter the tip is retracted only a few nm during slip phase. The main part of the indenter is still indenting the surface during slip phase. In consequence even in the stick phase the indenter applies a force to the glass. Caused by this fact in combination with the brittle behaviour of the glass chemical bonds have to be broken when the indenter slips into the next position. In the case of the polymers scratched by AFM tips as shown in Chapter 3 and a series of previous works [12, 18, 48] tip is retracted (nearly) completely and not indenting the surface during the slip phase. The compliant character of the material allows a plastically deformation without breaking chemical bonds.

The experimental results provide the validation for a theoretical model developed by *Gnecco et al.* [113]. Like the phenomenological interpretation it is based on the equations known from the model for stick-slip motion of a sliding block [64] and confirms the linear increase of ripple period λ with velocity v . The model was developed in Supplemental Material of reference [113] as described following. It was assumed that the indenter acts like a object with the mass m pulled by a spring with the stiffness k along a surface as described in Chapter 2.5. Sliding starts at the time t_1 when the spring force overcomes the threshold value F_S corresponding to the static friction force

$$t_1 = \frac{F_S}{kv}$$

Equation 4.2

and is damped by a constant kinetic friction force F_K . The tip respond as a harmonic oscillator and the motion of the tip along the surface can be described by the following equation

$$x(t) = vt - \frac{F_K}{k} - a \sin(\omega_0 t - \varphi)$$

Equation 4.3

with $\omega_0 = \sqrt{k/m}$ as the resonance frequency of the spring – tip system. The amplitude a of the oscillator and the phase shift ϕ are given by

$$a = \sqrt{\left(\frac{v^2}{\omega_0^2} + \frac{(F_S - F_K)^2}{k^2}\right)}$$

Equation 4.4

and

$$\varphi = \arctan\left(\frac{\omega_0(F_S - F_K)}{kv}\right) - \frac{\omega_0 F_S}{kv}$$

Equation 4.5

obtained from the initial conditions $x(t_1) = 0$ and $\dot{x}(t_1) = 0$. The tip will stop at the time t_2 at which $\dot{x} = 0$ again:

$$t_2 = t_1 + \frac{2}{\omega_0} \arctan\left(\frac{\omega_0(F_S - F_K)}{kv}\right).$$

Equation 4.6

The slip time t_{slip} is given by the difference $t_2 - t_1$. At t_2 the process starts again and following a similar approach from now on the stick time will be given by the formular

$$t_{stick} = \frac{2(F_S - F_K)}{kv}.$$

Equation 4.7

Under these assumptions the times of the two phases can be calculated

$$t_{slip} = \frac{2}{\omega_0} \arctan\left(\frac{v_c}{v}\right) \quad \text{and} \quad t_{stick} = \frac{2v}{\omega_0 v}$$

Equation 4.8

where $\omega_0 = \sqrt{k/m}$ is the resonance frequency of the system and $v_c = \omega_0(F_S - F_K)/k$. For $v \ll v_c$ slip time is $t_{slip} \approx \frac{\pi}{\omega_0}$ and the repetition distance of the stick-slip motion is given by $\lambda = v(t_{stick} - t_{slip}) = \lambda_0 + t_0 v$, where

$$\lambda_0 = \frac{2(F_S - F_K)}{k} \quad \text{and} \quad t_0 = \frac{\pi}{\omega_0}$$

Equation 4.9

The resulting linear response perfectly matches the linear regression of the experimental results shown in Figure 4.6. Considering these results it can be assumed that the ripple period increase linearly with scratch velocity. Under steady conditions λ represents the ripple period. In combination with the experimental data λ_0 and t_0 and some additional parameters like the effective mass of the indenter and $\Delta F = F_S - F_K$ can be estimated. Since surface rippling inside glass scratches has been observed and described for the first time the combination of the experimental results and the theoretical explanation given by *Gnecco et al.* provides comprehensive basic information about the phenomenon. [113]

5. Conclusion and outlook

In this chapter the thesis is concluded and an outlook on following investigations is given. In this context some open questions are listed. Scan induced surface rippling on polymer surfaces was investigated in relation to controlling the orientation and wear in this thesis. Additionally the practicability to other materials was tested and the resulting structures were analyzed.

In the first part of the thesis the AFM was used as a nanolithography technique to induce specific surface patterns. A polymer surface was scanned and structured thereby by an AFM tip under conditions tested previously. By the specific variation of the boundary orientation the direction of the resulting rippling structure was influenced. The resulting surface patterns were images using the same AFM tip. It was shown that the ripple orientation was clearly affected by the boundary orientation. Changes in the boundary angles caused changes in ripple orientation in the boundary regions of scanned areas. The ability to keep this orientation over larger distances depended on the orientation of boundary referred to fast scan axis. It was demonstrated that the orientation of the ripples can be adjusted over distances of several μm when the boundary angle is in a certain range, in particular the range of the steady state orientation of the ripples. The angle of this steady state orientation can be determined for each combination of parameters by scanning a squared area. Further investigations may focus on the control of ripple orientation over larger distances or the change of the orientation inside an area by a change of experimental parameters (normal load, scan velocity etc.). A further interesting issue is the formation of scan-induced ripples on polymer blends.

In the second part the influence of the scanning process on wear of the polymer surface was investigated. After the initial ripple pattern formation the area was scanned repeatedly till the pattern was destroyed. AFM technique enabled the manipulation and observation of the surface simultaneously. During the scan repetitions hints on particle detachment were observed in the topography images but not clearly proven in the lateral deflection signal. A imaging step afterwards clearly showed the presence of spherical particles detached in the scan passes and pilling up at the boundary of the scan area. The absence of peaks in the lateral deflection signal indicates a smooth detachment caused by a crazing mechanism inside the polymer. The crazing mechanism theory is also supported by an increased volume of the film after surface rippling. To prove this assumption further investigations are necessary. Since imaging of the crazing under the surface is a challenging issue may investigations on the density or mechanical properties of the ripples surface can help to support this theory. The existing theoretical model explaining the ripple formation on initially flat surfaces cannot explain the surface evolution when the scan process is repeated. So in the future it has to be improved considering scan repetitions and detachment and movement of particles. Further investigations should also address the release of the detached particles to environment.

After investigations of surface rippling phenomenon on compliant surfaces the formation of scan, respectively, scratch-induced periodic structures on a hard and brittle material was

investigated in the third part of the thesis. A commercial silica glass was scratched by a diamond tip of a nanoindenter. The normal load was chosen to induce plastic-elastic deformation and the scratch velocity was varied. The resulting surface scratches were imaged with AFM. Inside the scratch grooves a periodic herringbone pattern was found with a periodicity variation with increasing scratch velocity. The quantification of the periodicity has clearly proven an increasing repetition distance with increasing velocity and indicates a linear trend. The results validate a theoretical model based on a model for stick-slip motion at the macroscopic scale and considering the experimental parameters. The theoretical model supports a linear increase of ripple period with scratch velocity. Since the experimental results especially for low velocities does not perfectly match the linear trend additional experiments with low velocities can help to prove the linear regression. The assumed stick-slip motion of the indenter may could be tested with scratch tests performed with a AFM which allows the recording of lateral force variations. To obtain more information about the physical process the influence of other parameters like normal load or indenter geometry on ripple periods has to be tested. Additional information can be obtained by testing the formation of a herringbone pattern inside microscratches on other glass systems. Furthermore the formation of chips during microscopic scratching seems to be typical for silica glass. Considering the brittle behavior of silica glass this aspect is surprising and has to be investigated in detail in the future.

A. Appendix surface rippling on polymers

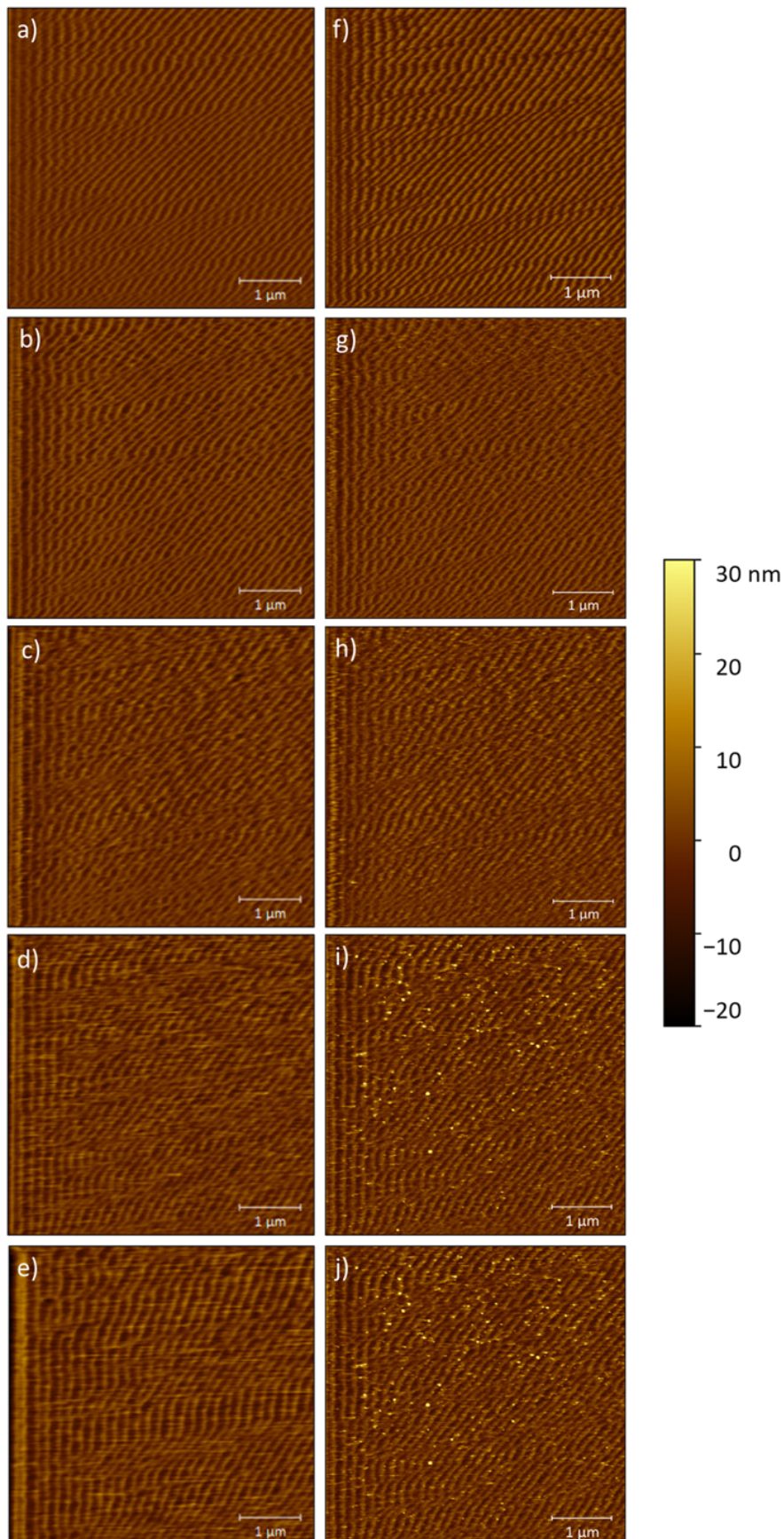


Figure A.1: Topography images acquired while scanning an initially flat PS surface with $F_N = 100$ nN, $v = 11,3$ $\mu\text{m/s}$ and $b = 20$ nm a) once, b) two times, c) three times, d) five times and e) ten times and corresponding tapping mode images afterwards f) – j).

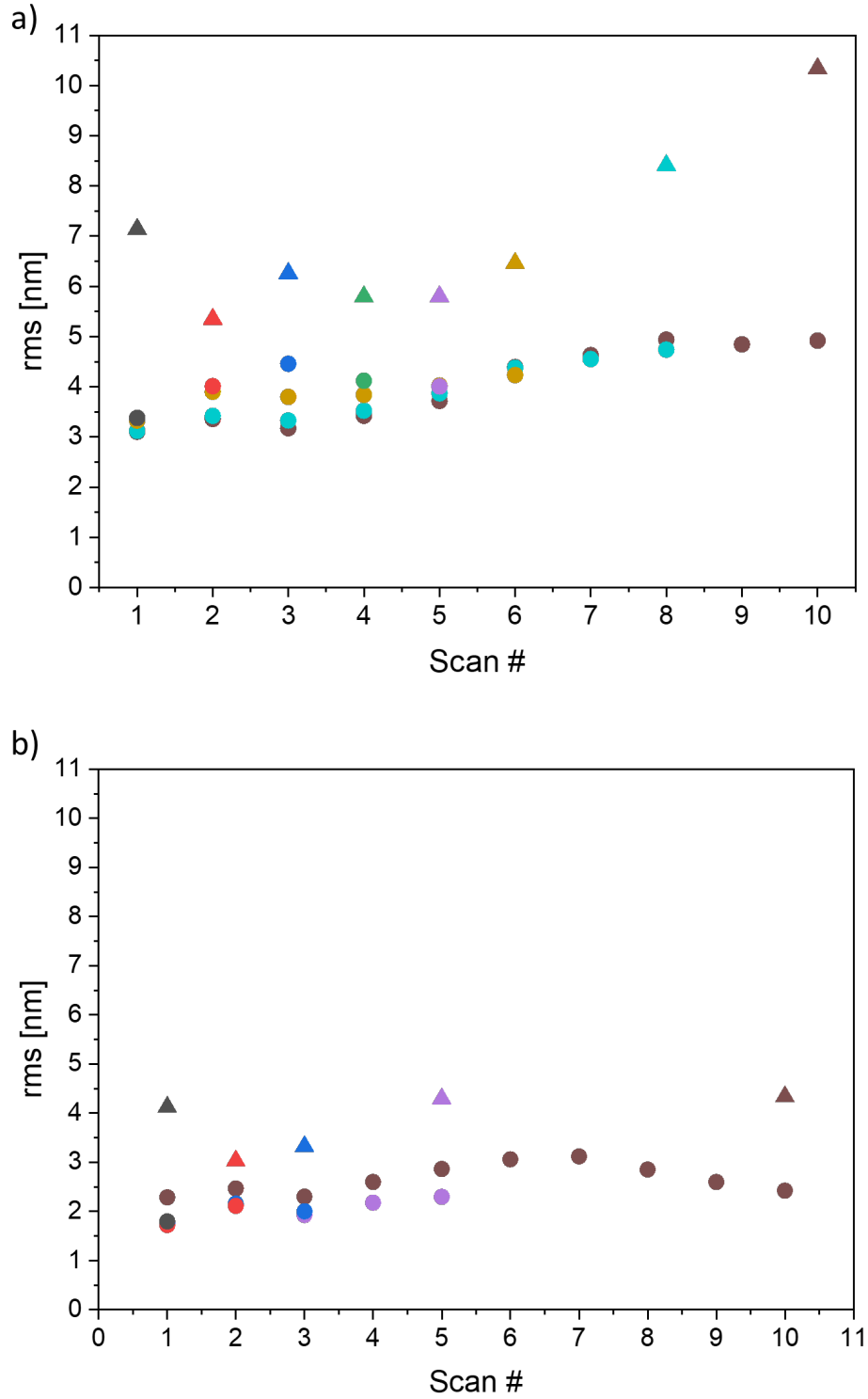


Figure A.2: Surface roughness rms of structured areas depending on scan repetitions. Dots represent values acquired while scrapping in contact mode, triangles represent values acquired while imaging in tapping mode afterwards. Colours represent measurements at same scan areas. Scanning conditions while scrapping a) $F_N = 100$ nN, $v = 15$ $\mu\text{m/s}$ and $b = 20$ nm (corresponding to results shown in Figure 3.12) and b) $F_N = 100$ nN, $v = 11,3$ $\mu\text{m/s}$ and $b = 20$ nm (corresponding to results shown Figure A.1).

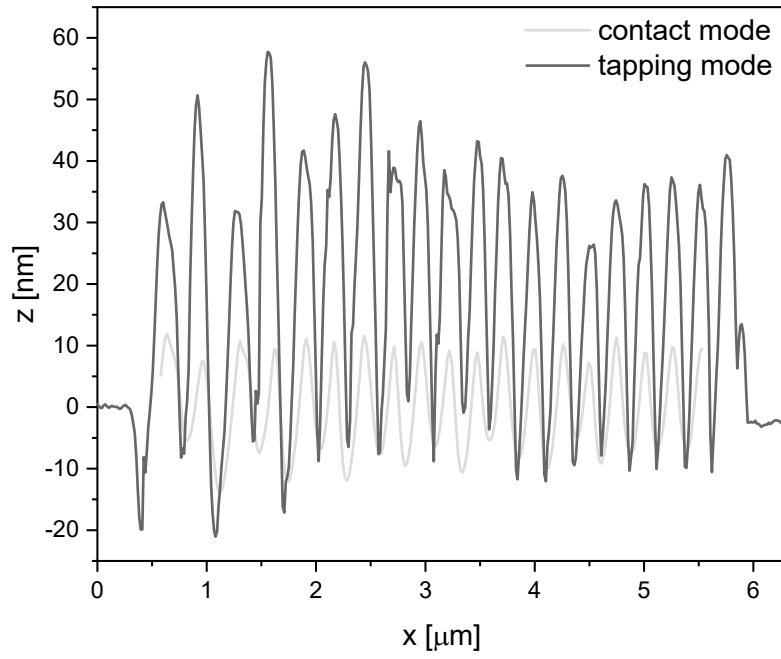


Figure A.3: Cross sections extracted from Figure 3.12 a) and d) at the same horizontal line.

B. Appendix surface rippling on glass

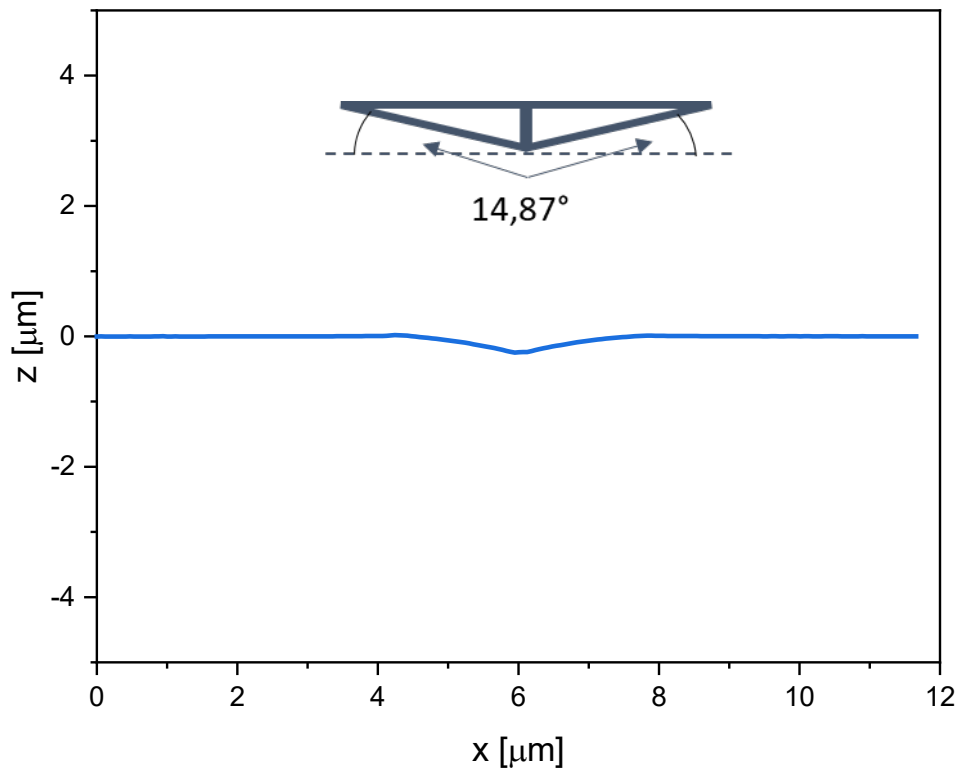


Figure B.1: Cross section extracted from Figure 4.3a with $z:x$ – ratio of one including a scheme of the indenter geometry.

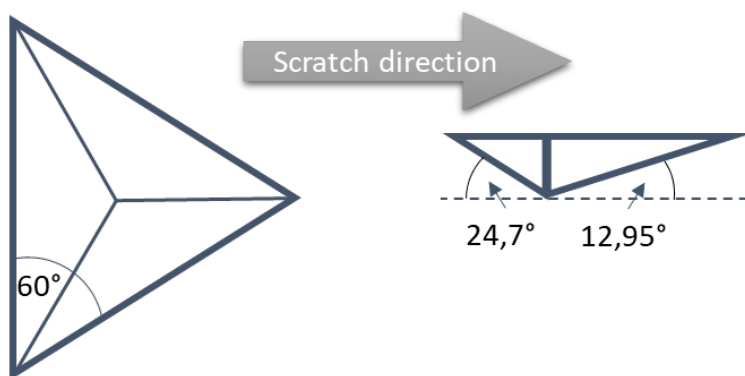


Figure B.2: Geometry of Berkovich indenter[128].

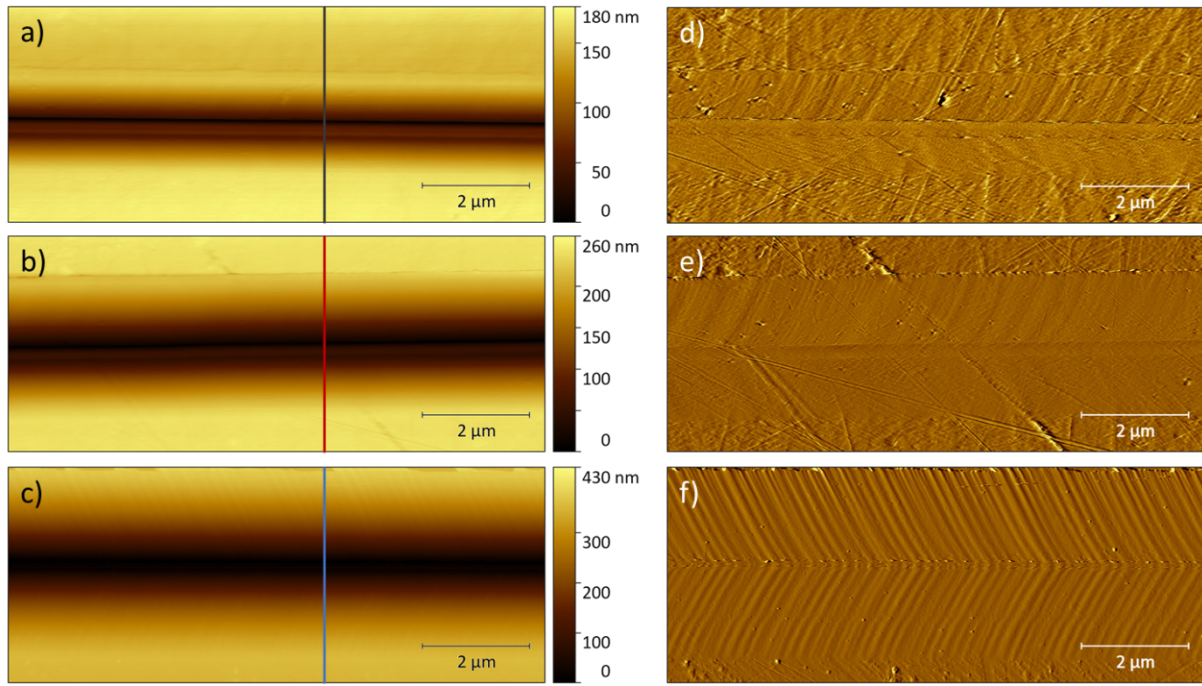


Figure B.3: a) – c) AFM topography images of scratches on silica glass scratched with a velocity of $v = 10 \mu\text{m/s}$ and normal loads of a) $F_N = 10$ mN, b) $F_N = 20$ mN and c) $F_N = 30$ mN and d) – f) corresponding error signals.

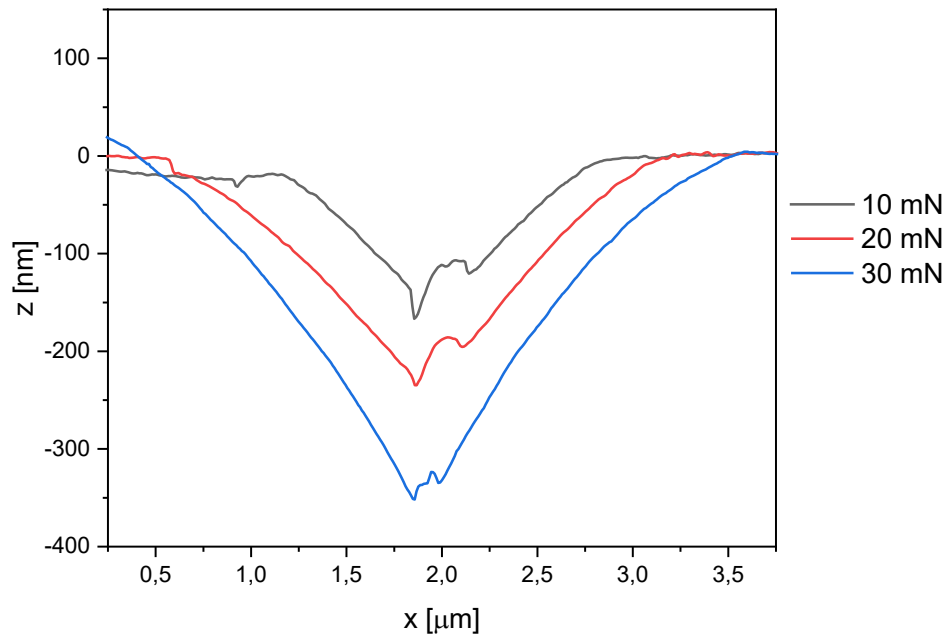


Figure B.4: Cross section extracted from topography images in Figure B.3a) – c) at the dark grey, red and blue lines.

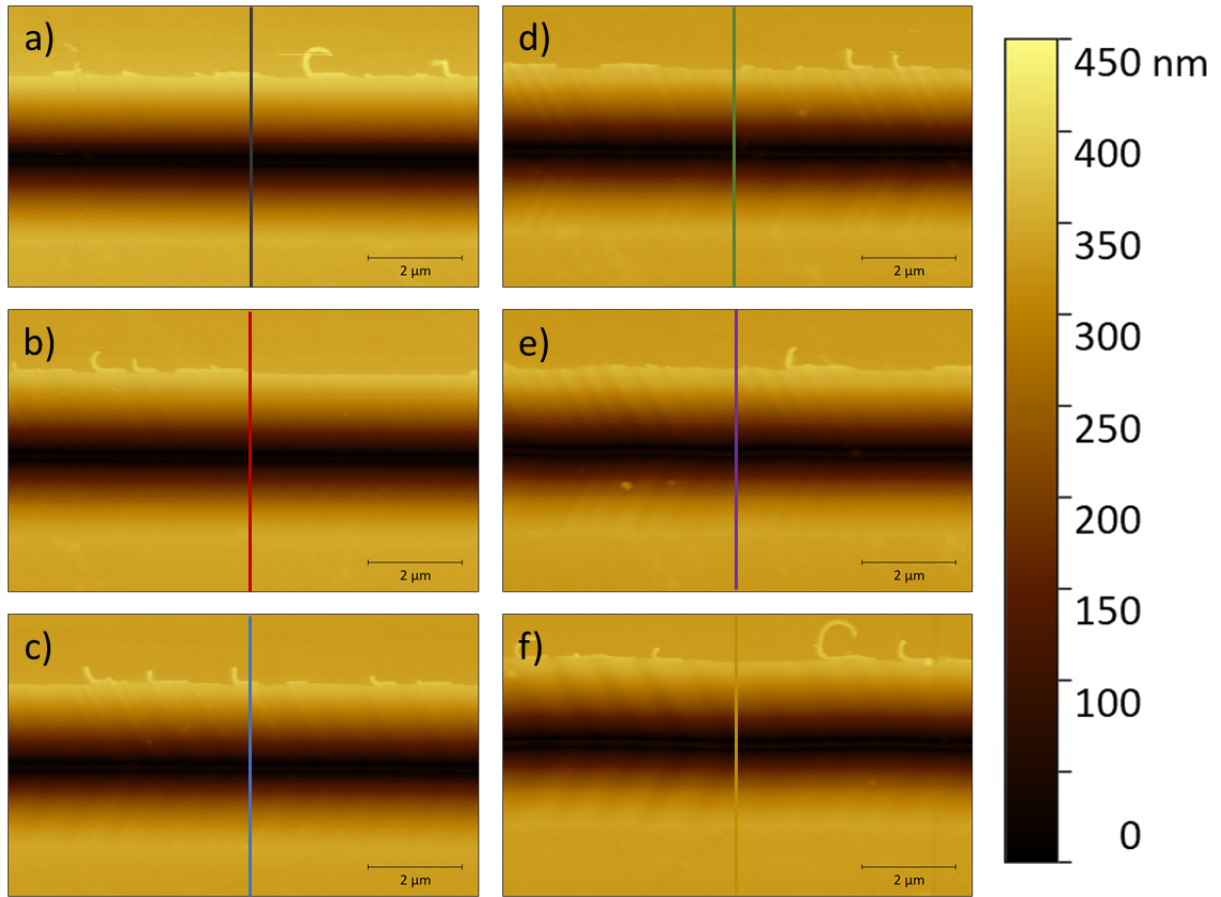


Figure B.5: AFM topography images of scratches on silica glass scratched with a normal load of $F_N = 30$ mN and velocities of a) $v = 10$ $\mu\text{m/s}$, b) $v = 50$ $\mu\text{m/s}$, c) $v = 100$ $\mu\text{m/s}$, d) $v = 150$ $\mu\text{m/s}$, e) $v = 300$ $\mu\text{m/s}$ and f) $v = 500$ $\mu\text{m/s}$.

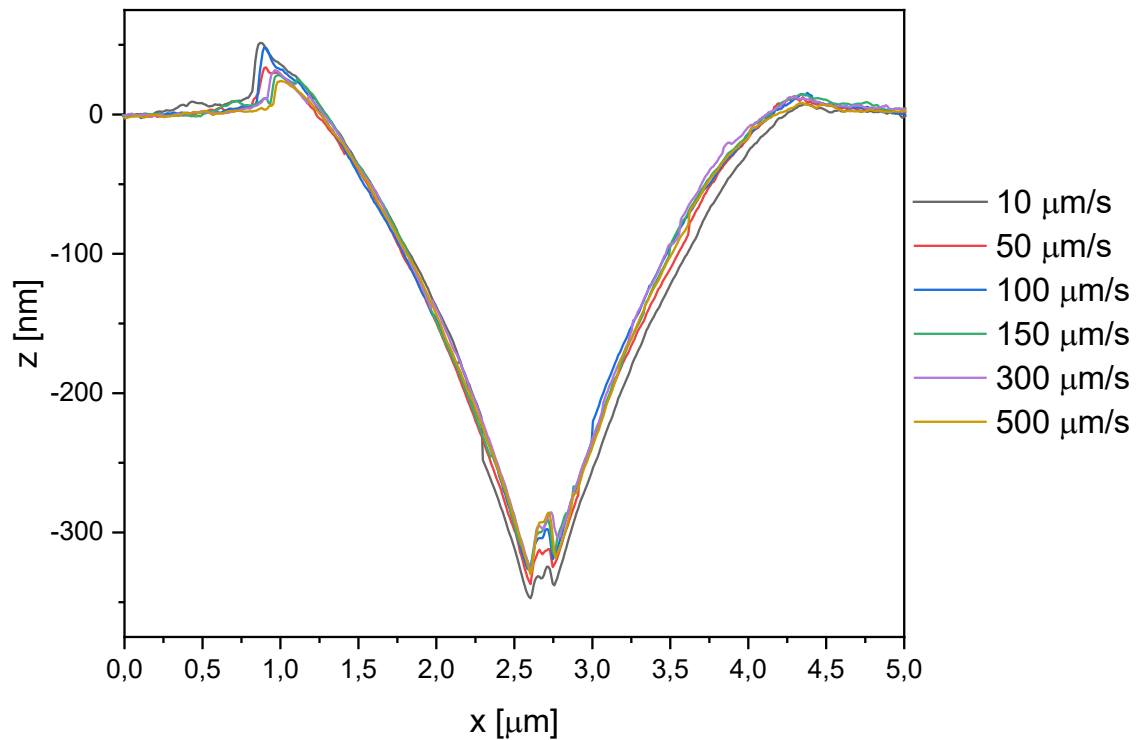


Figure B.6: Cross sections extracted at the corresponding lines in topography images shown in Figure B.5

Acknowledgements

Many people have contributed to this thesis and supported me over the past years which enabled the finishing of this thesis. I want to thank all of them here.

First of all I deeply thank Prof. Dr. Enrico Gnecco for providing the interesting topic as well as all the time he has spent over the past years to support me. He was always available for discussions even in the distance. Next to his scientific support he always enabled the compatibility of work and family.

I want to thank all members of the Otto Schott Institute of Materials Research at Friedrich Schiller University Jena who supported me scientifically and administratively. Some of them I want to point out. I want to thank Susanne Sandkuhl for her reliable technical assistance with all experiments. Then I want to thank Dr. Christian Helbing for all the scientific support especially with the AFM experiments. I thank Alexander Litschko and Valentin Veller for execution of AFM experiments during my maternity leave.

Additionally I thank Prof. Dr. Gianaurelio Cuniberti for giving the opportunity to finish my thesis in his group at the Institute of Materials Science at TU Dresden. I thank Sylvi Katzarow and Grit Kost for administrative support in distance and Dr. Alexander Croy for scientific support in the final stage of my PhD time.

Out of academic institutions I want to thank all people believing in me and supporting me. Especially I want to thank my husband Max Hennig for his support in all fields and the countless scientific discussions.

Viele Menschen haben zum erfolgreichen Abschluss dieser Arbeit beigetragen und mich in den letzten Jahren unterstützt. Ich möchte allen dafür danken.

Als erstes danke ich Prof. Dr. Enrico Gnecco, der mir ermöglicht hat über dieses interessante Thema zu forschen und viel Zeit in die Betreuung meiner Arbeit investiert hat. Meine Ergebnisse konnte ich jederzeit mit ihm diskutieren, auch in der Ferne. Wenn ich selbst mal Zweifel an meiner Forschung hatte, hat er die Besonderheit und Relevanz der Ergebnisse aufgezeigt und hervorgehoben. Neben der wissenschaftlichen Unterstützung hat er jederzeit die Vereinbarkeit von Familie und Beruf unterstützt.

Ich danke allen Mitarbeitern des Otto-Schott-Institutes für Materialforschung der Friedrich-Schiller-Universität Jena, die mich während meiner Promotion begleitet und unterstützt haben. Besonders hervorheben möchte ich dabei Susanne Sandkuhl für ihre zuverlässige technische Unterstützung bei meinen Experimenten. Außerdem danke ich Dr. Christian Helbing für die zahlreichen wissenschaftlichen Diskussionen und Unterstützung insbesondere bei AFM Messungen. Danke auch an Alexander Litschko und Valentin Feller, die AFM Experimente während meiner Elternzeit durchgeführt haben.

Weiterhin danke ich Prof. Dr. Gianaurelio Cuniberti dafür, dass er mir den Abschluss meiner Promotion in deiner Arbeitsgruppe am Institut für Werkstoffwissenschaften an der TU

Dresden ermöglicht hat. Vielen Dank auch an Sylvi Katzarow und Grit Kost für die administrative Unterstützung aus der Ferne und an Dr. Alexander Croy für die wissenschaftliche Unterstützung in Jena.

Außerhalb der akademischen Institutionen danke ich allen Menschen, die an mich geglaubt und mich unterstützt haben. Besonders herausheben möchte ich hier meinen Mann Max Hennig. Danke für die Unterstützung in allen Bereichen und die unzähligen fachlichen Diskussionen über meine Forschung.

References

1. *Wrinkled Polymer Surfaces - Strategies, Methods and Applications*. 2019: Springer Nature Switzerland AG.
2. Raj, S.S., et al., *Fabrication and Applications of Wrinkled Soft Substrates: An Overview*. Chemistryselect, 2022. **7**(16): p. 17.
3. Linklater, D.P., et al., *Mechano-bactericidal actions of nanostructured surfaces*. Nature Reviews Microbiology, 2021. **19**(1): p. 8-22.
4. Tripathy, A., et al., *Natural and bioinspired nanostructured bactericidal surfaces*. Advances in Colloid and Interface Science, 2017. **248**: p. 85-104.
5. Handy, K. *Wüsten : Sand, Kies und Steine | BR Kinder - eure Startseite*. 2019 [cited 2022 Jan].
6. Kunz, C., et al., *Large-area fabrication of low- and high-spatial-frequency laser-induced periodic surface structures on carbon fibers*. Carbon, 2018. **133**: p. 176-185.
7. Bonse, J., et al., *Femtosecond laser-induced periodic surface structures*. Journal of Laser Applications, 2012. **24**(4).
8. D'Acunto, M., et al., *Fast formation of ripples induced by AFM. A new method for patterning polymers on nanoscale*. Materials Letters, 2007. **61**(14-15): p. 3305-3309.
9. Socoliuc, A., et al., *Ripple formation induced in localized abrasion*. Physical Review B, 2003. **68**(11).
10. Gnecco, E., et al., *Linear ripples and traveling circular ripples produced on polymers by thermal AFM probes*. Physical Review B, 2009. **79**(23).
11. Yan, Y.D., et al., *Controlled nanodot fabrication by rippling polycarbonate surface using an AFM diamond tip*. Nanoscale Research Letters, 2014. **9**: p. 7.
12. Friedrich, S. and B. Cappella, *Friction and Mechanical Properties of AFM-Scan-Induced Ripples in Polymer Films*. Frontiers in Mechanical Engineering-Switzerland, 2021. **7**.
13. Sawamura, S., et al., *Lateral deformation and defect resistance of compacted silica glass: Quantification of the scratching hardness of brittle glasses*. Journal of Non-Crystalline Solids, 2018. **481**: p. 503-511.
14. Li, C., et al., *Surface deformation and friction characteristic of nano scratch at ductile-removal regime for optical glass BK7*. Appl Opt, 2016. **55**(24): p. 6547-53.
15. Xia, Y.N. and G.M. Whitesides, *Soft lithography*. Annual Review of Materials Science, 1998. **28**: p. 153-184.
16. Garcia, R., A.W. Knoll, and E. Riedo, *Advanced scanning probe lithography*. Nature Nanotechnology, 2014. **9**(8): p. 577-587.
17. Yu, B.J. and L.M. Qian, *Friction-Induced Nanofabrication: A Review*. Chinese Journal of Mechanical Engineering, 2021. **34**(1).
18. Gnecco, E., et al., *Surface rippling induced by periodic instabilities on a polymer surface*. New Journal of Physics, 2015. **17**.
19. Gong, W.W., et al., *Occurrence and distribution of micro- and mesoplastics in the high-latitude nature reserve, northern China*. Frontiers of Environmental Science & Engineering, 2022. **16**(9).
20. Zhou, B.Y., et al., *Microplastics in agricultural soils on the coastal plain of Hangzhou Bay, east China: Multiple sources other than plastic mulching film*. Journal of Hazardous Materials, 2020. **388**.

21. Courteney-Jones, W., et al., *Microplastic pollution identified in deep-sea water and ingested by benthic invertebrates in the Rockall Trough, North Atlantic Ocean*. Environmental Pollution, 2017. **231**: p. 271-280.
22. Cozar, A., et al., *The Arctic Ocean as a dead end for floating plastics in the North Atlantic branch of the Thermohaline Circulation*. Science Advances, 2017. **3**(4).
23. Suaria, G., et al., *The Mediterranean Plastic Soup: synthetic polymers in Mediterranean surface waters*. Scientific Reports, 2016. **6**.
24. Zhang, D.D., et al., *Microplastic pollution in deep-sea sediments and organisms of the Western Pacific Ocean*. Environmental Pollution, 2020. **259**.
25. Eerkes-Medrano, D., R.C. Thompson, and D.C. Aldridge, *Microplastics in freshwater systems: A review of the emerging threats, identification of knowledge gaps and prioritisation of research needs*. Water Research, 2015. **75**: p. 63-82.
26. Dris, R., et al., *Synthetic and non-synthetic anthropogenic fibers in a river under the impact of Paris Megacity: Sampling methodological aspects and flux estimations*. Science of the Total Environment, 2018. **618**: p. 157-164.
27. Evangeliou, N., et al., *Atmospheric transport is a major pathway of microplastics to remote regions*. Nature Communications, 2020. **11**(1).
28. Materic, D., et al., *Micro- and Nanoplastics in Alpine Snow: A New Method for Chemical Identification and (Semi)Quantification in the Nanogram Range*. Environmental Science & Technology, 2020. **54**(4): p. 2353-2359.
29. Bergmann, M., et al., *White and wonderful? Microplastics prevail in snow from the Alps to the Arctic*. Science Advances, 2019. **5**(8).
30. Kelly, A., et al., *Microplastic contamination in east Antarctic sea ice*. Marine Pollution Bulletin, 2020. **154**.
31. Barnes, D.K.A., et al., *Accumulation and fragmentation of plastic debris in global environments*. Philosophical Transactions of the Royal Society B-Biological Sciences, 2009. **364**(1526): p. 1985-1998.
32. Cox, K.D., et al., *Human Consumption of Microplastics*. Environmental Science & Technology, 2019. **53**(12): p. 7068-7074.
33. Machado, A.A.D., et al., *Microplastics as an emerging threat to terrestrial ecosystems*. Global Change Biology, 2018. **24**(4): p. 1405-1416.
34. da Costa, J.P., et al., *(Nano)plastics in the environment - Sources, fates and effects*. Science of the Total Environment, 2016. **566**: p. 15-26.
35. Mattsson, K., L.A. Hansson, and T. Cedervall, *Nano-plastics in the aquatic environment*. Environmental Science-Processes & Impacts, 2015. **17**(10): p. 1712-1721.
36. del Barrio, E. and C. Sanchez-Somolinos, *Light to Shape the Future: From Photolithography to 4D Printing*. Advanced Optical Materials, 2019. **7**(16).
37. Qin, D., et al., *Microfabrication, microstructures and microsystems*. Microsystem Technology in Chemistry and Life Science, 1998. **194**: p. 1-20.
38. Binnig, G., C.F. Quate, and C. Gerber, *ATOMIC FORCE MICROSCOPE*. Physical Review Letters, 1986. **56**(9): p. 930-933.
39. Sarid, D., et al., *COMPACT SCANNING-FORCE MICROSCOPE USING A LASER DIODE*. Optics Letters, 1988. **13**(12): p. 1057-1059.
40. Sarid, D., et al., *PERFORMANCE OF A SCANNING FORCE MICROSCOPE USING A LASER DIODE*. Journal of Vacuum Science & Technology a-Vacuum Surfaces and Films, 1990. **8**(1): p. 378-382.
41. Garcia, R. and R. Perez, *Dynamic atomic force microscopy methods*. Surface Science Reports, 2002. **47**(6-8): p. 197-301.

42. Parrat, D., et al., *IMAGING MODES IN ATOMIC-FORCE MICROSCOPY*. Journal of Trace and Microprobe Techniques, 1995. **13**(3): p. 343-352.
43. Hutter, J.L. and J. Bechhoefer, *CALIBRATION OF ATOMIC-FORCE MICROSCOPE TIPS*. Review of Scientific Instruments, 1993. **64**(7): p. 1868-1873.
44. Cohen, S.R., *AN EVALUATION OF THE USE OF THE ATOMIC FORCE MICROSCOPE FOR STUDIES IN NANOMECHANICS*. Ultramicroscopy, 1992. **42**: p. 66-72.
45. Sader, J.E., J.W.M. Chon, and P. Mulvaney, *Calibration of rectangular atomic force microscope cantilevers*. Review of Scientific Instruments, 1999. **70**(10): p. 3967-3969.
46. Sader, J.E., et al., *Spring constant calibration of atomic force microscope cantilevers of arbitrary shape*. Review of Scientific Instruments, 2012. **83**(10).
47. Yan, Y.D., et al., *Scratch on Polymer Materials Using AFM Tip-Based Approach: A Review*. Polymers, 2019. **11**(10).
48. D'Acunto, M., F. Dinelli, and P. Pingue, *Nanoscale rippling on polymer surfaces induced by AFM manipulation*. Beilstein Journal of Nanotechnology, 2015. **6**: p. 2278-2289.
49. Hay, J., *INTRODUCTION TO INSTRUMENTED INDENTATION TESTING*. Experimental Techniques, 2009. **33**(6): p. 66-72.
50. Oliver, W.C. and G.M. Pharr, *AN IMPROVED TECHNIQUE FOR DETERMINING HARDNESS AND ELASTIC-MODULUS USING LOAD AND DISPLACEMENT SENSING INDENTATION EXPERIMENTS*. Journal of Materials Research, 1992. **7**(6): p. 1564-1583.
51. Jiménez-Piqué, E., Y. Gaillard, and M.J. Anglada, *Instrumented indentation of layered ceramic materials*. Key Engineering Materials, 2007. **333**: p. 107-116.
52. Qian, L. and H.W. Zhao, *Nanoindentation of Soft Biological Materials*. Micromachines, 2018. **9**(12).
53. Xia, J., et al., *Nanoindentation and nanoscratch properties of a thermal oxidation treated gamma-TiAl based alloy*. Surface & Coatings Technology, 2006. **200**(16-17): p. 4755-4762.
54. Beake, B.D. and G.J. Leggett, *Nanoindentation and nanoscratch testing of uniaxially and biaxially drawn poly(ethylene terephthalate) film*. Polymer, 2002. **43**(2): p. 319-327.
55. Pelletier, H., C. Mendibide, and A. Riche, *Mechanical characterization of polymeric films using depth-sensing instrument: Correlation between viscoelastic-plastic properties and scratch resistance*. Progress in Organic Coatings, 2008. **62**(2): p. 162-178.
56. Wang, X.F., et al., *A review on the mechanical properties for thin film and block structure characterised by using nanoscratch test*. Nanotechnology Reviews, 2019. **8**(1): p. 628-644.
57. Kasimuthumaniyan, S., N.N. Gosvami, and N.M.A. Krishnan, *Towards understanding the scratchability in functional glasses*. Ceramics International, 2021. **47**(15): p. 20821-20843.
58. Tsujimoto, A., et al., *Wear of resin composites: Current insights into underlying mechanisms, evaluation methods and influential factors*. Japanese Dental Science Review, 2018. **54**(2): p. 76-87.
59. Varenberg, M., *Towards a unified classification of wear*. Friction, 2013. **1**(4): p. 333-340.
60. Burwell, J.T., *Survey of possible wear mechanisms*. Wear, 1957. **1**(2): p. 119-141.
61. Eagleson, H.V., *AN EXPERIMENTAL METHOD FOR DETERMINING COEFFICIENTS OF SLIDING FRICTION*. American Journal of Physics, 1945. **13**(1): p. 43-44.

62. Socoliuc, A., et al., *Transition from stick-slip to continuous sliding in atomic friction: entering a new regime of ultralow friction*. Phys Rev Lett, 2004. **92**(13): p. 134301.
63. Harris, R.A. and S.M. Day, *Effects of a low-velocity zone on a dynamic rupture*. Bulletin of the Seismological Society of America, 1997. **87**(5): p. 1267-1280.
64. Gnecco, E. and E. Meyer, *Elements of Friction Theory and Nanotribology*. 2015, Cambridge: University Printing House, Cambridge CB2 8BS, United Kingdom.
65. Rabinowicz, E., *THE INTRINSIC VARIABLES AFFECTING THE STICK-SLIP PROCESS*. Proceedings of the Physical Society of London, 1958. **71**(460): p. 668-675.
66. Prandtl, L., *Ein Gedankenmodell zur kinetischen Theorie der festen Körper*. Zeitschrift für angewandte Mathematik und Mechanik, 1928. **8**: p. 85-106.
67. Tomlinson, G.A., *CVI. A molecular theory of friction*. The London, Edinburgh, and Dublin Philosophical Magazine and Journal of Science, 1929. **7**(46): p. 905-939.
68. Popov, V.L. and J.A.T. Gray, *Prandtl-Tomlinson model: History and applications in friction, plasticity, and nanotechnologies*. Zamm-Zeitschrift Fur Angewandte Mathematik Und Mechanik, 2012. **92**(9): p. 683-708.
69. Luthi, R., et al., *Nanotribology: an UHV-SFM study on thin films of AgBr(001)*. Tribology Letters, 1995. **1**(1): p. 23-33.
70. Mate, C.M., et al., *ATOMIC-SCALE FRICTION OF A TUNGSTEN TIP ON A GRAPHITE SURFACE*. Physical Review Letters, 1987. **59**(17): p. 1942-1945.
71. Hall, D.B., P. Underhill, and J.M. Torkelson, *Spin coating of thin and ultrathin polymer films*. Polymer Engineering and Science, 1998. **38**(12): p. 2039-2045.
72. Sampaio, P.G.V., et al., *Overview of printing and coating techniques in the production of organic photovoltaic cells*. International Journal of Energy Research, 2020. **44**(13): p. 9912-9931.
73. Hennig, J., et al., *Locking effects in plowing-induced nanorippling of polystyrene surfaces*. Applied Surface Science, 2022. **594**.
74. Hennig, J., et al., *Nucleation and detachment of polystyrene nanoparticles from plowing-induced surface wrinkling*. Applied Surface Science Advances, 2021. **6**.
75. Aoike, T., et al., *Surface deformation properties of polystyrene as evaluated from the morphology of surfaces scratched by using the tip of a scanning force microscope*. Langmuir, 2001. **17**(18): p. 5688-5692.
76. Napolitano, S., et al., *Ordered rippling of polymer surfaces by nanolithography: influence of scan pattern and boundary effects*. Nanotechnology, 2012. **23**(47).
77. Yan, Y.D., et al., *Effects of the AFM tip trace on nanobundles formation on the polymer surface*. Applied Surface Science, 2012. **258**(24): p. 9656-9663.
78. Sun, Y., et al., *Effect of the molecular weight on deformation states of the polystyrene film by AFM single scanning*. Scanning, 2013. **35**(5): p. 308-15.
79. Mazo, J.J., et al., *Plowing-Induced Structuring of Compliant Surfaces*. Physical Review Letters, 2019. **122**(25).
80. Yan, Y.D., et al., *Effect of scratching trajectory and feeding direction on formation of ripple structure on polycarbonate sheet using AFM tip-based nanomachining process*. Micro & Nano Letters, 2017. **12**(12): p. 1011-1015.
81. Wang, J.Q., et al., *Study of the formation mechanism of bundle structures using AFM tip-based nanoscratching approach*. Tribology International, 2020. **142**: p. 10.
82. Leach, R.N., et al., *Nanometer-scale solvent-assisted modification of polymer surfaces using the atomic force microscope*. Langmuir, 2003. **19**(24): p. 10225-10232.

83. Alimi, O.S., et al., *Microplastics and Nanoplastics in Aquatic Environments: Aggregation, Deposition, and Enhanced Contaminant Transport*. Environmental Science & Technology, 2018. **52**(4): p. 1704-1724.
84. Allen, S., et al., *Atmospheric transport and deposition of microplastics in a remote mountain catchment*. Nature Geoscience, 2019. **12**(5): p. 339-+.
85. Hammer, J., M.H.S. Kraak, and J.R. Parsons, *Plastics in the Marine Environment: The Dark Side of a Modern Gift*, in *Reviews of Environmental Contamination and Toxicology*, Vol 220, D.M. Whitacre, Editor. 2012. p. 1-44.
86. Rossi, G., J. Barnoud, and L. Monticelli, *Polystyrene Nanoparticles Perturb Lipid Membranes*. Journal of Physical Chemistry Letters, 2014. **5**(1): p. 241-246.
87. Salvati, A., et al., *Experimental and theoretical comparison of intracellular import of polymeric nanoparticles and small molecules: toward models of uptake kinetics*. Nanomedicine-Nanotechnology Biology and Medicine, 2011. **7**(6): p. 818-826.
88. Xia, T., et al., *Cationic polystyrene nanosphere toxicity depends on cell-specific endocytic and mitochondrial injury pathways*. Acs Nano, 2008. **2**(1): p. 85-96.
89. Forte, M., et al., *Polystyrene nanoparticles internalization in human gastric adenocarcinoma cells*. Toxicology in Vitro, 2016. **31**: p. 126-136.
90. Almutairi, M.M.A., et al., *Factors controlling permeability of the blood-brain barrier*. Cellular and Molecular Life Sciences, 2016. **73**(1): p. 57-77.
91. Liu, P., et al., *Effect of weathering on environmental behavior of microplastics: Properties, sorption and potential risks*. Chemosphere, 2020. **242**: p. 12.
92. Zhang, K., et al., *Understanding plastic degradation and microplastic formation in the environment: A review*. Environmental Pollution, 2021. **274**: p. 14.
93. Hsiao, C.C. and J.A. Sauer, *ON CRAZING OF LINEAR HIGH POLYMERS*. Journal of Applied Physics, 1950. **21**(11): p. 1071-1083.
94. Baltenneck, F., J.P. Trotignon, and J. Verdu, *Kinetics of fatigue failure of polystyrene*. Polymer Engineering and Science, 1997. **37**(10): p. 1740-1747.
95. Caputo, F., et al., *Measuring particle size distribution and mass concentration of nanoplastics and microplastics: addressing some analytical challenges in the sub-micron size range*. Journal of Colloid and Interface Science, 2021. **588**: p. 401-417.
96. Enfrin, M., et al., *Nano/micro plastics - Challenges on quantification and remediation: A review*. Journal of Water Process Engineering, 2021. **42**: p. 28.
97. Pedraz, P., R. Wannemacher, and E. Gnecco, *Controlled Suppression of Wear on the Nanoscale by Ultrasonic Vibrations*. Acs Nano, 2015. **9**(9): p. 8859-8868.
98. Dinelli, F., G.J. Leggett, and P.H. Shipway, *Nanowear of polystyrene surfaces: molecular entanglement and bundle formation*. Nanotechnology, 2005. **16**(6): p. 675-682.
99. Puspoki, Z., et al., *Transforms and Operators for Directional Bioimage Analysis: A Survey*, in *Focus on Bio-Image Informatics*, W.H. DeVos, S. Munck, and J.P. Timmermans, Editors. 2016, Springer-Verlag Berlin: Berlin. p. 69-93.
100. Fonck, E., et al., *Effect of Aging on Elastin Functionality in Human Cerebral Arteries*. Stroke, 2009. **40**(7): p. 2552-2556.
101. Dickson, M.N., et al., *Nanopatterned polymer surfaces with bactericidal properties*. Biointerphases, 2015. **10**(2): p. 8.
102. Kim, S., et al., *Nanostructured Multifunctional Surface with Antireflective and Antimicrobial Characteristics*. Acs Applied Materials & Interfaces, 2015. **7**(1): p. 326-331.

103. Valle, J., et al., *Evaluation of Surface Microtopography Engineered by Direct Laser Interference for Bacterial Anti-Biofouling*. Macromolecular Bioscience, 2015. **15**(8): p. 1060-1069.
104. Deubel, M., et al., *Direct laser writing of three-dimensional photonic-crystal templates for telecommunications*. Nature Materials, 2004. **3**(7): p. 444-447.
105. Wang, Y.S., et al., *Enhancing the stability of polymer nanostructures via ultrathin oxide coatings for nano-optical device applications*. Nanotechnology, 2021. **32**(29): p. 9.
106. Darwich, S., et al., *Manipulation of gold colloidal nanoparticles with atomic force microscopy in dynamic mode: influence of particle-substrate chemistry and morphology, and of operating conditions*. Beilstein Journal of Nanotechnology, 2011. **2**: p. 85-98.
107. Rao, A., et al., *Trajectory fluctuations accompanying the manipulation of spherical nanoparticles*. Physical Review B, 2009. **80**(19).
108. Villarrubia, J.S., *Algorithms for scanned probe microscope image simulation, surface reconstruction, and tip estimation*. Journal of Research of the National Institute of Standards and Technology, 1997. **102**(4): p. 425-454.
109. Argon, A.S. and M. Salama, *MECHANISM OF FRACTURE IN GLASSY MATERIALS CAPABLE OF SOME INELASTIC DEFORMATION*. Materials Science and Engineering, 1976. **23**(2-3): p. 219-230.
110. Kausch, H.H. and G.H. Michler, *The effect of time on crazing and fracture*, in *Intrinsic Molecular Mobility and Toughness of Polymers I*, H.H. Kausch, Editor. 2005. p. 1-33.
111. Schmidt, R.H., G. Haugstad, and W.L. Gladfelter, *Scan-induced patterning in glassy polymer films: Using scanning force microscopy to study plastic deformation at the nanometer length scale*. Langmuir, 2003. **19**(3): p. 898-909.
112. Gnecco, E., et al., *Channeling motion of gold nanospheres on a rippled glassed surface*. Nanotechnology, 2014. **25**(48).
113. Gnecco, E., et al., *Surface rippling of silica glass surfaces scraped by a diamond indenter*. Physical Review Materials, 2018. **2**(11).
114. Gu, W., Z. Yao, and K. Li, *Evaluation of subsurface crack depth during scratch test for optical glass BK7*. Proceedings of the Institution of Mechanical Engineers, Part C: Journal of Mechanical Engineering Science, 2011. **225**(12): p. 2767-2774.
115. Moayed, E. and L. Wondraczek, *Quantitative analysis of scratch-induced microabrasion on silica glass*. Journal of Non-Crystalline Solids, 2017. **470**: p. 138-144.
116. Le Houerou, V., et al., *Surface damage of soda-lime-silica glasses: indentation scratch behavior*. Journal of Non-Crystalline Solids, 2003. **316**(1): p. 54-63.
117. Wang, W., et al., *Elastic stress field model and micro-crack evolution for isotropic brittle materials during single grit scratching*. Ceramics International, 2017. **43**(14): p. 10726-10736.
118. Wondraczek, L., et al., *Towards Ultrastrong Glasses*. Advanced Materials, 2011. **23**(39): p. 4578-4586.
119. Li, C., et al., *Surface deformation and friction characteristic of nano scratch at ductile-removal regime for optical glass BK7*. Applied Optics, 2016. **55**(24): p. 6547-6553.
120. de Macedo, G., S. Sawamura, and L. Wondraczek, *Lateral hardness and the scratch resistance of glasses in the Na₂O-CaO-SiO₂ system*. Journal of Non-Crystalline Solids, 2018. **492**: p. 94-101.
121. Sawamura, S. and L. Wondraczek, *Scratch hardness of glass*. Physical Review Materials, 2018. **2**(9).

122. Lawn, B.R., S.M. Wiederhorn, and D.E. Roberts, *EFFECT OF SLIDING FRICTION FORCES ON THE STRENGTH OF BRITTLE MATERIALS*. Journal of Materials Science, 1984. **19**(8): p. 2561-2569.
123. Li, K., Y. Shapiro, and J.C.M. Li, *Scratch test of soda-lime glass*. Acta Materialia, 1998. **46**(15): p. 5569-5578.
124. Horcas, I., et al., *WSXM: A software for scanning probe microscopy and a tool for nanotechnology*. Review of Scientific Instruments, 2007. **78**(1).
125. Miura, T., et al., *Universal hardness and elastic recovery in Vickers nanoindentation of copper phosphate and silicate glasses*. Journal of the European Ceramic Society, 2003. **23**(3): p. 409-416.
126. Hojamberdiev, M. and H.J. Stevens, *Indentation recovery of soda-lime silicate glasses containing titania, zirconia and hafnia at low temperatures*. Materials Science and Engineering a-Structural Materials Properties Microstructure and Processing, 2012. **532**: p. 456-461.
127. Hojamberdiev, M., H.J. Stevens, and W.C. LaCourse, *Environment-dependent indentation recovery of select soda-lime silicate glasses*. Ceramics International, 2012. **38**(2): p. 1463-1471.
128. Shi, C.L., et al., *Effects of Indenter Tilt on Nanoindentation Results of Fused Silica: an Investigation by Finite Element Analysis*. Materials Transactions, 2013. **54**(6): p. 958-963.